STUDY OF FLUX PINNING IN THICK FILM REBCO COATED CONDUCTORS OVER A WIDE RANGE OF MAGNETIC FIELDS AND TEMPERATURES

by

Mehdi Kochat

A dissertation submitted to the Department of Mechanical Engineering,
University of Houston
in partial fulfillment of the requirements for the degree of
DOCTOR OF PHILOSOPHY
in Mechanical Engineering

Chair of Committee: Dr. Venkat Selvamanickam

Committee Member: Dr. Haleh Ardebili

Committee Member: Dr. Yashashree Kulkarni

Committee Member: Dr. Jae-Hyun Ryou

Committee Member: Dr. John C. Wolfe

University of Houston

May 2020

DEDICATION

To my family and friends

ACKNOWLEDGEMENTS

First, I would like to express my sincere gratitude to my advisor Professor Venkat Selvamanickam for his guidance during the PhD. I am grateful for the opportunity and the strong support during this journey. Thank you.

I also would like to thank my PhD committee members, Dr. Haleh Ardebili, Dr. Yashashree Kulkarni, Dr. Jae-Hyun Ryou and Dr. John C. Wolfe for their guidance and comments.

I want to thank my fellow lab mates for their support, encouragement and for all the fun moments we shared. This work could not have been achieved without your help. Special thanks to Xiao-Fen Li, I am thankful to him for sharing his knowledge and for caring.

I thank Dr. J. Jaroszynski and all the wonderful scientists who assisted me during my visits to the National High Magnetic Field Lab.

I am grateful to the Departments of Energy and High Energy Physics for funding this research work.

Last but not least I am thankful to my parents, my sisters and my wife for their support and endless love.

ABSTRACT

RE-Ba-Cu-O (REBCO, RE = rare earth) coated conductors are approaching the large-scale electric power and magnetic applications over a wide range of temperatures and magnetic fields owing to their high critical current density (J_c), their high critical temperature (T_c) and their strong irreversibility field (H_{irr}). However, further enhancement of the engineering critical current (J_e) is required to make REBCO more cost-effective.

Improving J_e can be achieved by combining two strategies: achieving a thickness independent J_c and enhancing the flux pinning landscape in REBCO through the incorporation of artificial pinning centers (APC). In this work, are studied REBCO tapes deposited using an advanced metal organic vapor deposition process (A-MOCVD) allowing the growth of up to 5 μm thick high performing REBCO films without a deterioration in J_c. $BaMO_3$ (M: Zr, Hf, and Nb) self-assembled nanorods with different concentrations up to 15 mol% were incorporated into REBCO to enhance their J_c over a wide range of temperature (4.2—77 K) and applied magnetic field (0—31 T). The effect of the density, size, and continuity of the BMOs were systematically studied revealing a stronger contribution of the continuous and dense nanorods to the J_c at high magnetic fields and low temperatures.

Additionally, $BaZrO_3$ doped REBCO were subject to post-deposition tensile-creep-deformation at 580°C leading to an increase in the density of ab-plane stacking faults which correlated with up to 3 times higher critical current than a reference sample at 77 K and 1 T when the magnetic field is parallel to the ab-plane.

Finally, Artificial Neural Networks (ANN) were trained to accurately predict lower temperature critical currents out of the 65 K critical currents. The ANN predictions showed an average error of 2.8% at 4.2 K and 13 T when applied on a validation dataset containing 100 samples.

TABLE OF CONTENTS

LIST OF TABLES

LIST OF FIGURES

Chapter 1. Introduction

In this Chapter, a background on superconductivity is introduced with a focus on the flux pinning in $YBa_2Cu_3O_{7-x}$ (YBCO) coated conductors which is the motivation of the thesis. The chapter contains five parts: an introduction to superconductivity, electromagnetic properties and flux pinning in YBCO, synthesis of YBCO coated conductors, the challenges related to this material and the objectives of the dissertation.

1.1. Introduction to Superconductivity in YBCO

Superconductivity was first discovered by Hike Kamerlingh Onnes in 1911 when he noted a sharp drop in the electrical resistance of mercury from 0.12 Ω at 4.3 K to less than 10^{-6} Ω below 4.2 K [1]. The first parameter that is particular to a superconducting material is its critical temperature (T_c), which is the temperature below which the superconducting material has zero resistance to electric current.

In 1957, Bardeen, Cooper, and Schrieffer successfully explained superconductivity in conventional low temperature superconductors by the existence of an electron–phonon interaction below T_c; this was called the BCS theory [2]. The BCS theory explains superconductivity for low-temperature superconductors (LTS); the highest T_c for an LTS superconductor was found to be 39 K in MgB_2 [3].

YBCO ($YBa_2Cu_3O_{7-x}$) is a high-temperature superconducting (HTS) material that was first reported by Wu et al. in 1987 [4]; they observed that it had a superconducting transition T_c at 93 K. While the BCS theory does not predict or explain superconductivity in HTS materials, new materials with a higher T_c than YBCO at ambient pressure were discovered in the years following Wu et al.'s discovery. In 1988,

$Bi_2SrCaCu_2O_x$ (BSCCO) was discovered, which has a T_c of 105 K [5]. In 1994, the discovery of $HgBa_2Ca_3Cu_3O_{8+x}$ was announced [6], it is a material that has a T_c of 135 K at ambient pressure and 164 K under higher pressures. A summary of the HTS materials is shown in Figure 1-1 [7].

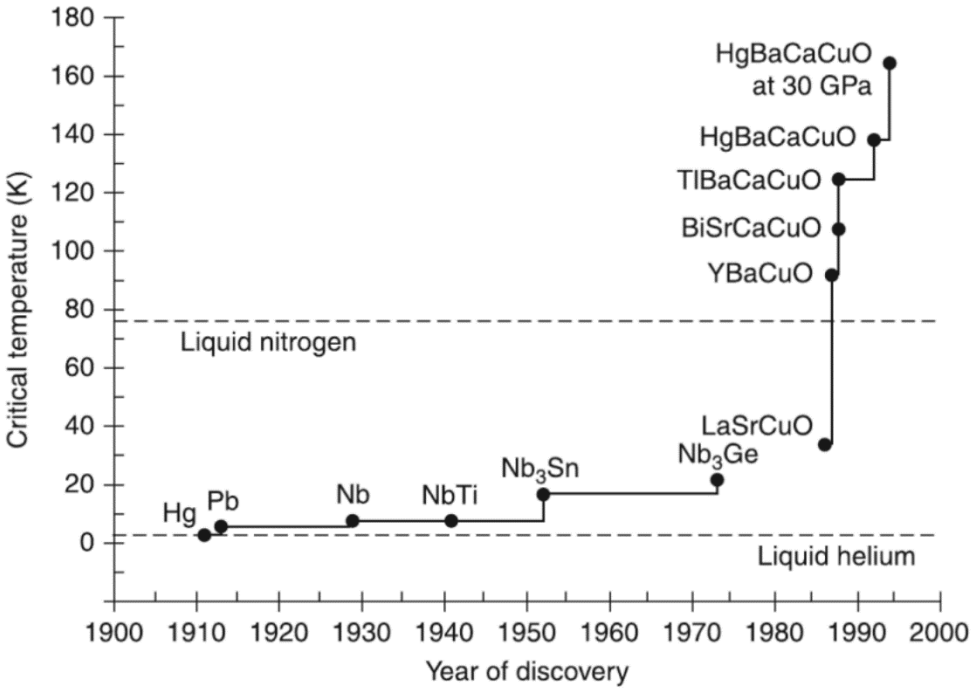

Figure 1-1. Evolution of the critical temperature of several LTS and HTS materials.

1.1.1. Crystal Structure of YBCO

YBCO has a complicated crystal structure. Its unit cell is formed of a succession of three perovskite structures, as follows: two adjacent $BaCuO_3$ cubes and one central $YCuO_3$ sub-cell. The YBCO structure often contains some unoccupied oxygen positions, which makes this material structure often distorted. $YBa_2Cu_3O_{7-x}$ has two crystalline structures depending on its oxygen content; it is orthorhombic for $x \geq 0.5$ and tetragonal otherwise [8-10] (Figure 1-2) [11].

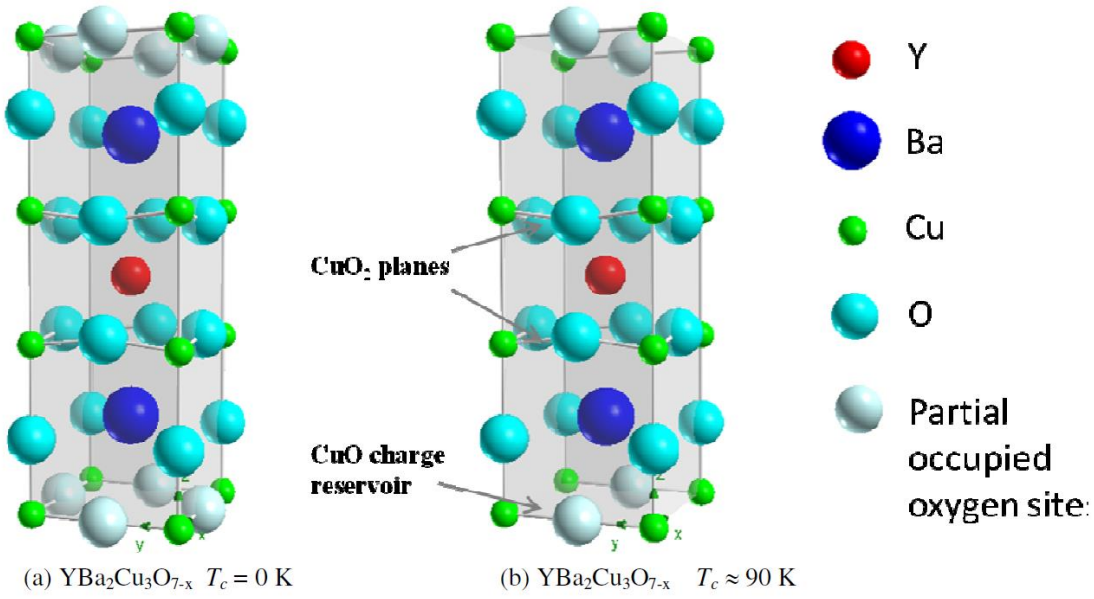

Figure 1-2. (a) Tetragonal $YBa_2Cu_3O_{7-x}$ with $x \geq 0.5$ and (b) Orthorhombic $YBa_2Cu_3O_{7-x}$ when $x \leq 0.5$.

While YBCO in its tetragonal structure is a not superconducting, its orthorhombic structure has a T_c of approximately 92 K. The T_c value depends on the oxygen content in $YBa_2Cu_3O_{7-x}$ and its optimal highest value is obtained for an x of approximately 0.07 [12]. In the YBCO crystallographic structure, each Cu atom is linked to four oxygen atoms in the CuO_x plane and to five oxygen atoms in the CuO_2 plane while the Ba and Y atoms are stacked in a Ba-Y-Ba sequence along the c-axis. The Ba atoms are slightly tilted toward the Y atom [8].

In addition to the $YBa_2Cu_3O_{7-x}$ (Y123), two other superconducting variations of the YBCO phase exist, as follows: the $Y_2Ba_4Cu_7O_{14+x}$ (Y247) that has a T_c of approximately 40 K [13] and the $YBa_2Cu_4O_8$ (Y124) that has a T_c around 80 K [14]. While the Y124 structure was discovered as a defect in bulk Y123, the Y247 phase was only reported in thin films, and it is believed to be an alternation between the Y123 and

the Y124 structures. Set side by side with the Y123 phase, the Y124 phase has an extra CuO_x chain.

Table 1-1.Three different superconducting phases of YBCO were reported to date.

Notation	Structure	T_c (K)	Lattice parameters (Å)			Formula
			a	b	c	
Y123	Tetragonal	Non superconducting	3.87	3.87	11.72	$YBa_2Cu_3O_{6+x}$ $x\leq 0.5$
	orthorhombic	92	3.82	3.89	11.66	$YBa_2Cu_3O_{7-x}$ $x\geq 0.5$
Y124	Tetragonal	80	3.83	3.83	27.20	$YBa_2Cu_4O_8$
Y247	Tetragonal	40	3.83	3.87	50.59	$Y_2Ba_4Cu_7O_{14+x}$

1.1.2. Mechanisms of Superconductivity and Anisotropy in YBCO

Conduction in YBCO happens by charge transfer between the Cu_2O and CuO_x planes [9]. Based on this mechanism, the CuO_x are hole carriers to the CuO_2 planes. Conduction in the copper planes makes the conductivity much stronger in the a–b plane, and this causes the observed anisotropy in the transport properties in YBCO. For other cuprates, the anisotropy is even greater because of the increased spacing of the CuO planes along the c-axis [15].

The electron mass anisotropy γ defines the anisotropy of high-temperature superconductors, as in Equation (1-1). The value of γ is always higher than 1 and for YBCO, it is approximately 5 because of the highly-layered orthorhombic crystal structure of YBCO.

$$\gamma = \frac{1}{\varepsilon} = \sqrt{\frac{m_c}{m_{ab}}} = \frac{\lambda_c}{\lambda_{ab}} = \frac{\zeta_{ab}}{\zeta_c} \ , \qquad \text{Equation (1-1)}$$

where m_c and m_{ab} are the effective electron mass in the c-axis and a–b plane, respectively; λ is the London penetration depth that characterizes the distance over which the magnetic field penetrates the superconducting material; and ζ is the coherence length that characterizes the density of the Cooper pairs, it is the distance over which their density reaches its maximum.

1.2. Electromagnetic properties and flux Pinning in YBCO

1.2.1. Magnetic properties of Superconductors

In addition to its zero resistivity below T_c, (it was measured to be below 3.6×10^{-23} Ω.cm [16]) the second characteristic of a superconducting material is its perfect diamagnetism that was discovered by Walter Meissner and Robert Ochsenfeld in 1933 [17]. Below T_c, an applied external magnetic field is completely expelled from a conventional superconducting material (except near the surface, within λ). There is a maximum amount of the magnetic field that can be expelled from the superconducting materials, above which superconductivity is lost and the magnetic field penetrates the material below T_c; this limit is called the thermodynamic critical field H_c.

The Ginzburg–Landau theory distinguishes between two types of superconductors, called type I and type II based on the sign of the surface energy between the normal and the superconducting state, which is defined in Equation (1-2).

$$g_{surface} = \frac{1}{2}\mu_0 H_c^2(\zeta - \lambda) \ , \qquad \text{Equation (1-2)}$$

where μ_0 is the magnetic permeability.

The surface energy is positive for type I superconductors and negative for the type II superconductors. The sign of the surface energy was found to be directly related to the magnitude of the Ginzburg–Landau parameter *K* as

$$\kappa = \frac{\lambda}{\zeta}, \qquad \text{Equation (1-3)}$$

for type II superconductors, $K \geq 1/\sqrt{2}$ and for type I superconductors, $K \leq 1/\sqrt{2}$. For YBCO, *K* is around 100.

Two critical magnetic fields can be distinguished for the type II superconductors: the lower critical magnetic field H_{c1} and the upper critical magnetic field H_{c2}. Based on the existence of these two boundaries, a type II superconductor can be in one of three states based on the intensity of the applied external magnetic field as seen in Figure 1-3 [18]. Below H_{c1}, the superconductor is in a Meissner state, and above H_{c2}, the material is in a normal non-superconducting state. When the applied magnetic field falls between H_{c1} and H_{c2}, a type II superconductor is in an intermediate mixed state where quantized flux lines penetrate the material. Each of these flux lines is a vortex of supercurrent; a flux quantum φ_0 of magnitude 2.07×10^{-15} Wb.

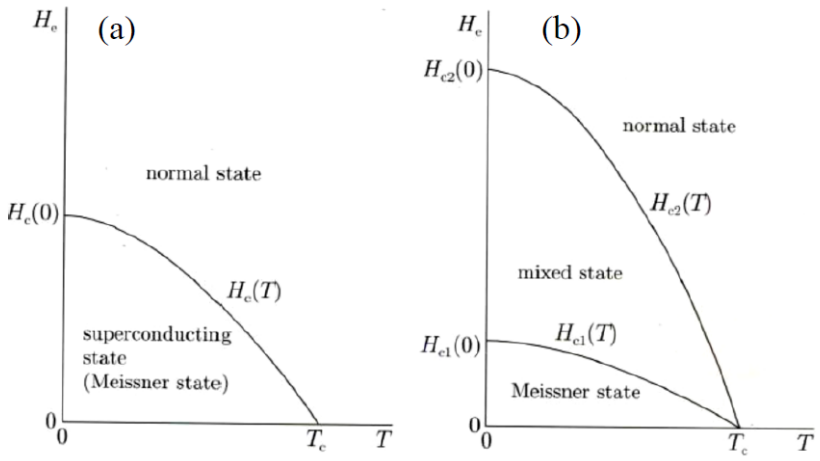

Figure 1-3. (a) Temperature-magnetic field phase diagrams for type I superconductors and (b) type II superconductors.

Each flux vortex is formed of a core of normal non-superconducting phase that has a diameter of approximately 2ζ, where the Cooper pairs are absent surrounded by a vortex of supercurrent that is approximately 2λ in diameter. As can be observed in Figure 1-4 [19], the supercurrent density decays exponentially over λ while the superconducting order parameter ψ (the square of the density of the Cooper pairs) decreases to zero at the vortex center where the Cooper pairs do not exist.

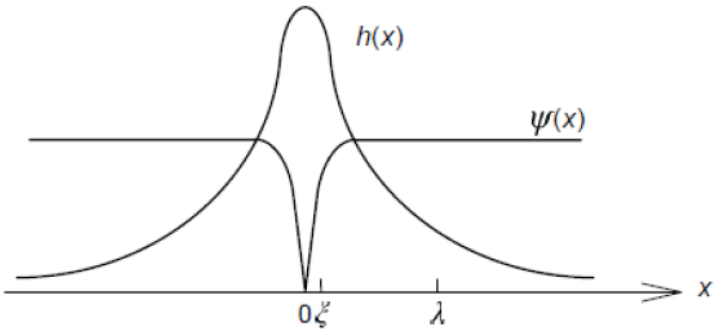

Figure 1-4. Variation of the order parameter $\psi(x)$ and the magnetic flux density $h(x)$ in a magnetic flux vortex.

Applying transport currents on a type II superconductor in the mixed state generates a Lorentz force on the vortices, which activates their motion. The motion of the vortices will generate an electric field, according to Faraday's law, resulting in the loss of the zero-resistance property of the superconducting material. Additionally, the type II superconductor can sustain a critical current only when it has a gradient of flux density, which is described by the Maxwell equation,

$$\nabla \times B = \mu_0 J, \qquad \text{Equation (1-4)}$$

this can be achieved by pinning the magnetic vortices into randomly dispersed non-superconducting cores. Because the core of the vortices is non-superconducting, it is energetically favorable for the vortices to be held in the non-superconducting structural defects that exist in the material; this is called flux pinning.

1.2.2. Flux pinning in YBCO

YBCO has naturally a high density of structural defects (intrinsic defects) such as oxygen vacancies [20], dislocations [21], cation disorders [22], and stacking faults [23] that can act as pinning centers [24]. In addition to these structural defects, artificial pinning centers have been successfully introduced into YBCO (extrinsic defects) either during the deposition process by the addition of BMO (B=Ba, M=Sn, Hf, Zr…) peroxides [25-27] or, after the deposition by irradiation damage for example [28].
Based on their dimensions the pinning centers can be classified into three categories, as follows in Figure 1-5 [29]:

- Zero-dimensional pinning centers (0D): point defects such as oxygen vacancies [20], cation disorder [30] and dilute doping [31] belong to this category. 0D are

smaller than the coherence length, and these defects are effective mostly at low temperatures.

- One-dimensional pinning centers (1D): line defects such as the nanocolumns introduced either during the deposition process: the BMOs [25-27] or by irradiation damage on fully processed films [28] and screw and edge dislocations [32]. These defects are effective mostly at high temperatures and low magnetic fields.
- Two-dimensional pinning centers (2D): such as twin boundaries and the surface of large precipitates [29].
- Three-dimensional pinning centers (3D): such as nanoparticles and second phases that are larger or in the same size as the coherence length [29].

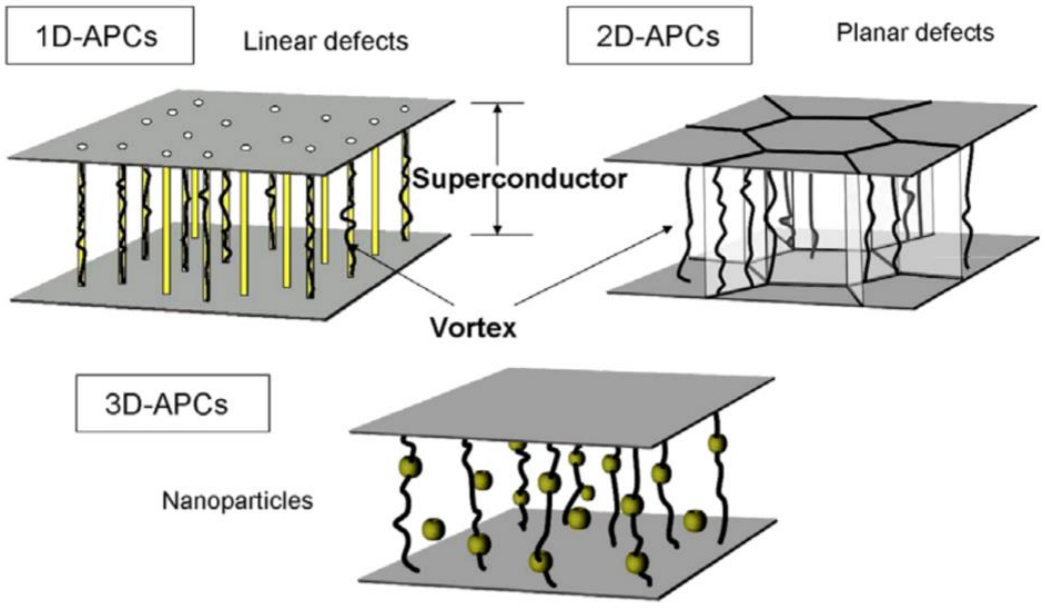

Figure 1-5. Classification of the pinning centers based in their dimensions.

Based on their pinning effect, pinning centers can be classified into the following two categories:

- Core pinning: Includes pinning centers where the dominant interaction is with the core of the vortex. In these pinning centers, the order parameter $\psi(x)$ falls to zero over a range close to ζ.
- Magnetic pinning: These pinning centers are related to the screening currents, and they are in same range as λ.

Since in YBCO λ is 100 times larger than ζ, the optimal density of effective pinning centers can be achieved by a matrix of core pinning centers. The magnetic pinning is effective when the flux vortex densities are small, such as at low magnetic fields. Surface pinning is an example of magnetic pinning [33].

As observed earlier, YBCO's crystal structure is highly anisotropic, which makes both its coherence length and penetration depth directionally dependent. This affects the structure of the vortices themselves by making them dependent on the angle between the applied magnetic field and the axes of the YBCO crystal structure. In Figure 1-6 [18], the flux vortex is anisotropic when the magnetic field is applied parallel to the CuO_2 plane; it has a shorter radius in the c-direction, while the vortex has an isotropic geometry when the magnetic field is applied parallel to the YBCO c-axis. Since the dimensions of an ideal pinning center should be in the same scale of the coherence length to be effective, the effectiveness of the pinning centers in YBCO is anisotropic.

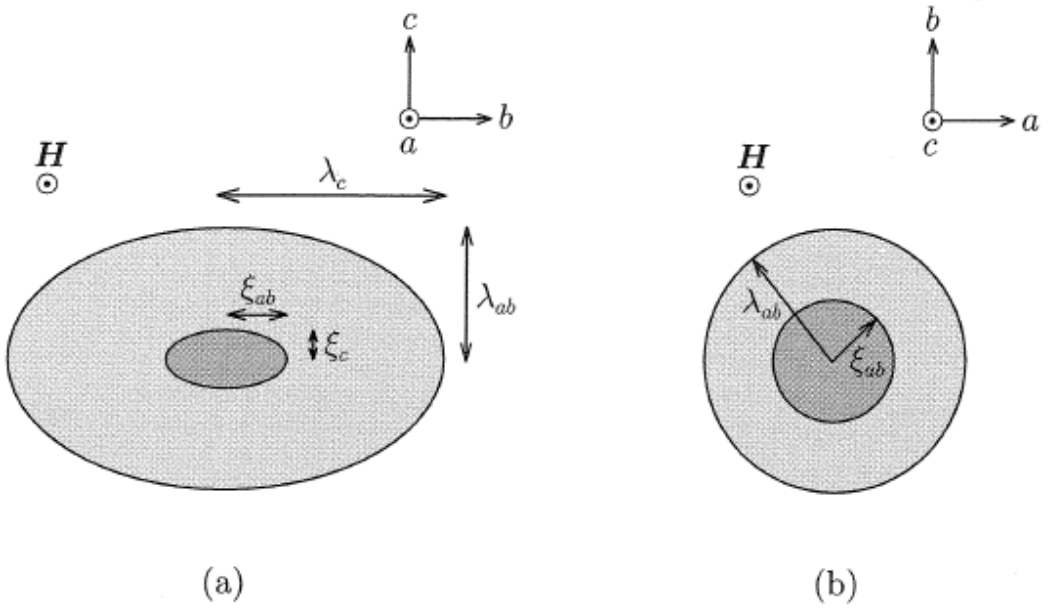

Figure 1-6. (a) Flux line in YBCO when the magnetic field is applied parallel to the CuO_2 plane; (b) flux line in YBCO when the magnetic field is applied parallel to the c-axis of YBCO.

The anisotropy in the effectiveness of the pinning centers in YBCO, in addition to the anisotropy of its crystal structure, makes the in-magnetic field critical currents of these materials highly anisotropic (Figure 1-7) [34]. Thus, the engineering of artificial pinning centers that can be incorporated into the YBCO matrix and decrease the anisotropy of critical currents is highly desirable. A significant improvement in the critical current over the full range of angles between the magnetic field and the YBCO films has been achieved by incorporating nanoparticles in the YBCO films. RE_2O_3 (e.g., Y_2O_3) are nanoprecipitates that are commonly incorporated into YBCO, and they are formed by the deviation from the YBCO 1:2:3 stichometry [35]. The RE_2O_3 precipitates act as strong 3D pins and they were shown to enhance the critical currents especially at temperatures higher than 65 K [36]. BZO ($BaZrO_3$) nanoparticles were also successfully incorporated into YBCO using Metal Organic Deposition (MOD), resulting in achieving

highly isotopic in magnetic fields critical currents [37, 38]. 1D pinning centers were later successfully incorporated into YBCO, first using ion irradiation that resulted in improving the critical current in the irradiation direction [39], and then by the successful growth of self-assembled perovskite nanocolumns such as $BaZrO_3$ (BZO). The growth of BZO nanocolumns resulted in the enhancement of the critical current over a wide range of angles and particularly when the magnetic field is applied parallel to the c-direction of YBCO, the direction over which these columns grow [40, 41].

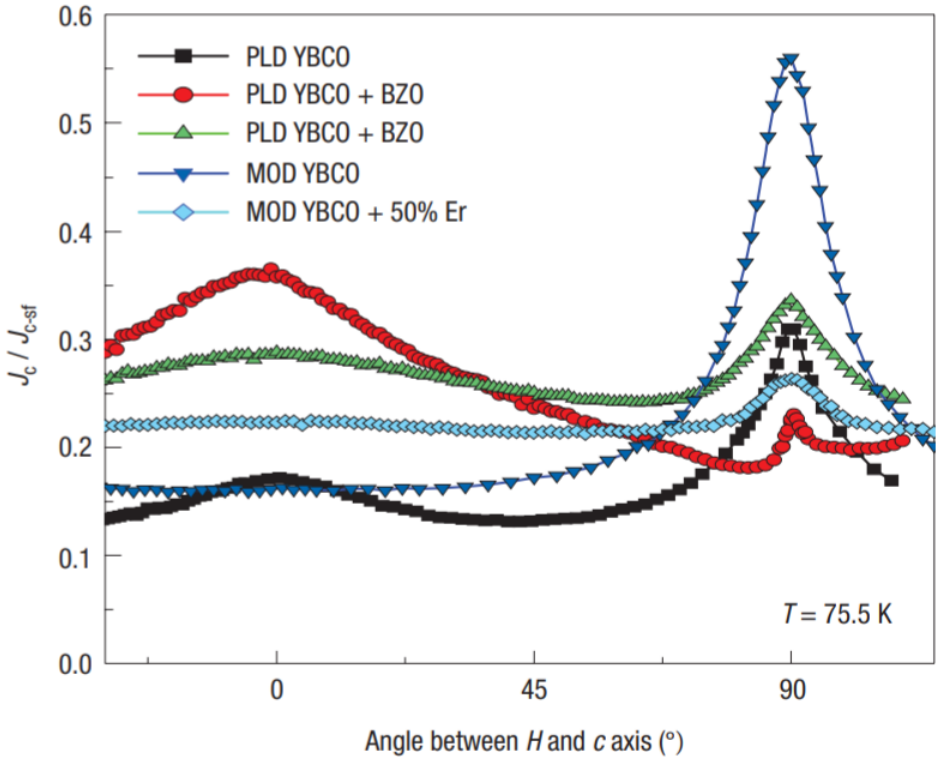

Figure 1-7. Effect of different pinning centers that are introduced by different processes on the angular dependence of critical current density J_c at 75.5 K and 1T. J_c is normalized to the self-field J_c for clarity.

Selvamanickam et al. successfully incorporated 2D defects into bulk YBCO via high-temperature uniaxial and isostatic deformation, which resulted in an increase in the dislocation density leading to an enhancement of the pinning over a wide range of angles

in multitextured bulk YBCO [42]. Because 2D defects are naturally present in YBCO films, no significant efforts have been made to extrinsically incorporate such pinning centers into the YBCO matrix. Stacking faults are an example of 2D pinning centers that naturally exist in YBCO, and they have been shown to enhance the critical current, especially when the magnetic field is applied parallel to the a–b-direction of the YBCO film at high temperatures, above 65 K [34, 43]. These stacking faults are usually an extra CuO_2 plane.

1.3. Synthesis of REBCO thin films

Critical currents decrease exponentially when crossing grain boundaries; above an angle of misorientation of approximately 5-10°, a drastic drop in critical current occurs [44-46]. Hence, the conventional bulk fabrication processes limit the potential performance that can be achieved by YBCO.

Ion Beam Assisted Deposition (IBAD), Rolling Assisted Biaxially Textured substrate (RABiTs), and Inclined-Substrate Deposition (ISD) have been developed to fabricate biaxially textured substrates. Using these substrates, long and flexible textured REBCO (RE=Rare-earth, B=Ba, C=Cu) films have been produced [47, 48].

1.3.1. Substrate Development technologies

The buffer layer in REBCO tapes consists of three principal components: a diffusion barrier, a nucleation layer, and a biaxially textured template. Ni-based alloys are usually used as substrates in RABiTs technology and a buffer layer of YSZ acts as a diffusion barrier to Ni. Different buffer architectures are used in RABiTS including $CeO_2|YSZ|CeO_2$ and $CeO_2|YSZ|Y_2O_3$.

In the IBAD technology, a buffer layer of $Gd_2Zr_2O_7$, MgO, or YSZ is vacuum-deposited on top of a polycrystalline substrate such as Hastelloy or stainless steel. The texture of the buffer is controlled by ion bombardment at a specific angle to the film to eliminate undesired grain orientations during buffer deposition.

These technologies allow the growth of single crystal-like substrates. And their texture is transferred to the REBCO layer using several techniques such as Chemical Vapor Deposition (CVD), Metal Organic Deposition (MOD), and Pulsed Laser Deposition (PLD).

1.3.2. Deposition techniques of the REBCO thin film

The biaxial texture of the substrates that were discussed previously can be transferred to the REBCO thin films because of the excellent lattice match between them. The techniques used to deposit the REBCO film include both physical and chemical vapor deposition methods (Figure 1-9 [49]). PLD is one of the most frequently-used physical deposition techniques, where a pulsed laser beam is focused on a target of the material that is to be deposited. The vaporized material from the target then deposits on the heated substrate. This process requires a high vacuum system and stoichiometric films can be made compared to the chemical vapor deposition techniques such as CVD and MOD. In chemical vapor deposition, volatile precursors are brought into contact with the heated substrate where the deposition occurs. Use of vapor deposition processes allows higher deposition rates to be achieved. The structure of the final REBCO film is presented in Figure 1-8 [50].

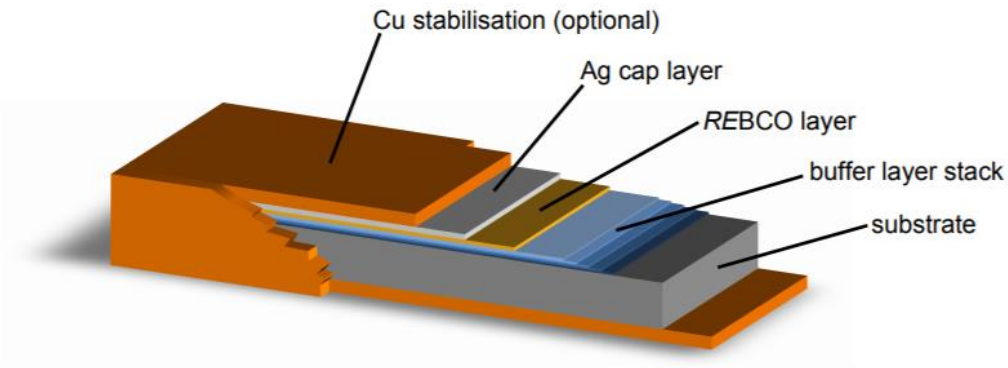

Figure 1-8. Schematic of the final structure of REBCO film.

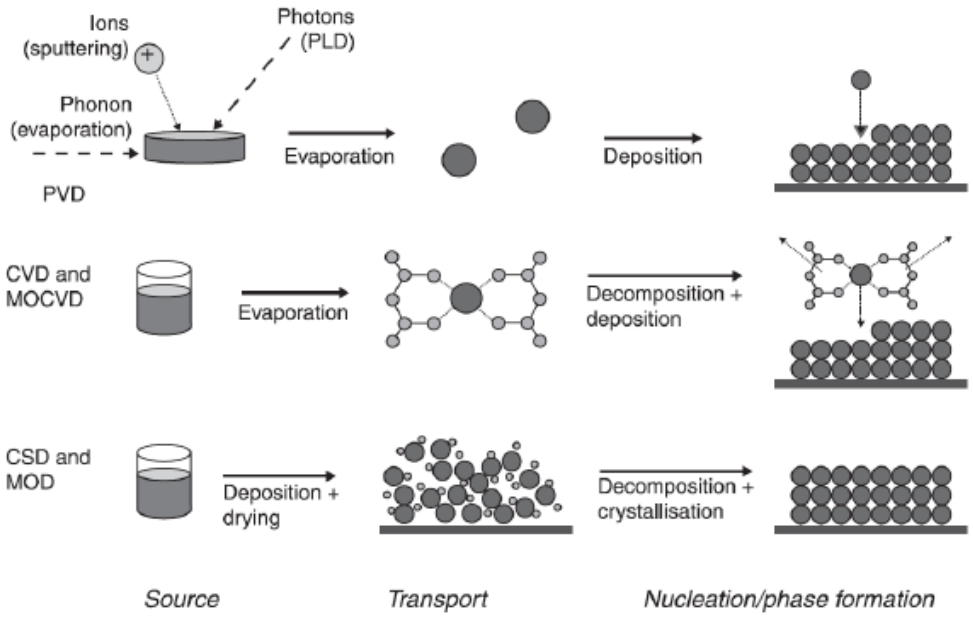

Figure 1-9. Schematic of different chemical and physical deposition processes.

1.4. Challenges for REBCO thin films

Because of its promising properties and the potential to make long thin films, REBCO is one of the most studied HTS materials. However, developing REBCO films that can compete in several applications, such as motors and magnet applications, many challenges such as the thickness dependence of critical current and the complex pinning

mechanisms that are observed in HTS superconductors and particularly in REBCO, have to be overcome.

1.4.1. Thermal fluctuations and pinning modeling

Because of their small coherence length and high T_c, high-temperature superconductors are susceptible to strong thermal fluctuations. These thermal fluctuations cause the movement of the vortex lines because they allow them to exceed the energy barriers that pin them to the non-superconducting pinning centers, causing flux creep. The movement of the vortices reduces the critical current capabilities of HTS superconductors. Thermal fluctuations are characterized by the Ginzburg number, Equation (1-5), as

$$G_i = \frac{1}{2}\left(\frac{2\pi k_B T_c \mu_0 \lambda^2}{\varphi_0 \zeta_c}\right)^2, \qquad \text{Equation (1-5)}$$

where ζ_c is the c-axis coherence length. Since YBCO has a T_c of about 92 K and is highly anisotropic, it has a G_i of about 10^{-2} compared to a G_i of about 10^{-8} in LTS superconductors. The direct consequence of the strong thermal fluctuations in HTS is that its irreversibility magnetic field H_{irr} is lower than its H_{c2} (H_{irr} is the magnetic field at which J_c=0). Thus, the mixed phase in the magnetic field–temperature diagram for HTS superconductors is divided into two phases: a solid phase where the vortices are pinned, and a liquid phase where the vortices move because of thermal fluctuations (Figure 1-10) [11].

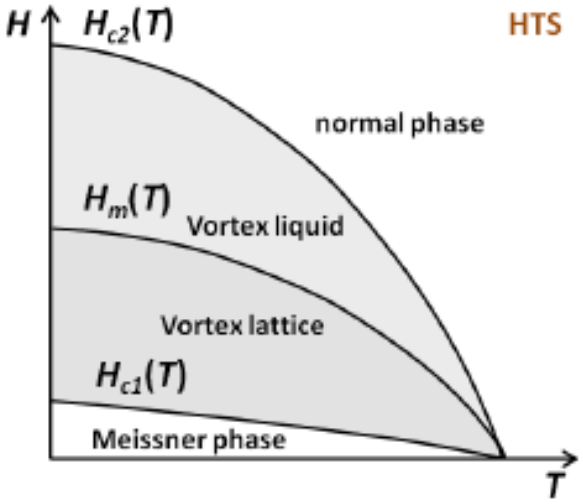

Figure 1-10. H-T diagram of HTS type II superconductors. H_m is transition of the vortex solid lattice to a vortex liquid phases.

Most applications, and in particular the high temperature magnet application, are limited by the difference between H_{c2} and H_{irr}. Therefore, controlling the pinning in REBCO is required to increase H_{irr} and satisfy the requirements of these applications. Understanding the pinning mechanisms in REBCO can enable the engineering of REBCO materials with higher critical currents and less sensitive to applied magnetic fields and thermal fluctuations, which is the focus of this thesis.

Because of the large thermal fluctuations that are present in the operational regime of HTS, the influence of pinning mechanisms in HTS and LTS is different. Pinning centers present in REBCO are classified according to their nature as correlated strong flux pinning centers and randomly-distributed uncorrelated flux pinning centers [51]. The random pinning centers include mostly 0D pinning centers such as crystal defects, oxygen vacancies, and cation disorders [29], while the strongly-correlated pinning centers include 1D and 2D pinning centers such as grain boundaries, dislocations, and nanorods, including BZO and BHO [29, 51]. The uncorrelated pinning

centers contribute mainly to the weak pinning regime where the critical current density as a function of temperature is described using the following Equation [52-54].

$$J_c^{wk}(T) \approx \mathrm{J}_{\mathrm{c0}}^{wk} \exp\left(-\left(\frac{T}{T_0^{wk}}\right)\right), \qquad \text{Equation (1-6)}$$

where J_{c0}^{wk} is the contribution of the uncorrelated weak pinning centers to the zero-temperature critical current, and T_0^{wk} is the characteristic temperature that fixes the energy scale of the pinning centers contributing to the weak uncorrelated pinning [52, 55]. T_0^{wk} has been reported to be in the range of 10 K for REBCO films [54, 56]. J_c^{wk} is observed to exponentially decay as a function of *T* [52].

The correlated pinning centers, however, contribute mainly in the strong pinning regime, and its critical current temperature dependence is described by the following equation [37, 52, 57, 58].

$$J_c^{str}(T) \approx \mathrm{J}_{\mathrm{c0}}^{str} \exp\left(-3\left(\frac{T}{T_0^{str}}\right)^2\right), \qquad \text{Equation (1-7)}$$

where J_{c0}^{str} is the contribution of the strongly correlated pinning centers to the zero-temperature critical current, and T_0^{str} is the characteristic temperature that fixes the energy scale of the pinning centers contributing to the strong correlated pinning [55]. T_0^{str} has been reported to be in the range of 60 K for REBCO films [54]. J_c^{str} is observed to exponentially decay as a function of T^2 [52].

REBCO films studied in this thesis contain a rich pinning landscape (Figure 1-11) [34] because of the mixture of correlated pinning that is introduced mainly by the BMO nanorods, and weak pinning that naturally exists in the REBCO matrix and that is amplified by the lattice mismatch between the BMOs and the REBCO matrix. To

separate the contributions of the weak and strong pinning to the total J_c, the field dependence of the weak pinning critical current can be fitted using the collective vortex pinning model, as shown in Equation (1-8).

$$J_c^{rand}(H\varepsilon) = \mathrm{J}_\mathrm{c}^{rand}(0)\left(1+\frac{H\varepsilon}{H_0}\right)^{-\mathrm{p}}\left(1-\frac{H\varepsilon}{H_{irr}}\right)^{q}, \qquad \text{Equation (1-8)}$$

where $\varepsilon(\theta) = \cos^2(\theta) + \gamma^{-2}\sin(\theta)$ is from the effective mass model where, based on different γ values, the angular dependence of J_c can be fitted as a function of the scaled magnetic field, $H\varepsilon(\theta)$, especially at low temperatures where the pinning is dominated by the weak pinning. γ is called the anisotropic factor, and it is usually between 5 and 7 for REBCO films [59-61]. H_{irr} and H_0 are the irreversibility and the accommodation magnetic fields.

The formula shown in Equation 1-7 is a combination of the Bean or Kim models if p=0 or 1 [62-65]. For REBCO films, q ranges from 2 to 3 [54, 66] and p ranges from 0.5 to 0.6 [54, 67].

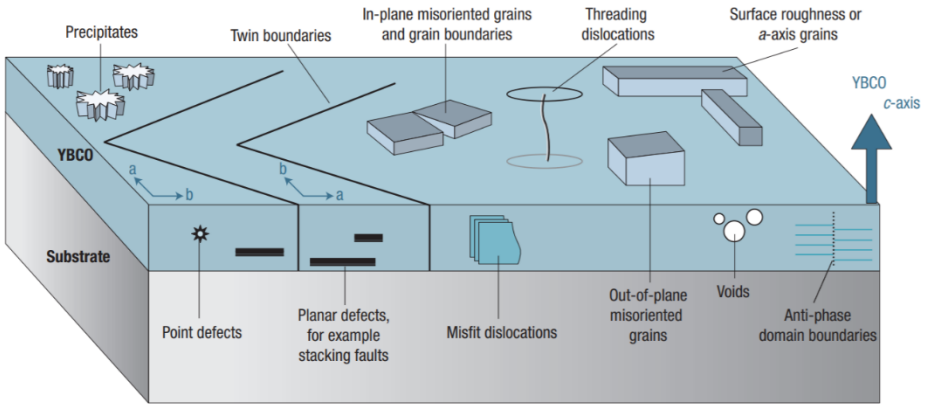

Figure 1-11. Defects that can act as pinning centers in REBCO films.

Further understanding of the complex pinning landscape that is present in REBCO through modeling can lead to an improvement in critical current and its angular and field dependences.

1.4.2. Thickness dependence of J_c:

It has been reported that REBCO films show a thickness dependence of critical current density. While there is no prompt physical explanation for the causes leading to this observation, a higher risk of developing material imperfections such as misoriented grains, voids, and secondary phases with thickness can explain the observed degradation with increasing film thickness. In a systematic study of the evolution of the microstructure of 5% BZO and 5% Y_2O_3 doped REBCO with increasing thickness, Zhou et al. showed a coarsening of grains and grain boundaries starting rapidly from the first 1.6 μm (Figure 1-12) [68].

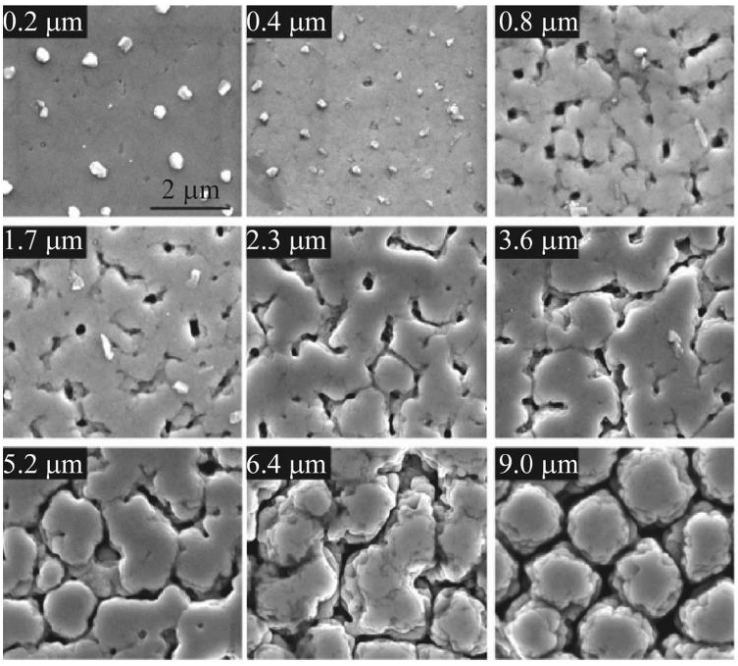

Figure 1-12. SEM images of the surface morphology variation with increasing REBCO films thickness from 0.2 to 9 μm.

1.5. Objectives of the dissertation:

High critical current I_c as well as reduced anisotropy and a weak in-magnetic field dependence of I_c are necessary for all REBCO applications [34]. Since the critical current density J_c was found to decrease significantly with increasing thickness, expanding the effective REBCO cross-section is the straightforward way to enhance the I_c of REBCO films [69]. Recently, an advanced metal-organic chemical vapor deposition (A-MOCVD) system was developed at the University of Houston, aiming at better control of the REBCO growth conditions [70]. The aforementioned system enabled deposition thick a-axis grain-free REBCO films of up to 5 μm in thickness with high critical currents.

In this dissertation, the outcome of a study on the thickness dependence of superconducting properties (critical current density J_c and superconducting transition temperature T_c) and the microstructure of A-MOCVD-made REBCO films with different thicknesses up to 4.8 μm is detailed.

Then, in a second part, the effect of introducing BMO (B=Ba, M= Hf, Zr…) artificial pinning centers on anisotropy and in-magnetic field dependence of the critical current of thick A-MOCVD-made REBCO films is analyzed. The effect of their addition on the critical current over a wide range of temperatures (4.2 to 77 K) has been revealed by varying the dopants (Zr, Hf and Nb) and the density of the BMO.

Later, methods of reducing the anisotropy of BZO-doped REBCO are examined. One method is combining BZO-doping with RE-doping. Another method is high temperature tensile-creep deformation of fully-processed BZO-doped REBCO tapes.

Finally, a model was developed to predict the critical current at low temperatures and high magnetic fields. Artificial neural networks were applied to predict the critical current at temperatures ranging from 4.2 K to 40 K out of 65 K measurements. This statistical model was combined with a physics-based model to extend the predictions to higher magnetic fields up to 31 T.

Chapter 2. Experimental Methods and Technical Background

In this chapter, experimental methods used to collect the data presented in the thesis are described. The selected methods include the advanced metal-organic chemical vapor deposition (A-MOCVD) system used to make the rare-earth barium copper oxide (REBCO) films in addition to the systems and methods used for electromagnetic and material characterizations of the REBCO films.

2.1. Deposition of the REBCO Film Using A-MOCVD

The REBCO films described in this thesis were prepared using a roll-to-roll A-MOCVD reactor. The use of this improved MOCVD system permitted better control of the deposition process through the use of direct ohmic heating in a closed loop with non-contact temperature measurement [71].

In contrast to conventional MOCVD, in which the tape is in contact with a curved susceptor for the purpose of heating the substrate in precursor flow, the susceptor is eliminated in the advanced system, and the substrate is directly heated by current b through two rollers. The tape is heated mainly through the resistance of the Hastelloy which is about 1 Ω. An array of optical probes positioned on the bottom of the tape are used to monitor the temperature of the tape through the radiation in the infrared range that is emitted during heating. A quartz plate placed between the optical probes and the substrate avoids precursor depositions on the optical probes [49]. The precursor flow is constrained between two plates that are close to each other [71]. This narrow gap enables a higher precursor-to-film conversion efficiency [49, 71]. A schematic of the A-MOCVD system is presented in Figure 2-1.

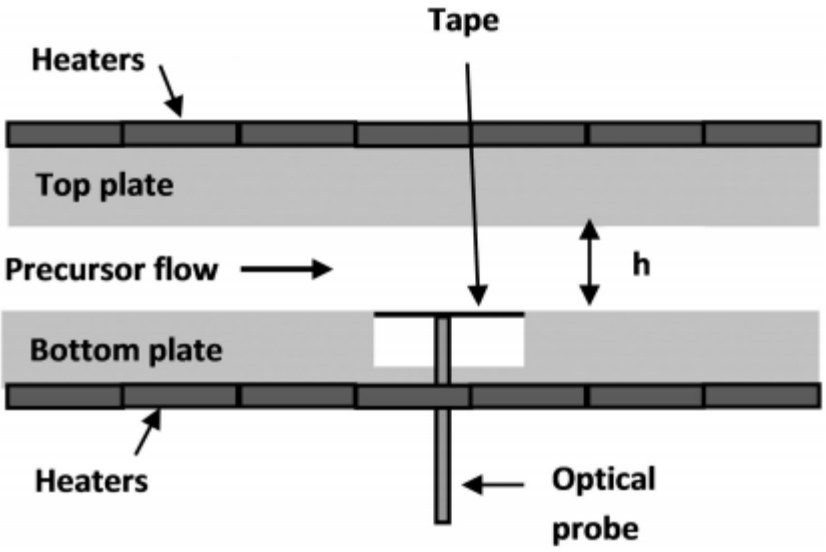

Figure 2-1. Schematic of the flow pattern in the advanced metal-organic chemical vapor deposition (A-MOCVD) reactor.

The buffer stack on 50 µm C-276 Hastelloy substrate, on top of which the REBCO layer is grown, is constructed in the following sequence: 180 nm Al_2O_3|7 nm Y_2O_3|70 nm of ion beam-assisted deposition (IBAD) MgO and homo-epitaxy MgO|40 nm $LaMnO_3$. Hastelloy C-276 is a nickel-based alloy with a melting temperature of approximately 1350 °C. The Al_2O_3 layer provides a diffusion barrier that prevents Ni diffusion from the Hastelloy during deposition at room temperature. The Y_2O_3 layer provides a platform for nucleation of the IBAD MgO layer. The IBAD and the homoepitaxial MgO layers in addition to the lanthanum manganese oxide (LMO) layer form a seed stack used to grow the epitaxial REBCO film.

After the deposition of the REBCO film, a silver layer is deposited on both sides of the film using a roll-to-roll sputtering system in which silver (2 µm) is sputtered onto the REBCO side of the film, and 0.5 µm of silver is sputtered onto the Hastelloy side.

The silver layer protects the REBCO film and provides low resistivity electrical contact needed for critical current measurements.

The silver sputtered samples are then oxygenated; the tape is heat treated for 2 h at 500 °C in an oxygen flow to enable the transition of the REBCO crystal structure from the tetragonal non-superconducting phase to an orthorhombic superconducting phase as discussed in the Introduction chapter. A 70 standard cubic centimeters per minute (SCCM) oxygen flow rate is used during this process. After oxygenation, the REBCO coated conductor is used for testing and characterization by different methods.

2.2. Electromagnetic Characterization of the REBCO Films

Critical current measurements were performed in a magnetic field with two different systems to determine the critical current values of the A-MOCVD-grown REBCO films studied in this thesis. In the first system, direct transport critical current measurements were obtained, while in the second system, critical current values were obtained indirectly from the magnetization measurements.

2.2.1. Transport Measurements

In transport measurements, the four-probe method was used. This method is a low-noise measurement technique that allows the detection of the superconductor to resistive transition as shown in Figure 2-2. In this method, two voltage tabs are directly soldered on the REBCO-coated conductor while the current is fed to the sample either by soldering or pressing the current leads on both sides of the sample. The current was supplied via a DC power supply, and the voltage was detected using a nanovoltmeter (Keithley 2182). In order to avoid heating during these high current measurements, a

narrow bridge of 1 to 0.3 mm width was patterned on the sample using chemical etching as shown in Figure 2-3. A 1 µV/cm criterion was selected to define the I_c values.

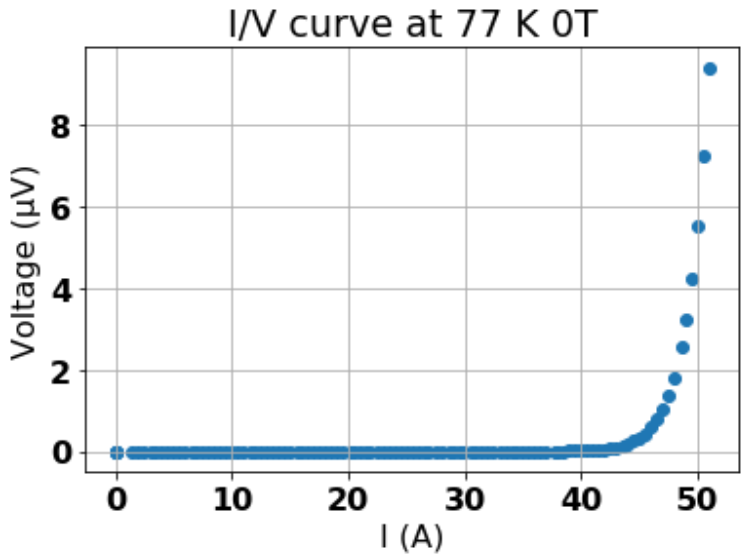

Figure 2-2. Transport measurement of current/voltage (I/V) curve using the four-probe method. The critical current value was defined using a criterion of 1 µV/ cm.

A cryogen-free J3100 system made with a superconducting magnet was used for transport measurements at temperatures as low as 4.2 K and magnetic fields up to 9 T. Cryogenic temperatures are achieved in this system using two compressors that drive moving pistons with regenerators (the compressors do not have any cold moving parts). Controlling the expansion of compressed helium gas allows cryogenic temperatures to be achieved.

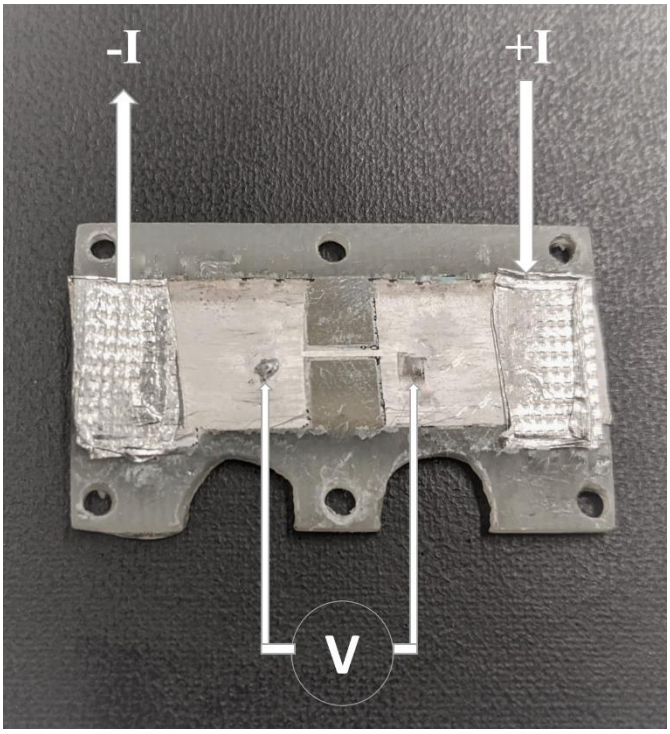

Figure 2-3. Example of a sample used for the in magnetic field transport measurement: a ~ 0.6 mm bridge was patterned on the sample using chemical etching. The sample was glued onto a G10 board, and an indium sheet was used to press it on the current leads.

Figure 2-4. Photograph of the platform over which the sample is mounted. The platform is equipped with flexible superconducting current leads and a potentiometer for position reading.

The constituents of the system can be divided into three groups: (1) the cryostat with an inner diameter of 63.6 mm; (2) the probe in which the REBCO sample is mounted and inserted in the cryostat during the measurements; and (3) a rack of electronics that allow low-noise measurements to be obtained in addition to controlling the temperature and magnetic field.

The probe is equipped with a stepper motor and a potentiometer for angular dependence measurements. Current contact is established by pressing the sample on two copper blocks while the voltage tabs are directly soldered to the sample surface as shown in Figure 2-3. The probe is also equipped with high-temperature superconducting (HTS) current leads to reduce heating during transport measurements (Figure 2-4).

The electronics rack consists of a Keithley 2182 nanovoltmeter for the voltage reading during the four-probe measurement, a Lakeshore 336 Temperature controller that controls the many temperature sensors existing in the system (Figure 2-5), a 600A power supply for the transport measurements, a SMS 120C-4Q bi-polar magnet power supply, and a data acquisition panel controlling the motion of the stepper motor.

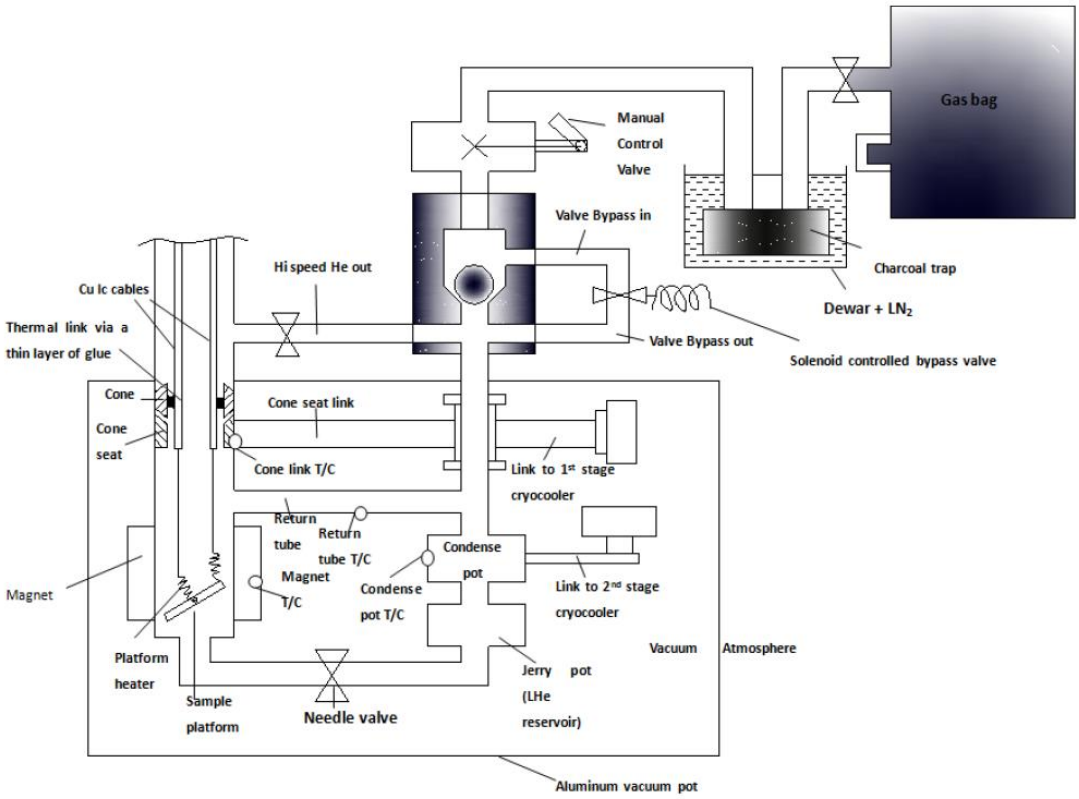

Figure 2-5. Schematic of the J3100 system.

2.2.2. Magnetic Measurements

A physical property measurement system (PPMS) system by Quantum Design was used to measure the magnetic critical current. This system consists of a 14 T magnet and can operate at temperatures as low as 4.2 K. It is equipped with a vibrating sample magnetometer (VSM) in which an approximately 3.5 mm × 3.5 mm sample can be measured. Magnetization hysteresis loops are obtained at different temperatures and magnetic fields up to 14 T. The magnetic field is swept at a constant rate of 100 Oe/s.

The Bean model was used to determine the critical current values as described by equation 2-1 [72].

$$J_c = 20\frac{\Delta M}{a(1-\frac{a}{3b})}\ , \qquad \text{Equation (2-1)}$$

in which a and b are the width and the length of the sample, respectively, and ΔM is the width of the magnetization hysteresis loop at a given magnetic field. This measurement is always conducted with the magnetic field applied perpendicular to the film. The criterion to define the critical current value using the VSM system is ~ 0.15 μV/cm, which results in lower critical current values than from transport measurements [73].

2.3. Critical Temperature Measurements

Critical temperature (T_c) was measured inductively with the REBCO film between two coils. The first coil was excited using an alternating current (AC) while the second coil (the pick-up coil) was connected to a lock-in amplifier to measure the induced voltage. The sample and the two coils were then immersed in a liquid nitrogen bath. The voltage in the pick-up coil was measured while the liquid nitrogen evaporates allowing the REBCO film to warm up.

Below T_c, the magnetic field from the exciting coil is screened by the superconducting film. When T_c is reached, the magnetic field penetrates the sample, and a voltage appears in the pick-up coil. Figure 2-6 shows an example of the induced voltage measured in the pick-up coil while the REBCO film was warming up from 89 to 95 K.

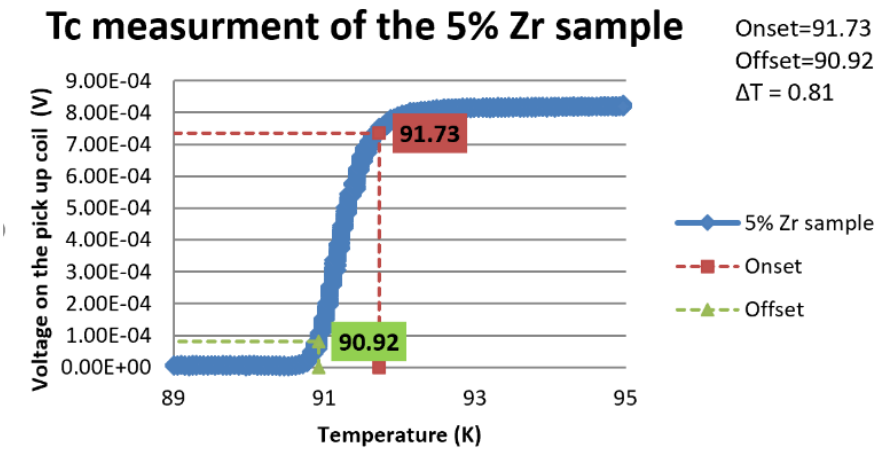

Figure 2-6. Critical temperature (T_c) measurement of a 5 mol% Zr-doped REBCO film. Below ~91 K, zero voltage was measured by the pick-up coil. The voltage from the pick-up coil rises sharply until ~ 92 K.

2.4. Induced-Coupled Plasma Mass Spectrometry (ICP-MS)

Induced-coupled plasma mass spectrometry (ICP-MS) was used to measure the composition of the REBCO films to a resolution of 1 part per billion (ppb) concentration. The concentration of each element was calculated by dividing the measured concentration by its atomic weight. In order to normalize the atomic percentage of each elements, the element's relative concentration was divided by the sum of the relative concentrations of all of the measured elements.

2.5. Transmission Electron Microscopy

The microstructure of the samples was studied with a JEOL 2000FX transmission electron microscope (TEM). The samples were prepared for TEM with the focused ion beam (FIB) and Gatan PIPS milling techniques. The thickness of the samples was also checked by the FIB technique.

2.6. X-ray Diffraction XRD

The crystalline structure of the REBCO film was studied using a general area diffraction system (GAADS) by Bruker with a Cu Kα (λ = 1.5418 Å) source and two-dimensional (2D) detector. The X-ray tube operates at 40 kV and 40 mA.

Chapter 3. Toward thickness-independent critical current density in Zr-doped REBCO using Advanced MOCVD

3.1. Introduction

In early stages of development of REBCO-coated conductors, a thickness dependence of critical current was reported, with the critical current density decreasing rapidly within the first 2 μm of the REBCO film [11, 34, 69]. Extending this threshold thickness or achieving a thickness-independent critical current is important to increase the performance of REBCO tapes.

The reason for the thickness dependence of the critical current density (J_c) has been subject to debate. The degradation of J_c with increasing thickness could be due to a reduction in the effective cross-section area because of microstructural detractors or to a change in the vortex pinning effectiveness.

The first reason for the degradation seen in J_c with increasing thickness is the formation of misoriented grains along the a-axis, which typically occurs when the REBCO film thickness exceeds 1.5 μm. Using the Advanced MOCVD process, films up to 5 μm in thickness nearly free of a-axis misoriented grains were grown [70, 71, 74]. This enabled the thickness dependence of J_c to be studied to higher thicknesses without the complicating effect of microstructure degradation.

The addition of BZO nanorods that grow along the c-axis orientation of the film enabled the enhancement of the critical current, especially in the strong pinning regime. For films containing strong pinning centers, J_c is determined by the interactions between the pinned vortex lines at the scale of the spacing of pinning centers; thus, J_c is

controlled by the pinning center spacing and not the thickness of the film when the film thickness exceeds the pin spacing [11, 75, 76]. In addition to being limited to a low thickness threshold due to the degradation of the films' crystallinity, most studies on the effect of thickness on critical current focused only on the self-field critical current at 77 K. Only a few studies have been conducted on the in-magnetic field critical currents where the addition of strong pinning mechanisms can lead to a weak thickness dependency of J_c [11, 73, 77].

In this chapter, critical currents of 5 mol% Zr-doped films made by Advanced MOCVD with different thicknesses (up to 4.8 µm) were studied to investigate the effect of thickness on critical current. These samples contained both BZO nanorods and RE_2O_3, offering a rich strong pinning landscape effective over a wide range of magnetic field orientations and temperatures. The microstructure was investigated with TEM and XRD to corroborate the critical current values measured. The superconducting temperature transition with increasing thickness was also assessed.

3.2. Experimental Methods

All samples presented in this chapter were deposited using the Advanced MOCVD system. The lattice parameters were measured using the GAADS system presented in Chapter 2. Omega scan ($\Delta\omega$) was used to calculate the out-of-plane texture by analyzing the REBCO-005 peak while the pole figure ($\Delta\varphi$) of the REBCO-103 peak was used to analyze the in-plane texture. The standard deviation of $\Delta\varphi$ was measured to be ~0.719°, whereas the standard deviation of $\Delta\omega$ was measured as ~0.024°, which leads to a standard deviation of 0.0013° in the REBCO c-lattice constant. The films were

grown and the XRD analysis were performed by Dr. Rudra Pratap [49]. TEM microstructures were obtained by Dr. Eduard Galstyan.

3.3. Results and Discussion

Figure 3-1 illustrates the in-plane and out-of-plane textures of 11 5% Zr-doped REBCO samples made by Advanced MOCVD with thicknesses ranging from approximately 1.1 to 4.8 μm. The full-width-at-half-maximum (FWHM) values of the texture spreads were used to characterize the change in microstructure with increasing film thickness. The FWHM of the REBCO-005 peak (out-of-plane texture) of the 11 samples presented in Figure 3-1 varied between 0.9° and 1.5°, whereas the FWHM of the REBCO-103 peak (in-plane texture) varied between 2.2° and 3.5° [49]. The sharp in-plane and out-of-plane peaks qualify the sharp crystallographic texture achieved by the Advanced MOCVD process. The nearly constant FWHM values with increasing film thickness indicate the absence of any systematic change in crystallinity and texture as thickness changes.

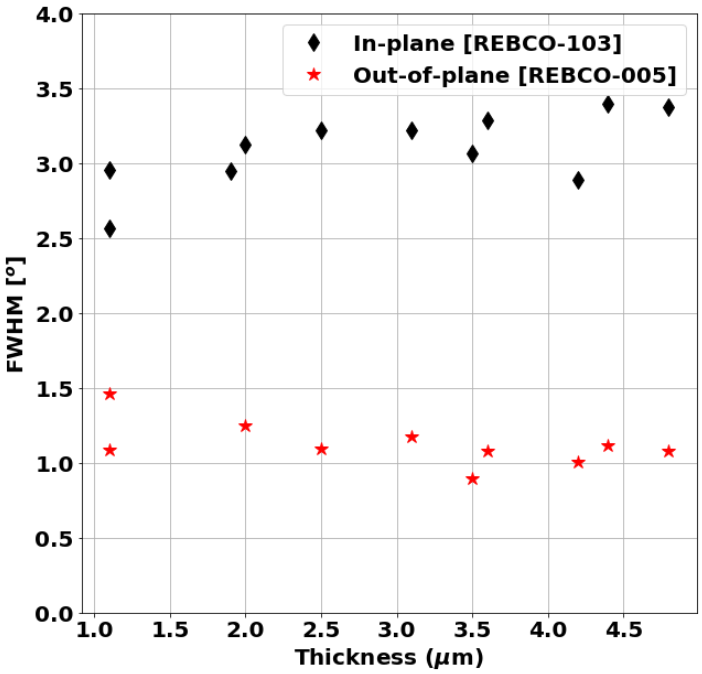

Figure 3-1. Consistent out-of-plane and in-plane texture achieved in 5% Zr-doped REBCO films made by Advanced MOCVD with film thicknesses ranging from 1.1 to 4.8 μm.

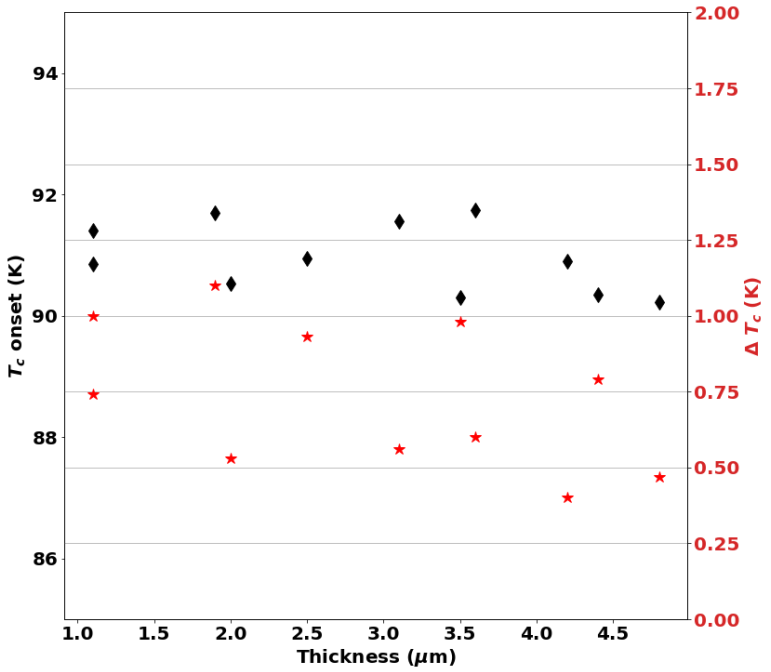

Figure 3-2. Onset T_c above 90 K in 5% Zr-samples with film thicknesses ranging from 1.1 to 4.8 μm.

Figure 3-2 characterizes the change in critical transition temperature (T_c) with thickness for 11 5% Zr-doped REBCO films with thicknesses ranging from 1.1 to 4.8 μm. The onset of T_c is defined as the temperature corresponding to 90% of the maximum voltage induced in the pick-up coil, whereas the transition width ΔT_c is defined as the difference between the temperatures corresponding to 90% and 10% of the maximum voltage induced (Figure 2-6). An onset T_c above 90 K was achieved in all samples. The narrow transition widths, independent of film thickness, is another indicator of the homogeneity in film crystallinity and the absence of secondary phases. Broad superconducting transitions indicate a degradation of the in-plane texture and an expansion in the c-lattice parameter of the REBCO unit cell [78]. T_c degradations have attributed to a decrease in charge carrier concentration, and lattice mismatch between dopants and REBCO have been reported to increase the c-lattice constant and induce charge transfer from the conducting CuO planes to the Cu-O chain [78-80]. BZO addition to the REBCO films without a significant degradation of T_c indicates that high-condensation energy can be achieved in these films, which leads to an enhancement in the upper critical current field H_{c2} and high flux pinning strength [78, 81, 82].

The c-axis lattice constant of 5% Zr-doped films with different film thicknesses (ranging from 1.1–4.8 μm) was determined by fitting the Nelson-Riley function [49]. No thickness effect was found on the c-lattice constant value, which ranged from 11.734–11.742 Å (Table 3.1) [49]. The consistent c-lattice constant confirmed that increasing film thickness did not affect crystallinity or composition, and no extra strain was created in these BZO-doped films.

Table 3-1. A consistent c-lattice constant in Advanced MOCVD made 5% Zr-doped REBCO films with thicknesses ranging from 1.1 to 4.8 μm.

	5 mol% Zr-doped REBCO			
Film thickness (μm)	1.1	2.5	3.5	4.8
REBCO c-lattice constant (Å)	11.735	11.734	11.742	11.734

Figure 3-3 shows the magnetic field dependence of critical current at 65 K with the magnetic field applied parallel to the c-axis of four 5% Zr-doped REBCO films with thicknesses ranging from 1.1 to 4.8 μm. Two different thickness dependencies of the critical current density were observed over this range of thicknesses. Above 4 T, all samples showed no thickness dependence of J_c (in fact, a nearly identical J_c value was observed). Below 4 T, a weak thickness dependence of J_c was observed because, while all samples exhibited a plateau in J_c between 0.2 and 2.5 T that resulted in a slower decay in J_c over this range of magnetic fields, the J_c values themselves differed. The 1.1 μm-thick film showed the highest self-field J_c (4.5 MA/cm^2) while the thicker films exhibited a nearly similar self-field J_c of ~3.2 MA/cm^2; however, the 4.8 μm-thick film had the highest J_c values over the plateau range.

The thickness dependence of J_c has been theoretically associated with the effect of strong thermal fluctuations by Gurevich [11, 75], who suggested that thermal fluctuations reduce J_c when the superconducting layer thickness is comparable to the spacing between the effective pinning centers. This predicts a thickness-independent J_c with increasing pinning center density and in thicker films. The effects of thermal fluctuations on J_c are also more pronounced when the magnetic field increases [75]. In

the field dependence of J_c of the four presented samples (Figure 3-3), J_c is likely significantly affected by thermal fluctuations when exceeding ~2.5 T. The presence of the plateau in J_c, where J_c is not affected by the changing magnetic field, is correlated with the high density of BZO nanorods achieved by Advanced MOCVD. The presence of the plateau (up to ~2.5 T) in all four samples indicates a consistency in the BZO nanorod density that is independent of the REBCO film's thickness. The transition field above which the thermal fluctuations have a more significant effect on the J_c has been reported to be 0.5 T in BZO-doped YBCO made by PLD [77] and 2 T in BZO-doped REBCO made by MOCVD [11].

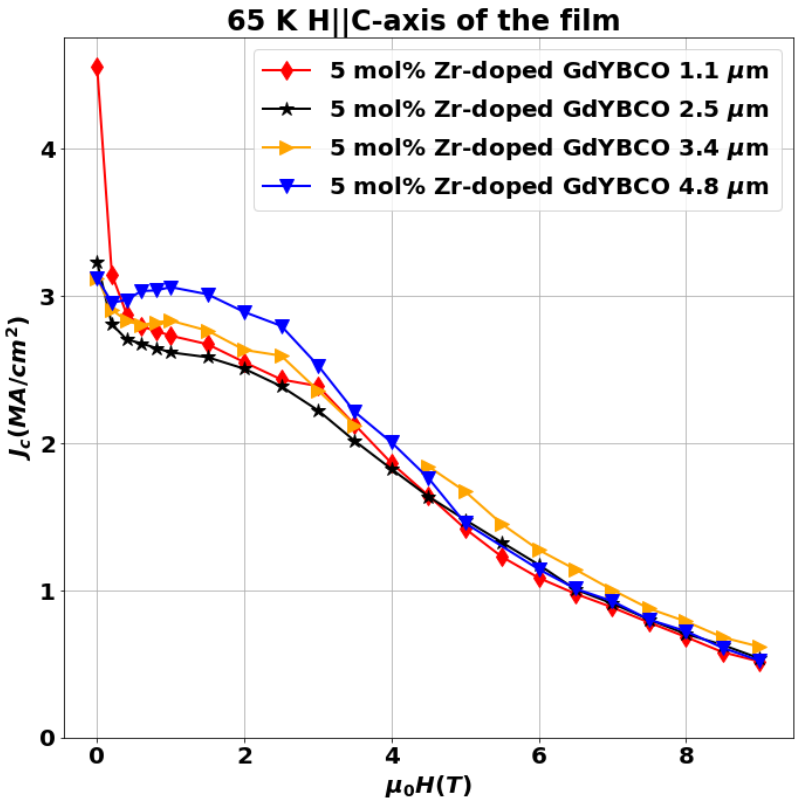

Figure 3-3. J_c (H||c) of 5% Zr-doped REBCO films with different thicknesses.

Figure 3-4 illustrates the pinning force $F_p(H) = J_c \times H$ at 65 K when the magnetic field was applied parallel to the c-axis of the films. The 4.8-μm film had the highest maximum pinning force (87 GN/m^3), while the thinner films displayed lower maximum pinning force values (79 GN/m^3, 74 GN/m^3, and 75 GN/m^3 for 3.4 μm, 2.5 μm, and 1.1 μm, respectively). The matching field, on the other hand, varied between 4–5 T; 4 T for the 4.8 μm- and 1.1 μm-thick films and 5 T for the remaining two samples. The matching field is the magnetic field where the maximum pinning force is achieved. At 65 K, with the magnetic field applied parallel to the c-axis of the film, the matching field correlates with the density of the BZO nanocolumns since the pinning at 65 K is dominated by the strong correlated pinning introduced by the BZO nanorods [83, 84]. A consistent matching field despite varying film thickness indicates that BZO nanorod density did not vary with thickness.

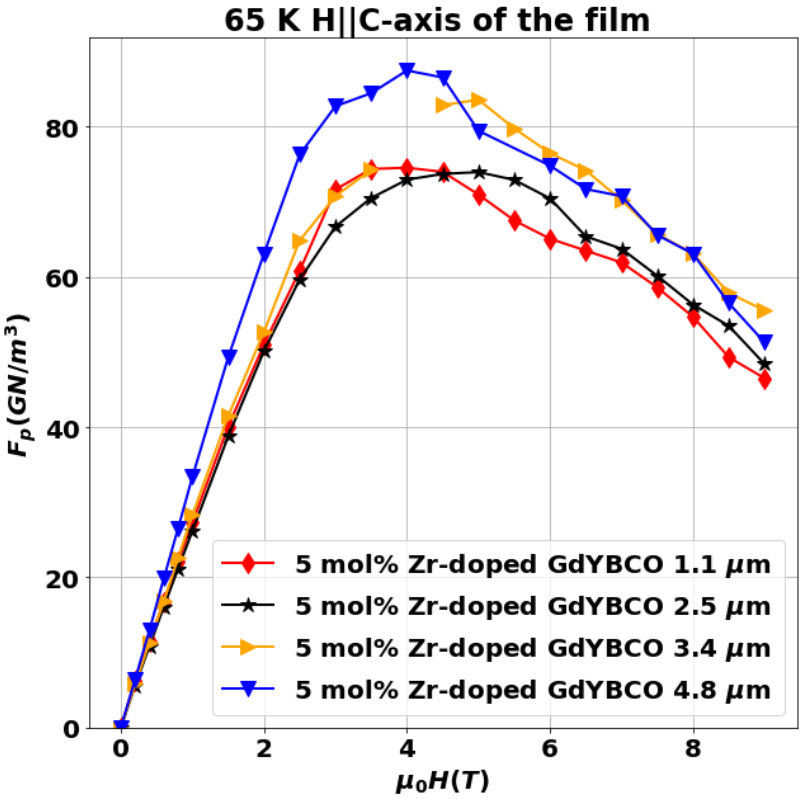

Figure 3-4. Evolution of the pinning force curve with film thickness when the magnetic field is applied parallel to the c-direction of four 5% Zr-doped REBCO films with different thicknesses, at 65 K.

A cross-section TEM of an approximately 4.1 μm-thick 5% Zr-added REBCO film is shown in Figure 3.5. The presence of continuous BZO nanorods along most of the film thickness is seen. The BZO nanorods had a bottle-like shape, with narrow sections averaging 3–4 nm in diameter and wide sections with average diameters up to 10 nm. The average spacing between the BZO nanorods was approximately 23 nm. RE_2O_3 nanoprecipitates were observed along the entire thickness of the film. A total of approximately 80 layers of RE_2O_3 with an average spacing along the c-axis of approximately 65 nm were observed. The spacing along the c-axis of RE_2O_3 and the spacing of BZO nanorods along the ab-direction were consistent along the entire

thickness of the REBCO film. Misoriented REBCO grains were noted near the substrate interface.

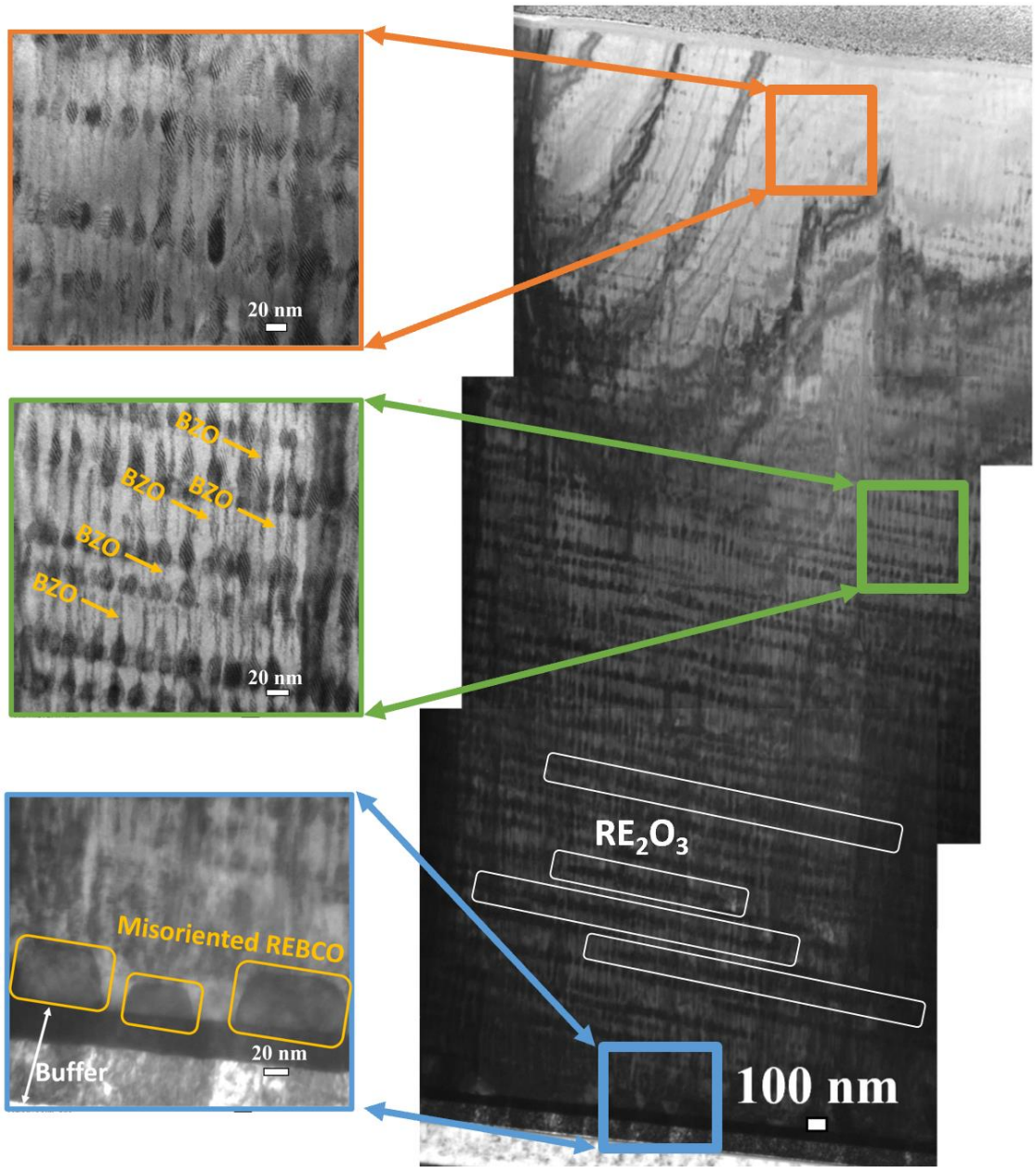

Figure 3-5. TEM cross-section of ~4.1 µm-thick 5% Zr-doped REBCO film made by Advanced MOCVD.

Table 3-2 displays the microstructural properties of 5% Zr-doped films of various thicknesses. A consistent average RE_2O_3 spacing along the c-axis is seen. The average spacing between the BZO nanorods was also independent of the film thickness, which is consistent with the comparable matching fields of films with different thickness as observed from pinning force curves at 65 K (Fig. 3.5). On the other hand, the average BZO diameter varied slightly from sample to sample, with all four samples showing bottle-shaped BZO nanorods [84].

Table 3-2. Overview of the microstructural features of 5% Zr-doped REBCO films of various thicknesses.

	5 mol% Zr-doped REBCO				
Thickness (μm)	1	1.7	2.6	4	4.1
Average BZO diameter (nm)	4.4[(a)(b)]	5[(a)(c)]	4.5[(a)(c)]	4.6[(a)(b)]	4.2[(a)(c)]
Average BZO spacing (nm)	25[(b)]	-	-	22[(b)]	23[(c)]
Average RE_2O_3 c-axis spacing (nm)	62[(c)]	65[(c)]	59[(c)]	55[(c)]	65[(c)]

[(a)] *Average diameter of the narrow portion in samples where bottle-like shaped BZO nanorods were observed.*
[(b)] *Value determined from plan-view TEM images.*
[(c)] *Value determined from cross-sectional TEM images.*

Figure 3-6 illustrates the angular dependence of J_c at 65 K and 1.5 T of 5% Zr-doped REBCO films with different thicknesses (ranging from 1.1–4.8 μm). All samples showed a similar shape of angular dependence; the thickest sample showed the highest J_c when the magnetic field was applied parallel to the c-axis of the film. However, no

notable differences in the J_c at B||ab and minimum J_c were seen in films of all thickness, which correlates with the consistent RE_2O_3 precipitate average spacing along the c-axis as reported in Table 3.2.

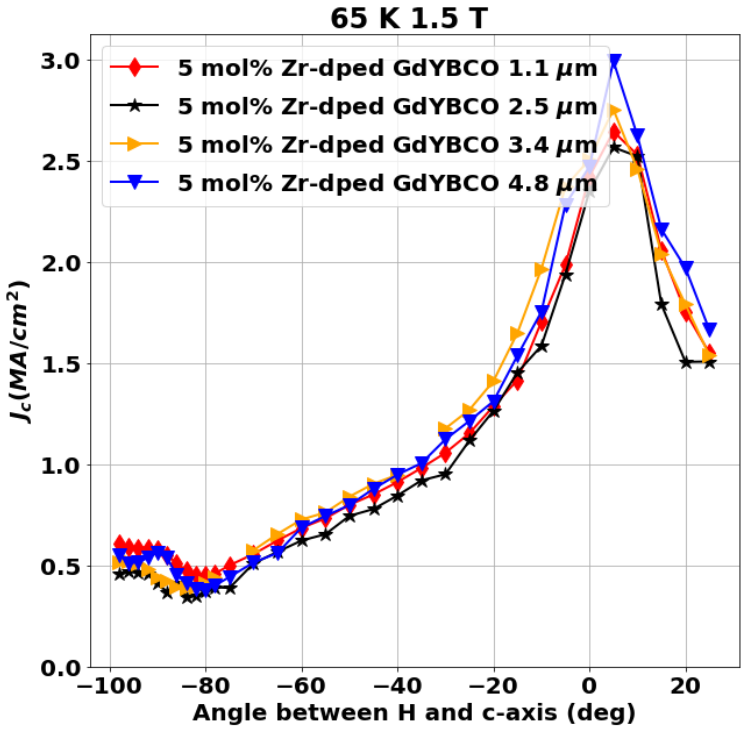

Figure 3-6. Angular dependence of Jc at 65 K and 1.5 T of four 5% Zr-doped REBCO films with thicknesses ranging from 1.1 to 4.8 μm.

3.4. Conclusions

5% Zr-doped REBCO films up to 4.8 μm-thick have been demonstrated by the Advanced MOCVD process without degradation of crystallinity and formation of misoriented a-grains. At 65 K and 1.5 T with the magnetic field applied along the c-axis of the film, a 4.8 μm-thick film had an I_c of 1722 A/12 mm which corresponds to a J_c of 3 MA/cm^2.The thinner films had J_c in the range of 2.5-2.7 MA/cm^2 under the same conditions. A maximum of pinning force at 65 K with the magnetic field applied along the c-axis of the film of 87 GN/m^3 was achieved in the 4.8 μm-thick film at a matching field of 4 T.

In the next chapter a detailed analysis of the electromagnetic properties of Zr-, Hf-, and Nb-doped REBCO thick films is presented to study the effect of the size, continuity, density, and shape of the BMO (M: Zr, Hf, and Nb) nanorods on the critical current of thick REBCO films over a wide range of magnetic fields and temperatures.

Chapter 4. The role of correlated pinning introduced by self-assembled nanorods

4.1. Introduction

Perovskite BMO_3 (B: Ba, M: Hf, Nb, Zr etc.) has been introduced into REBCO to enhance its flux pinning. BMO forms self-assembled nanorods along the c-axis of the REBCO film, thereby enhancing the critical current especially when a magnetic field is applied parallel to the c- axis. The efficiency of the BMO artificial pinning centers is directly related to their size, density, and continuity. Using the Advanced MOCVD system, it was possible, as mentioned in Chapter 3, to grow 4.8-μm thick Zr-doped REBCO films with continuous uninterrupted $BaZrO_3$ (BZO) and with a champion critical current I_c value of 8705 A/12 mm at 30 K and 3 T [74]. In this chapter, the pinning behavior of the high-performing REBCO conductors with BMO is examined. The pinning characteristics of films with different dopants, including Zr, Nb, and Hf, are compared and the contribution of the correlated pinning introduced by these dopants to the critical current are compared at temperatures from 4.2 K to 77 K and in magnetic fields up to 13 T. The effect of BMO density on the pinning characteristics in this range of temperatures and applied magnetic fields is also analyzed through investigation of REBCO films with different dopant concentrations.

4.2. Results and Discussion

4.2.1. Effect of Zr addition on critical currents in-magnetic field

Figure 4-1 illustrates cross-sectional and plan-view TEM images of two 4.7-μm thick (Gd,Y)BaCuO with 5% and 15% Zr addition. In both samples, growth of continuous-aligned BZO nanorods along the whole film thickness is shown in Figure 4-

1(a). A high density of RE_2O_3 precipitates that do not affect the growth of the BZO nanorods is also noted [74]. The plan-view microstructure of the 5% Zr-added film shown in Figure 4-1(d) reveals an average BZO diameter of 6.8 nm and an average spacing d = 22 nm. The matching field $B_\psi = \varphi_0/d^2$, where $\varphi_0 = 2.07 \times 10^{-15}$ Wb is the flux quantum, can be calculated as approximately 4.2 T. The 15% Zr-added sample reveals an average BZO diameter of 4.5 nm and an average spacing of 17 nm, resulting in a matching field B_ψ of approximately 6.9 T.

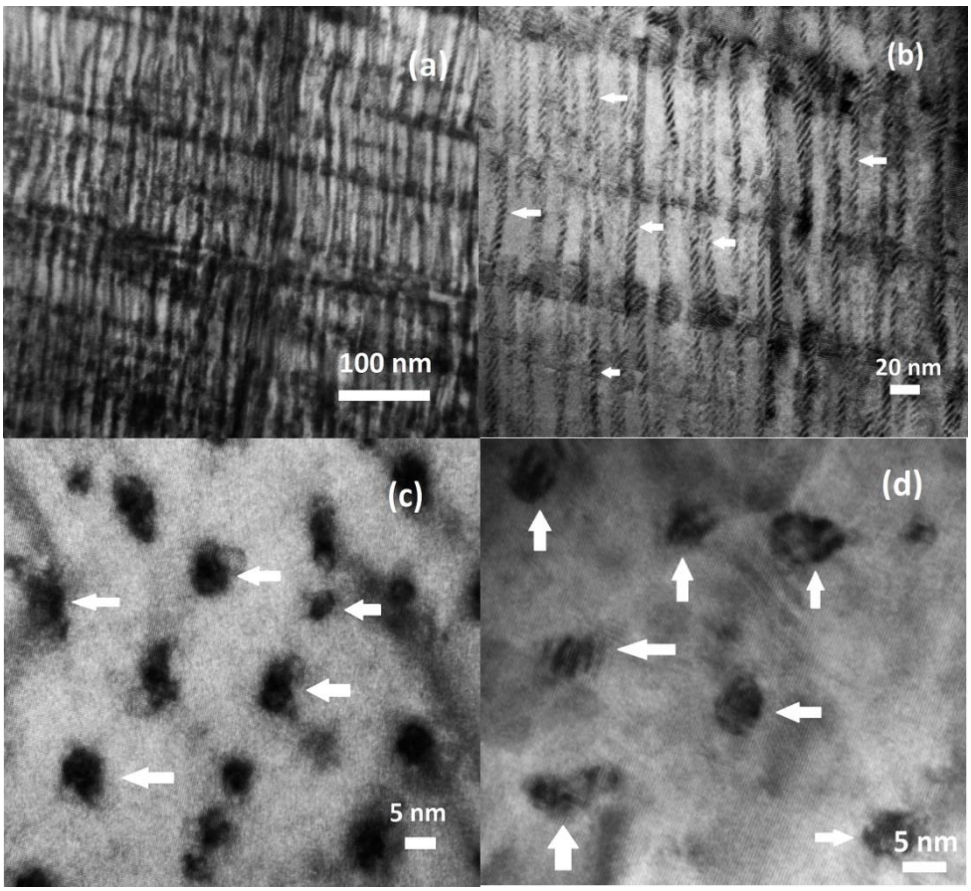

Figure 4-1. (a) and (b) TEM cross sections, representative of the entire 4.7-μm thickness of a 15 mol% Zr-doped REBCO sample (c) and (d) Plan-view TEM of 15 mol% and 5 mol% Zr samples. BZO is indicated by the arrows.

Table 4-1. Summary of microstructure features of two REBCO films with different Zr doping.

Zr mol. %	Thickness	Average BZO Spacing	Average BZO Size	Matching field Bψ
5%	4.7 µm	22 nm	6.8 nm (15 nm)	4.2 T
15%	4.7 µm	17 nm	4.5 nm (6 nm)	6.9 T

Note: The value in parenthesis in the average BZO size column represents the size of the largest diameter that was observed in both samples.

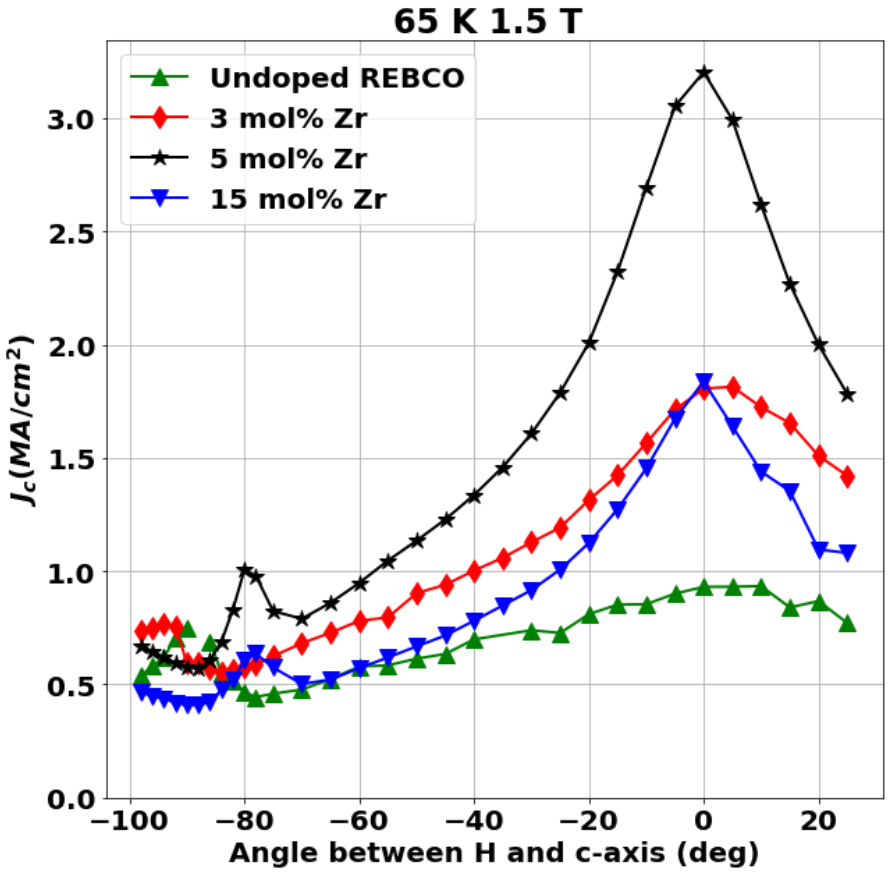

Figure 4-2. Angular dependence of critical current density J_c at 65 K and 1.5 T of an undoped REBCO film, and three Zr-doped REBCO films. All films were made by A-MOCVD and had a thickness of 4.5 to 4.7 µm.

Angular dependence of J_c at 65 K and 1.5 T is exhibited in Figure 4.2. Similar to the previous finding on heavily BZO-doped REBCO [85], we observed an increase in the J_c value in the c-axis direction at 65 K. While a 4.5-μm undoped REBCO film had a J_c of 0.93 MA/cm^2 at 65 K, 1.5 T (B||c), the J_c of a 4.7-μm 5% Zr-doped REBCO film reached 3.20 MA/cm^2 under the same conditions. The improvement in J_c along the c-axis depended on the dopant content. Both the 3% and 15% Zr doped REBCO films exhibit a J_c of about 1.8 MA/cm^2; the optimal performance at 65 K at 1.5 T is then achieved with 5% Zr doping.

Because of the critical current enhancement along the c-axis, the anisotropy ratio that is defined as Maximum J_c/ Minimum J_c reached 3.58, 5.53, and 4.5 for 3%, 5%, and 15% Zr doped samples, respectively, at 65 K and 1.5 T compared to 2.09 observed in the undoped REBCO film. Figure 4-2 also shows that the J_c of the pure REBCO sample at B||c is 1.25-times that of its J_c at B||ab.

Enhancing the pinning along the c-axis is correlated with the high density of BZO nanocolumns, as seen in the microstructure presented in Figure 4-1. These nanocolumns match the shape and dimensions of the flux vortices that are generated by the applied magnetic field, and thus, improve the pinning especially when the magnetic field is applied parallel to their growth direction, which is the c-axis of the REBCO film.

Angular dependence of J_c at 30 K and 3 T is illustrated in Figure 4-3. Similar to the previous findings on 15 mol% Zr-doped REBCO [85], a significant peak in J_c was observed in all three Zr-doped samples in the magnetic field orientation along the c-axis. This peak was lower than the peak in J_c that was observed when the field was

applied along the a–b orientation [86] with an anisotropy ratio (Maximum J_c/Minimum J_c) equal to 2, 1.60, and 1.46 for the 3%, 5%, and 15% Zr-doped samples, respectively. For the undoped REBCO film, the anisotropy was equal to 2.93. In contrast to 65 K, 1.5 T, where the enhancement in critical current resulting from the Zr doping led to a more anisotropic pinning, this enhancement led to more isotropic pinning at 30 K and 3 T. Additionally, the dependence of the critical improvement at 30 K on dopant content is different from that was observed at 65 K, with the 15% Zr-added GYBCO film exhibiting the highest critical current values in all field orientations.

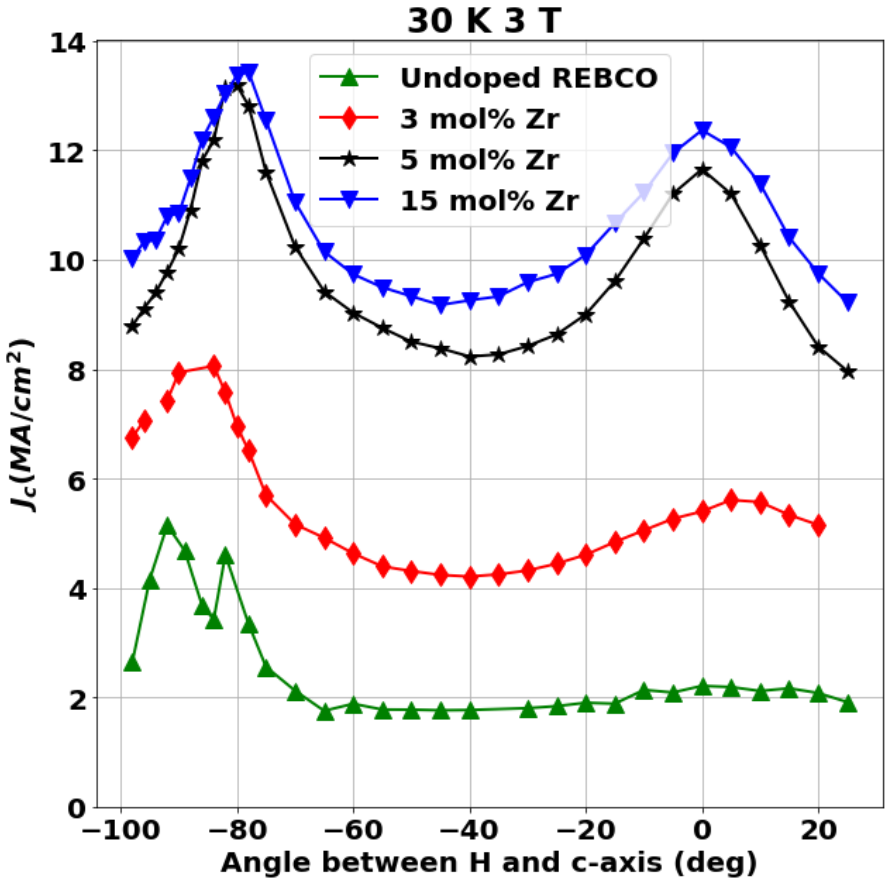

Figure 4-3. Angular dependence of critical current density J_c at 30 K and 3 T for an undoped REBCO film and three Zr-doped REBCO films. All films were made using A-MOCVD and have a thickness of 4.5 to 4.7 µm.

The enhancement in pinning in all directions at 30 K is attributed to the weak pinning defects that were introduced by the presence of BZO. The lattice mismatch between the BZO nanorods and the REBCO matrix generates a high density of point defects along the BZO/REBCO interface. These point defects act as pinning centers, especially in the weak pinning regime (below 40 K) [85]. These 1D pinning centers, because of their geometry, are effective in all magnetic field orientations, which explains the further enhancement of the minimum critical current with increasing Zr additions at 30 K and 3 T, as presented in Figure 4-3.

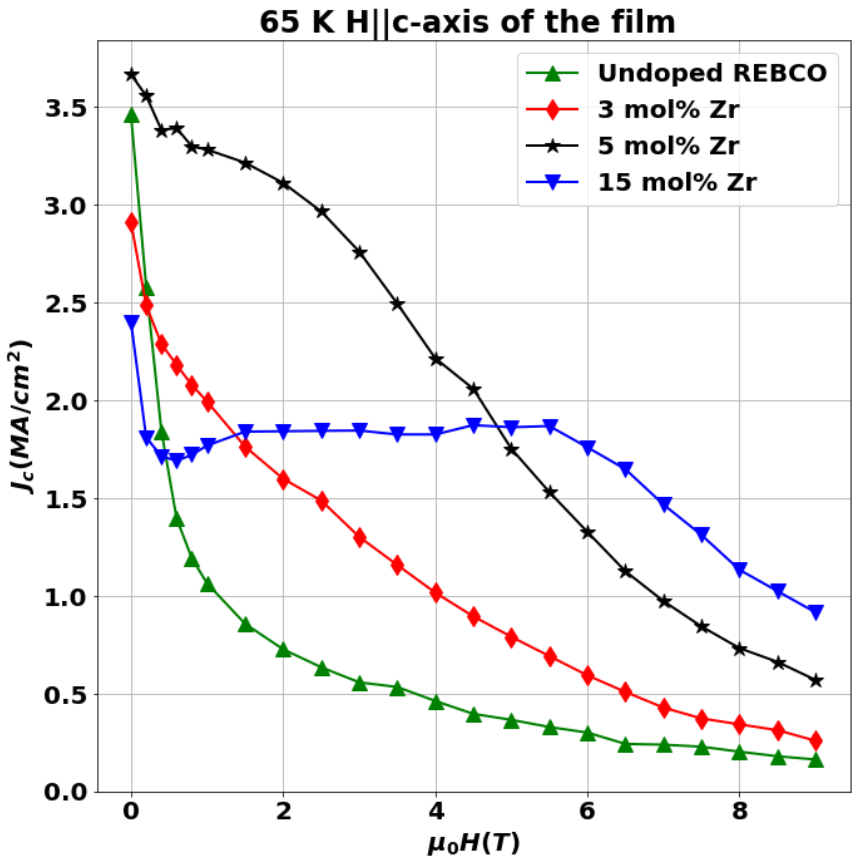

Figure 4-4. J_c (H||c-axis) at 65 K of 3 mol%, 5 mol%, and 15 mol% Zr-doped films in addition to a undoped REBCO film, all with 4.5 to 4.7-μm thick REBCO films.

Figure 4-4 demonstrates the field dependence of J_c(H||c) at 65 K in fields up to 9 T. The 15 mol% Zr-doped films were less sensitive to the field and exhibit a plateau

in J_c between approximately 0.2 and 6 T. Thus, an unusually high retention of 76% of the J_c self-field at 6 T was found. The 15 mol% Zr-doped sample showed a lower J_c than the 3 mol% and 5 mol% Zr-doped samples at low fields. The 5 mol% Zr sample had a self-field J_c of 3.6 MA/cm^2, while the 15 mol% Zr sample showed a 36% lower self-field J_c (2.3 MA/cm^2). However, the J_c of the 15 mol% Zr tape was the highest beyond 5 T because of the slower decay of its J_c. At 7 T, the value of J_c in the 15 mol% Zr sample reached 1.52 MA/cm^2, which was 54% higher than the J_c of the 5 mol% Zr sample.

Figure 4-5 displays the evolution of the pinning force $F_p = J_c \times H$ at 65 K in magnetic field up to 9 T. The 15 mol% Zr sample reached its maximum pinning force, 107 GN/m^3, at 7 T which almost equaled the 6.9 T matching field value that was predicted based on BZO spacing by TEM analysis. The 5 mol% Zr-doped sample attained its maximum pinning force, 92.7 GN/m^3, at 4.5 T, while the 3 mol% Zr-doped sample reached a maximum pinning force of 40.6 GN/m^3 at 3.5 T. The increase in the matching field and the maximum of pinning force with increasing Zr doping relates to the increasing nanorod density.

The plateau behavior where the J_c became less sensitive to the variation of the magnetic fields similar to that observed for the 15 mol% Zr sample was reported previously by Xu et al. [87] at 77 K when the Zr content is increased from 7.5 to 15 mol% in REBCO. This was also reported by Tsuchiya et al. [88] in SmBaCuO films at 65 K and 77.3 K when the $BaHfO_3$ volume content was increased from 2.2 to 4.5%.

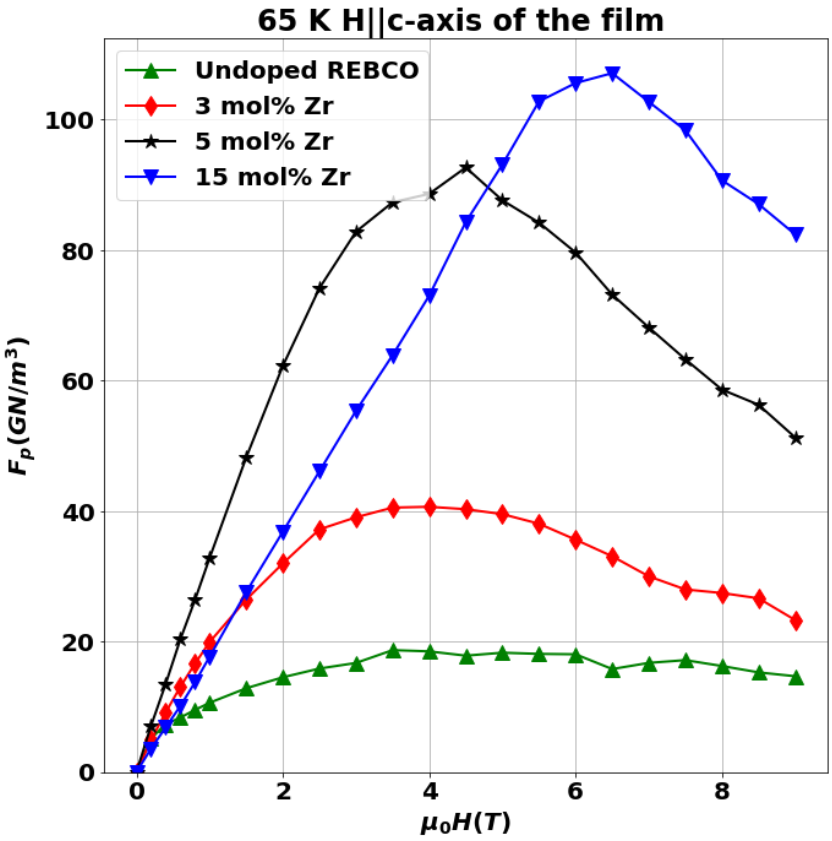

Figure 4-5. Pinning force density curves, $F_p = J_c \times \mu_0 H$ at 65 K, H|| c-axis of 3 mol%, 5 mol%, and 15 mol% Zr-doped tapes in addition to a undoped REBCO film, all with 4.5 to 4.7-µm thick REBCO films.

In Figure 4-6, the field dependence of J_c up to 9 T at different angles up to 15º from the c-axis of a 15 mol% Zr-doped 4.7-µm thick film is presented. This sample also exhibited a plateau in J_c below 6.5 T. It is seen that the plateau gradually contracts with declining J_c values at all fields as the applied magnetic field is moved away from the c-axis. This behavior can be an outcome of the truncation of every vortex that is actually pinned by the nanorods when the angle between the applied magnetic field and the BZO nanorods increases. As shown in Figure 4-6 (b), the pinning force curve exhibited a pronounced peak only when the magnetic field was applied along the c-axis.

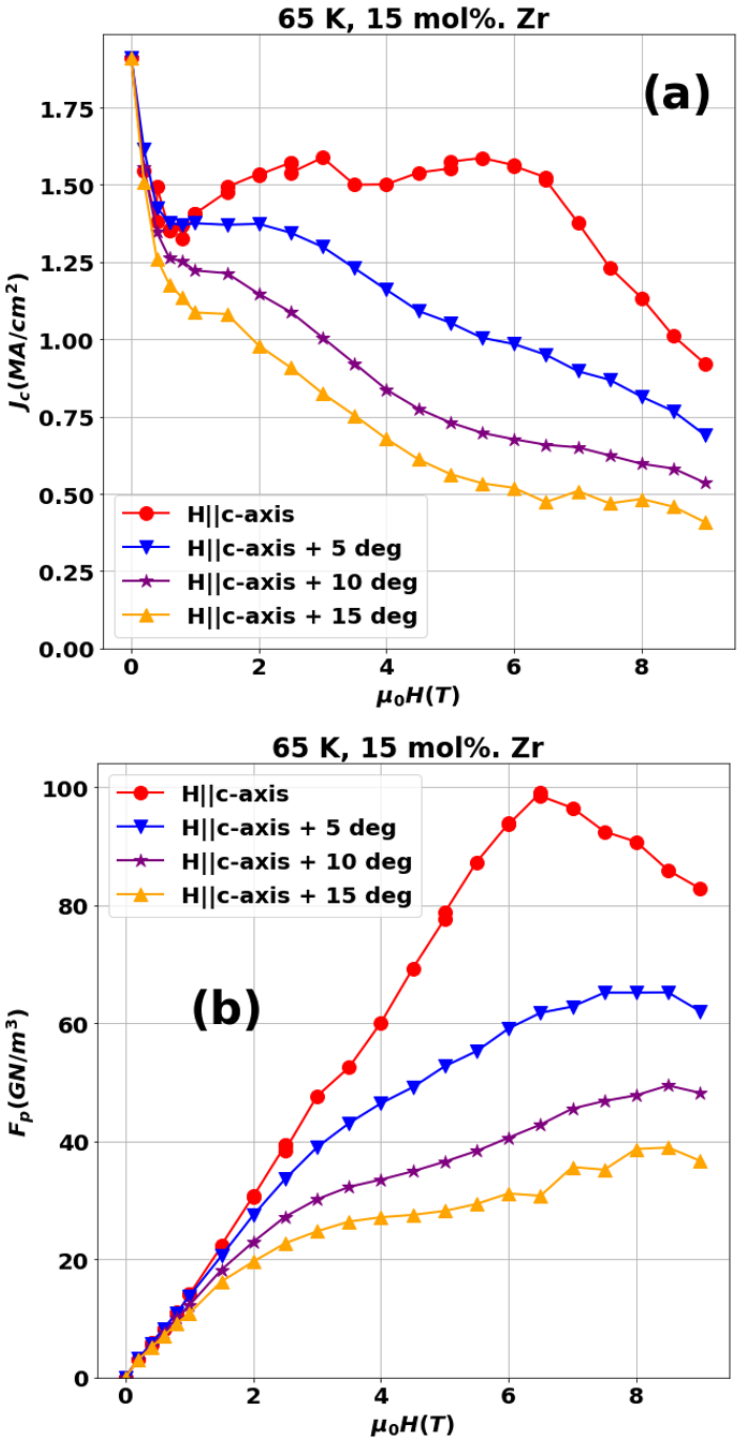

Figure 4-6. (a) $J_c(H)$ at 65 K in field orientations in five-degree increments from the c-axis. An extended J_c plateau is seen only at the H||c-axis. (b). Corresponding pinning force characteristics at 65 K

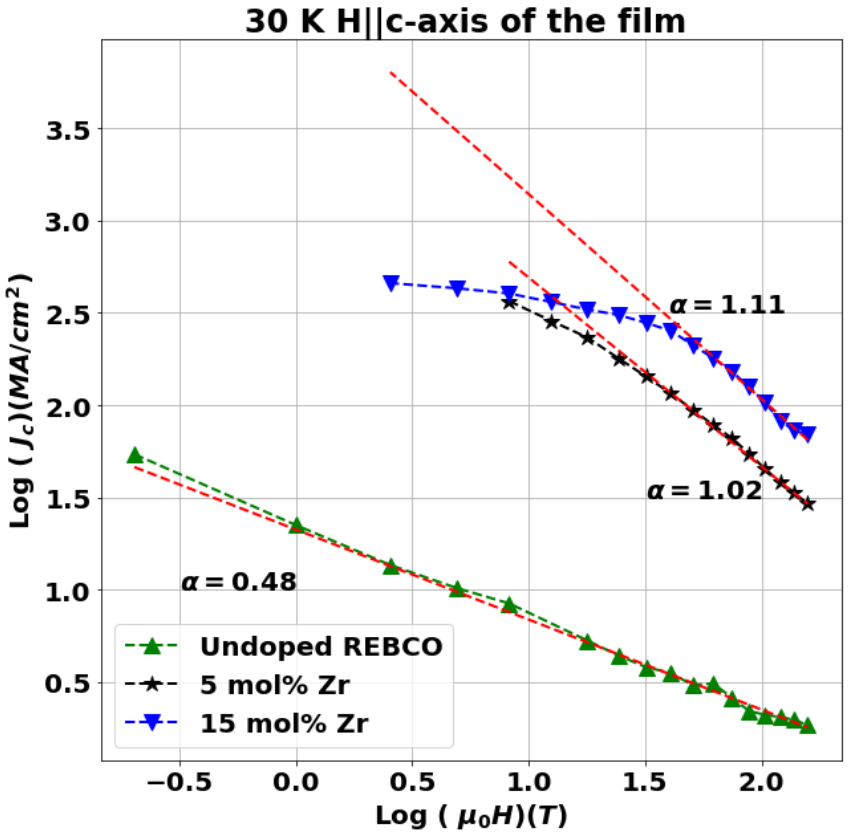

Figure 4-7. J_c (H||c-axis) at 30 K of undoped REBCO, and 5% Zr-doped and 15% Zr-doped tapes, all with 4.7-μm thick films. The J_c values of the 5% and 15% Zr-doped tapes are proportional to $H^{-\alpha}$ above their accommodation fields.

Figure 4-7 shows the J_c (H||c-axis) at 30 K of the undoped REBCO and the 5% and 15% Zr samples. We noticed that both the Zr-doped films followed the power law function $J_c \sim H^{-\alpha}$, at magnetic fields higher than their respective accommodation fields, where α = 1.02 for the 5% Zr sample and 1.11 for the 15% Zr sample. We noticed the highest accommodation field in the 15% Zr sample i.e., the faster decline in critical current occurred at a higher applied magnetic field in sample. The J_c of the undoped REBCO film, however, has an α = 0.48 and followed the power law from the first tested magnetic field, 0.2 T. The maximum pinning force of the 15% Zr sample reached 621 GN/m^3 at 6 T.

Further information on the temperature dependence of the pinning mechanisms can be obtained by fitting the field dependence of J_c using the collective pinning model that is presented in Chapter 1. To separate the contribution of the random uncorrelated defects from the correlated defects to pinning when the magnetic field is applied along the c-axis of a REBCO film with BZO nanorods, the J_c uncorrelated can be fitted using Equation 1-7. For this work, because we are fitting J_c (H||c), $\varepsilon(\theta) = \varepsilon(0) = 1$, H_0 is the accommodation field, H_{irr} is the irreversible field and p and q are two dimensionless parameters. For REBCO films in the collective pinning regime, p and q are in the range of 0.5 to 0.6 and 2 to 3, respectively [54]. The irreversibility field H_{irr} was approximated using the following equation.

$$H_{irr}(T) = H_{irr}(0)\left(\frac{\mathrm{T}}{\mathrm{T_c}}\right)^{-\mathrm{a}}\left(1-\frac{T}{T_c}\right)^{b}, \qquad \text{Equation (4-1)}$$

where H_{irr} (0) =120 T, and a and b are equal to 0.015 and 1.42, respectively [89-91]. Magnetic critical current of the 5 mol% and 15 mol% Zr-doped films was fitted using the model because of the data availability at more temperatures from 4.2 K to 77 K and at higher magnetic fields up 13 T (Figure 4-8).

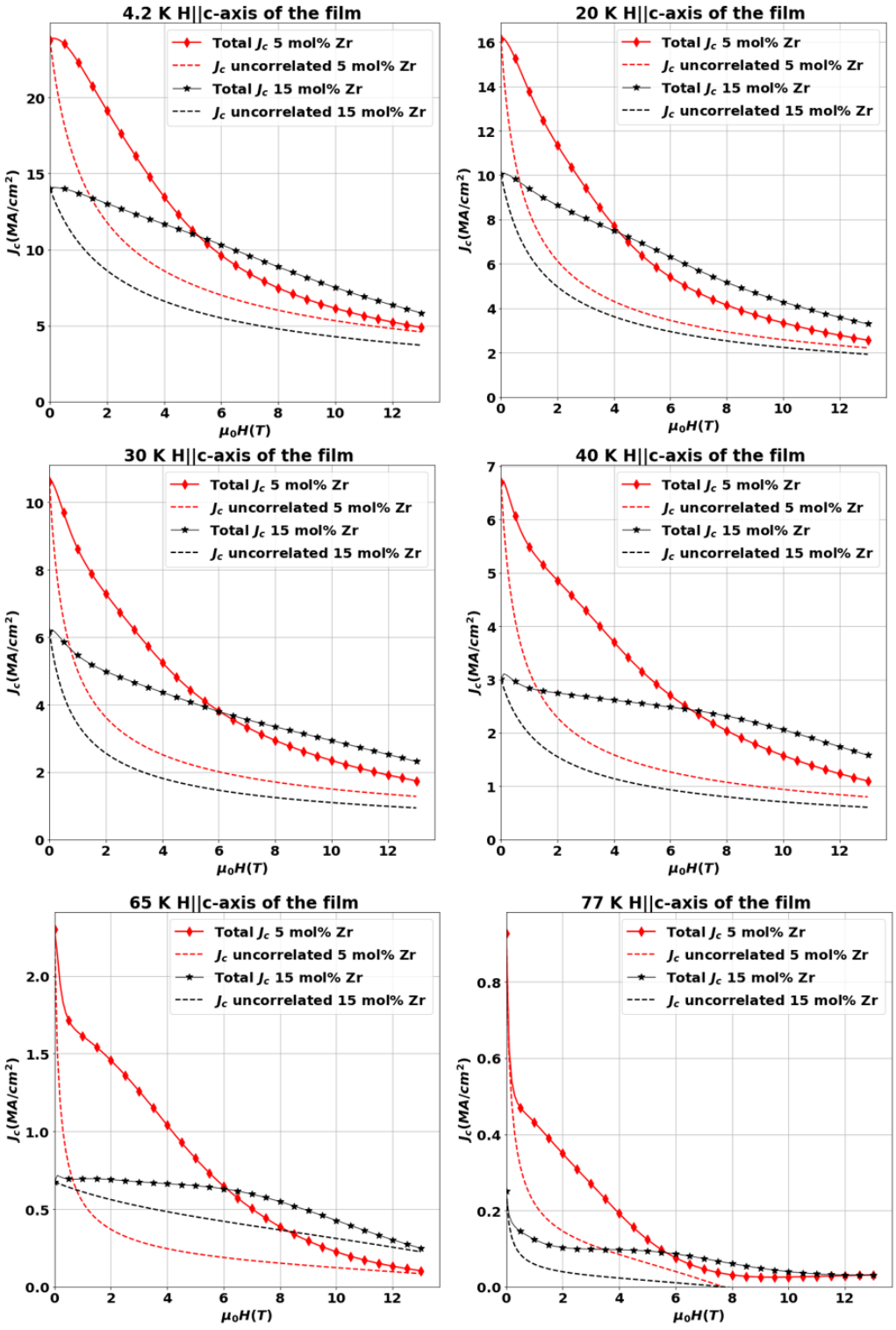

Figure 4-8. Field dependence of the total magnetic J_c of 5 mol% and 15 mol% Zr samples at temperatures from 4.2 to 77 K compared to their J_c from uncorrelated random pinning centers.

Figure 4-8 presents field dependence of the magnetic critical current density of the 5 mol% and the 15 mol% Zr-doped samples at temperatures from 77 K to 4.2 K. The 15 mol% Zr sample shows higher critical current density values over the whole range of magnetic fields at temperatures below 30 K; this is the weak pinning regime. At temperatures greater than 30 K, the 5 mol% Zr sample shows higher critical current density at the lower fields, while the 15 mol% Zr sample is less sensitive to the field. The same figure shows the fitting of J_c from uncorrelated pinning; its contribution to the total J_c was observed to increase with decreasing temperatures. In the strong pinning regime, the difference between the total critical current density and the uncorrelated pinning critical current density decreased with increasing applied magnetic field.

Figure 4-9 shows the percentage of contribution of the correlated pinning to the total critical current density of 5 mol% and 15 mol% Zr-doped samples from 4.2 K to 65 K. We observed that the correlated pinning contributed to more than 60% of the total critical current over the whole range of magnetic fields at 65 K for the 15% Zr sample, which confirmed the direct relationship between the BZO pinning and the presence of the plateau that was observed at 65 K in the 15 mol% Zr-sample. This contribution reached its maximum at 6 T. This maximum was achieved at a lower magnetic field of approximately 2.5 T for the 5 mol% Zr sample. The correlated pinning contribution decreased with decreasing temperature and at 4.2 K, the maximum contribution of the correlated pinning was below 50% for both samples. The correlated pinning critical current density increased with increasing Zr doping in both the weak and the strong pinning regimes.

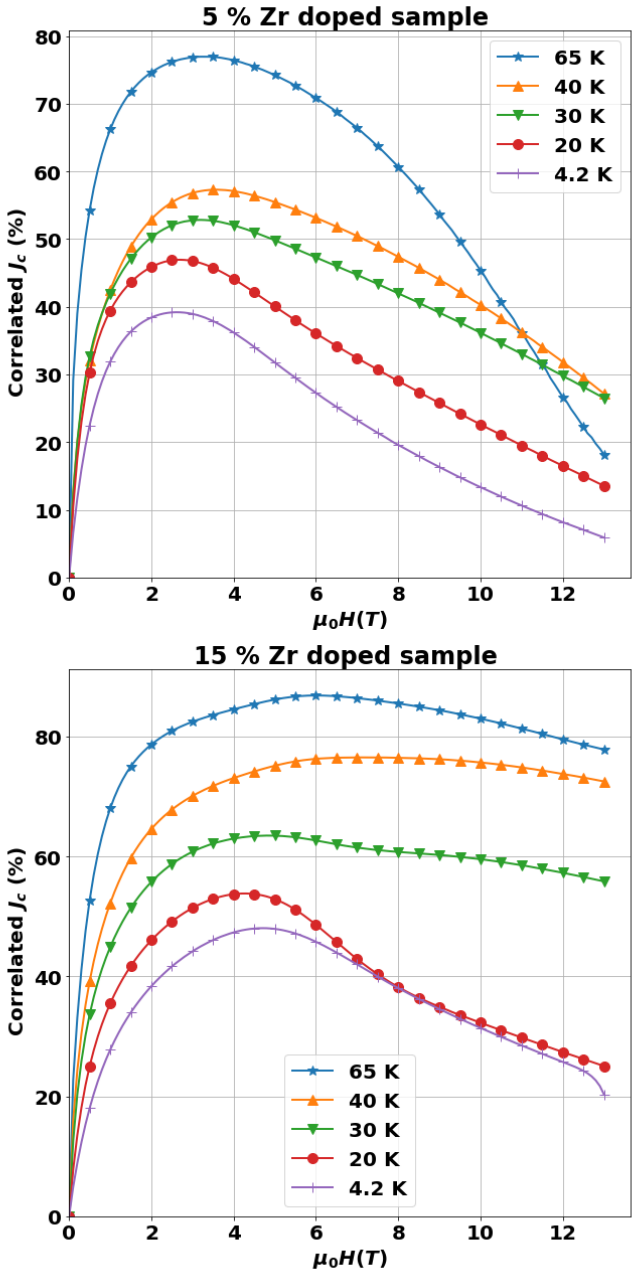

Figure 4-9. Contribution of the correlated pinning centers to the total critical current density of 5 mol% and 15 mol% Zr samples from 4.2 K to 65 K.

The magnetic field dependence of the critical current of 4.5 to 4.7 µm REBCO samples with different Zr doping up to 15 mol% showed that although the 5 mol% Zr-added tapes performed better at 65 K and low magnetic fields (below 5 T), increasing

the BZO density in 15% Zr resulted in higher critical currents at 65 K in higher magnetic fields, and also at temperatures below 30 K over the entire range of the magnetic fields (up to 13 T). Next, the performance of REBCO tapes with different perovskite oxide BMOs, including $BaNbO_3$, $BaZrO_3$, and $BaHfO_3$ is compared over a wide range of temperatures and applied magnetic fields.

4.2.2. Comparison among Zr, Nb, and Hf additions

Figure 4-10 illustrates cross-sectional TEM images of three (Gd,Y)BaCuO films. The first film (Figure 4-10 (a)) is 5 mol% Zr doped, the second film is 5 mol% Hf doped (Figure 4-10 (b)), and the third film is 5 mol% Nb doped (Figure 4-10 (c)). Both the Zr- and Hf-doped samples show the presence of narrow nanorods over the whole thickness of the films, and most of the nanorods are 3.5 to 5 nm wide. It is observed that while the RE_2O_3 did not break the BZO nanorods, the BHO nanorods were shorter and their growth was usually interrupted by the RE_2O_3 precipitates. BNO observed in the third sample formed shorter nanorods, more like round precipitates that are elongated along the c-direction of the film. In addition to the larger size of the BNO spherical precipitates, high strain regions were observed at the boundaries between them and the REBCO matrix.

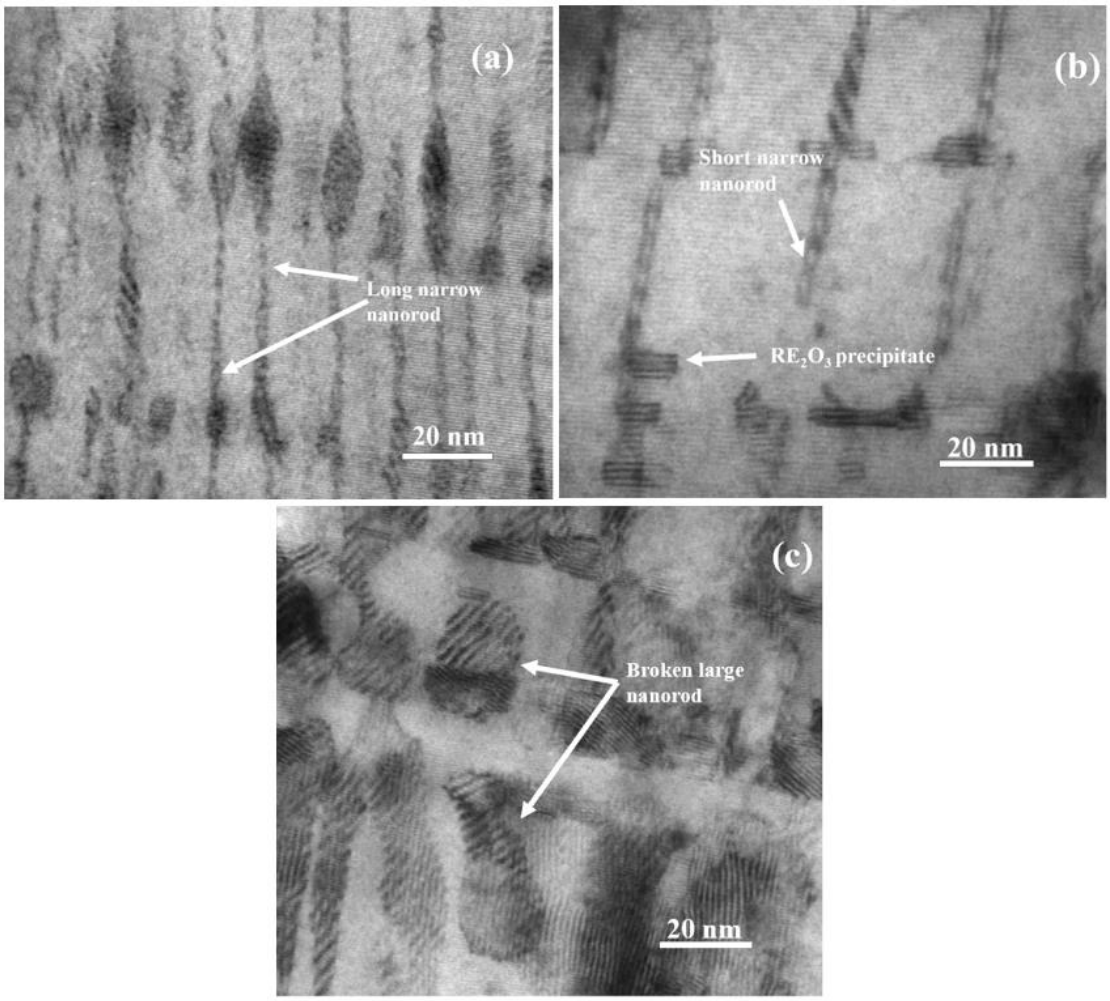

Figure 4-10. (a) 250,000× TEM cross-section of a 5 mol% Zr-added sample. (b) 400,000× TEM cross-section of a 5 mol% Hf-added sample. (c) 400,000× TEM cross-section of a 5 mol% Nb-added sample.

Figure 4-11 shows the angular dependence of the critical current density at 65 K, 1.5 T of 5 mol% Zr, Hf, and Nb-doped samples in addition to an undoped REBCO film. It is observed that all three-doped samples show a dominant J_c peak at B|| c-axis compared to the undoped REBCO sample. It is also observed that the Hf and Zr samples show a much higher J_c at B|| c-axis than the Nb-doped sample. This observation can be explained by the microstructure of the Nb sample which contains large and short nanorods which are likely not as efficient pinning centers as the narrow and long

nanorods. It is also observed that the Hf-doped sample show a much higher minimum J_c than the other samples. This result may be explained by the formation of narrow discontinuous nanorods that make their density higher without degrading the REBCO, which could improve both the self-field and the minimum J_c. A similar result was reported by several groups that observed a more isotropic pinning behavior in Hf-doped REBCO [25, 81, 92, 93]. As a direct consequence, the anisotropy for the 5 mol% Hf-doped sample was equal to 2.64, which was the lowest between all three doped samples; it was equal to 5.53 for the Zr-doped sample and 2.89 for the Nb-doped sample.

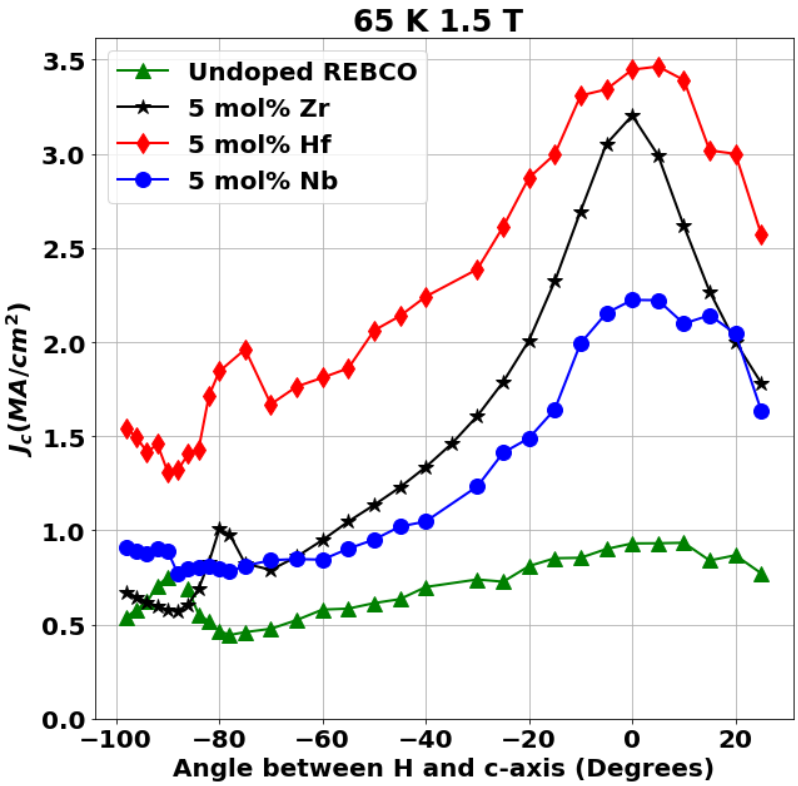

Figure 4-11. Angular dependence of the critical current density J_c at 65 K and 1.5 T for a pure REBCO film and three REBCO films doped with 5% Zr, Hf, and Nb.

The Nb and Hf-doped samples had comparable anisotropy, but the Hf-doped sample had much higher critical current density at all magnetic field orientations. The performance of the Hf-doped sample is much more attractive.

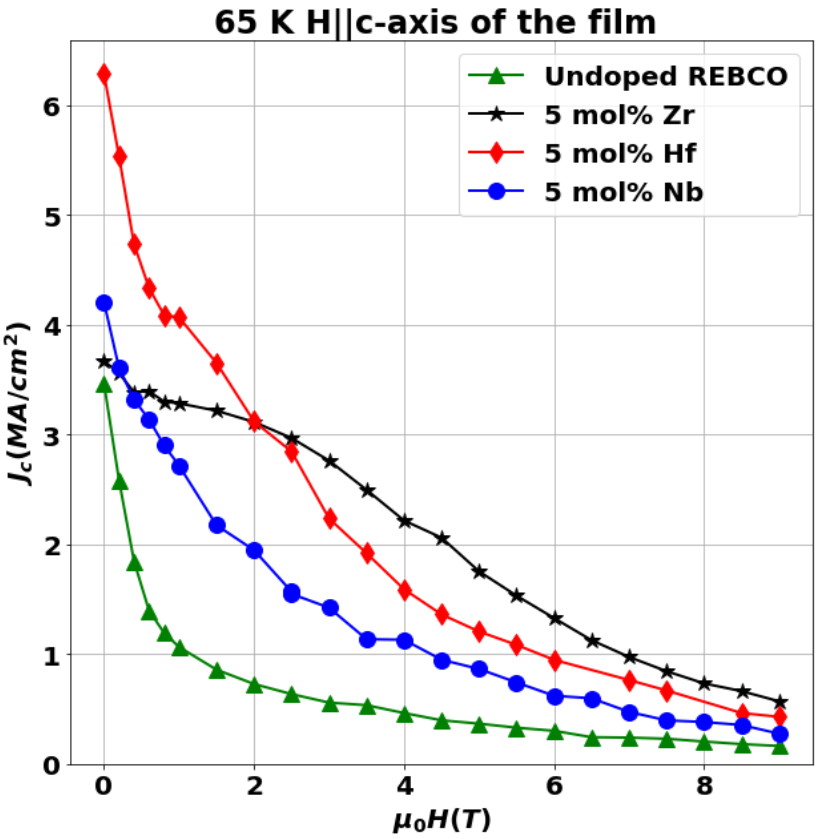

Figure 4-12. J_c (H||c-axis) at 65 K of 5 mol% Zr, Nb, and Hf-doped tapes in addition to an undoped REBCO film.

Field dependence of a critical current density at 65 K up to 9 T is shown in Figure 4-12. The higher self-field value for the Hf-doped sample is evident. The field dependence curve of the Zr-doped sample crossed the Hf-doped sample's curve at 2 T, so the J_c of the Zr-doped sample is the highest at higher magnetic fields. This can be explained by its microstructure which consists of a high density of long and aligned BZO nanorods along the whole thickness of the film. This microstructure results in a

matrix of pinning centers that prevents the movement of the flux vortices even with increasing applied Lorentz force that can make the Zr-doped sample more resistant to flux creep. This observation was confirmed by the pinning force curve at 65 K (Figure 4-13), where the Zr-doped sample shows the highest maximum pinning force and the highest matching field among all samples. Its matching field was 4.5 T compared to 2.5 T of the Hf-doped sample. The maximum pinning force of the 5 mol% Zr-doped sample was equal to 9.26 GN/m^3 compared to 7.10 GN/m^3 of the Hf-doped sample and 4.51 GN/m^3 of the Nb-doped sample.

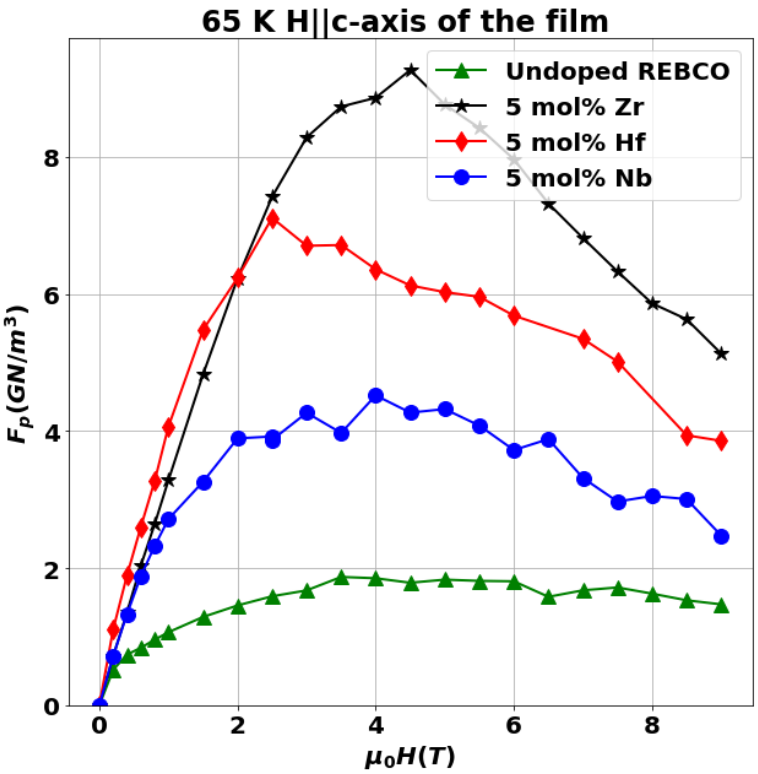

Figure 4-13. F_p (H||c-axis) at 65 K of 5 mol% Zr, Nb, and Hf-doped films in addition to an undoped REBCO film.

At 30 K, with the magnetic field applied parallel to c-axis of the film (Figure 4-14), the 5% Zr-doped sample showed double the critical current density of the 5% Hf-doped sample at all applied magnetic fields. At 3 T, while the J_c of the 5% Zr-doped

sample was equal to 11 MA/cm^2, which corresponds to a lift factor in the critical current of 7.88, the J_c of the 5% Hf-doped sample was equal to 6.14 MA/cm^2 at the same magnetic field and temperature which corresponds to a lift factor of 2.54 in the critical current density.

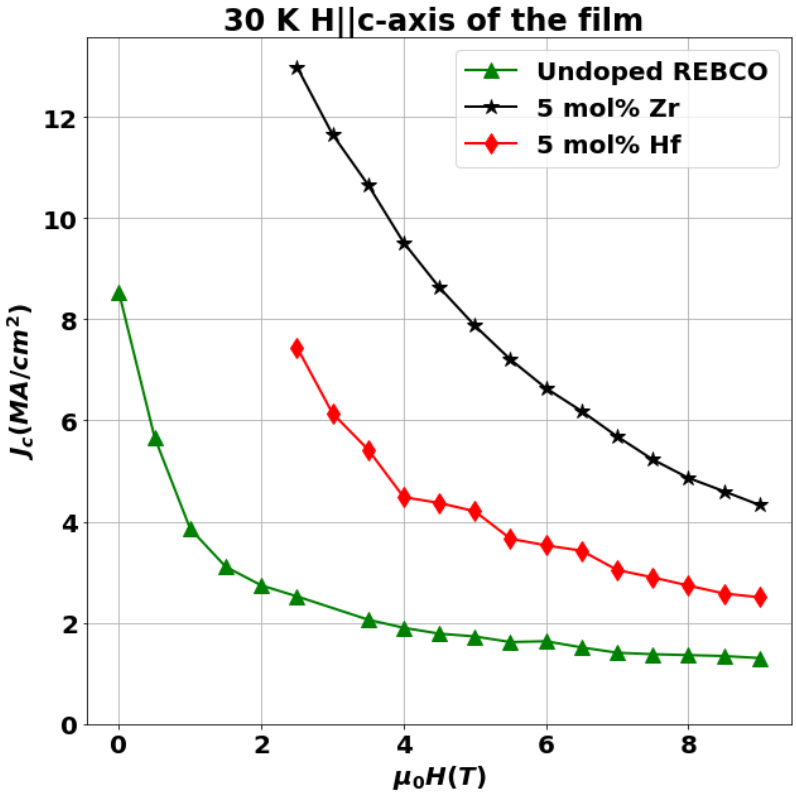

Figure 4-14. J_c (H||c-axis) at 30 K of 5 mol% Zr and Hf-doped films in addition to a pure REBCO film.

The contribution of the correlated pinning mainly by BZO, BNO, and BHO to the magnetic critical current density of the three samples at different temperatures is shown in Figure 4-15. The short and discontinuous nanorods present in the Hf and Nb-doped samples appear to be effective mainly at lower magnetic fields at all temperatures when compared to the long BZO nanorods that were present in the Zr-doped sample that appear to be effective at higher fields as well. This observation was confirmed by

the higher retention of self-field critical current in the Zr-doped samples with increasing magnetic field. The contribution of correlated pinning to the total critical current was also lower in Hf- and Nb-doped samples which contain short nanorods. The higher critical current that was observed in the Hf-doped sample at 65 K below 2 T was a result of the higher self-field of the sample. The contribution of correlated J_c introduced by the continuous BZO nanorods was observed to decrease steadily with temperature while the contribution of the correlated J_c introduced by the BHO short columns collapsed to the same curve below 40 K. The correlated J_c of samples with BNO had different characteristics at different temperatures which may be due to the more complex pinning landscape introduced by the BNO precipitates, Figure 4-10. The contribution of correlated J_c introduced by the continuous BZO nanorods had a consistent trend of peaking at lower magnetic fields with decreasing temperature whereas the peaks in the contribution of the correlated J_c introduced by the BNO and BHO do not show any trend with varying temperature.

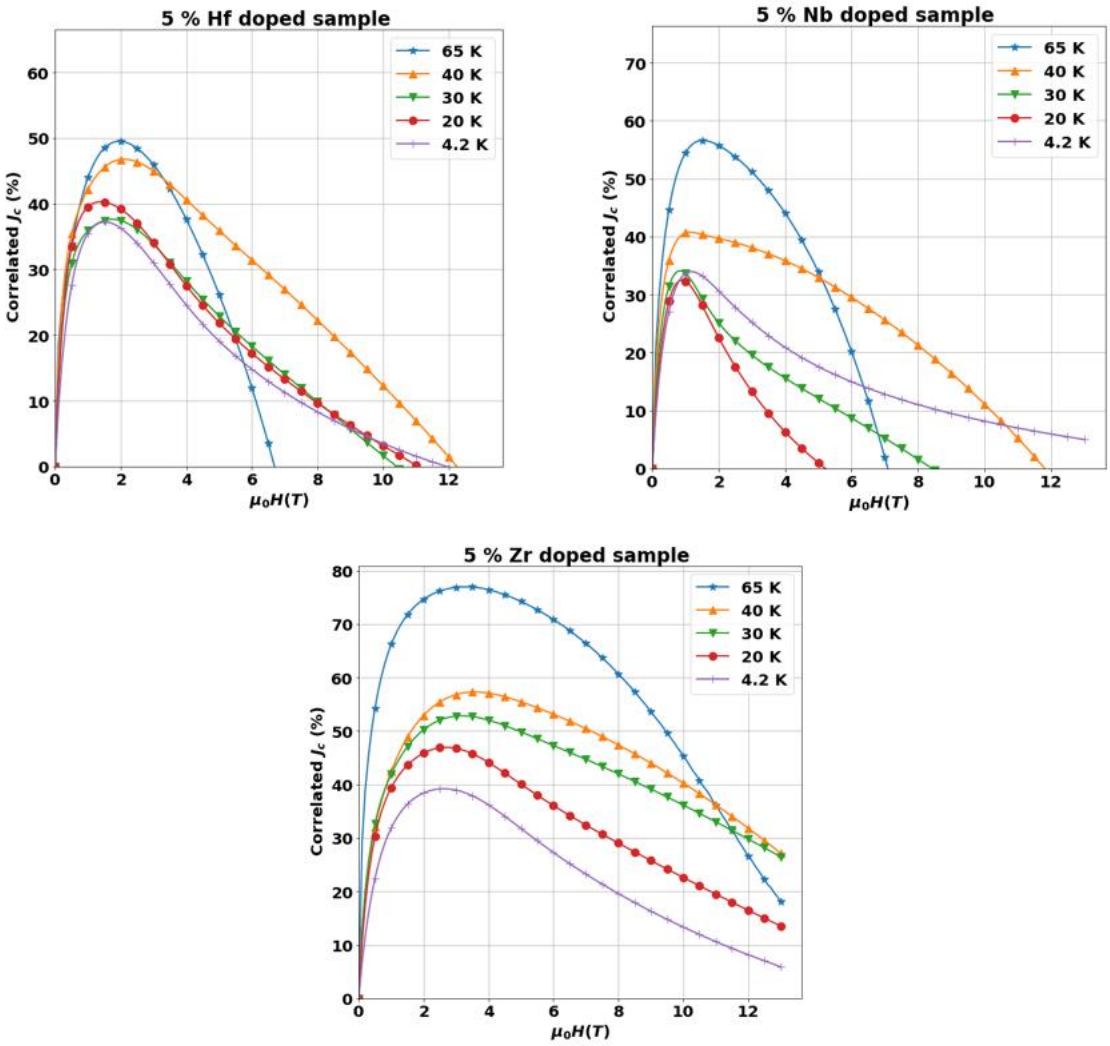

Figure 4-15. Contribution of correlated pinning centers to the total critical current of 5 mol% Hf, Nb, and Zr-doped samples from 4.2 K to 65 K.

REBCO tape with 15 mol% Hf was tested in the National High Magnetic Field at 4.2 K and magnetic fields up to 31.2 T. The barium concentration in the precursor was varied from 1.97 to 2.10 for the 15 mol% Hf-doped sample to optimize the BHO density for 4.2 K performance. Figure 4-16 (a) shows the J_c plot for three 15% Hf-doped samples with different barium concentrations in addition to a 5% Hf-doped sample. The film thickness of these samples ranged from about 3.7 to 4.4 μm. While all 15% Hf-

doped samples were expected to show a higher critical current then the 5% Hf sample, no significant difference was observed between the samples with 15% Hf doping despite the Ba variation as seen in Figure 4-16 (a). The samples with the highest and lowest Ba concentrations showed almost the same J_c values at all magnetic field conditions. Fitting the critical current to the power-law function gave an alpha value in the range of 0.92 to 0.94 for the 15% Hf-doped samples and an alpha value equal to 0.67 for the 5% Hf-doped sample. The corresponding pinning force curve is reported in Figure 4-16 (b), where it is seen that the pinning force of the 5% Hf-doped sample increases up to 24 T, while the pinning force of all the 15% Hf-doped samples showed a mild increase after 10 T. This result is unlike 65 K data where the pinning force reached a maximum at a much lower magnetic field before starting to decline. The 15% Hf-doped sample made with 1.97 Ba in the precursor showed a maximum pinning force of 1.34 TN/m^3 at 30 T.

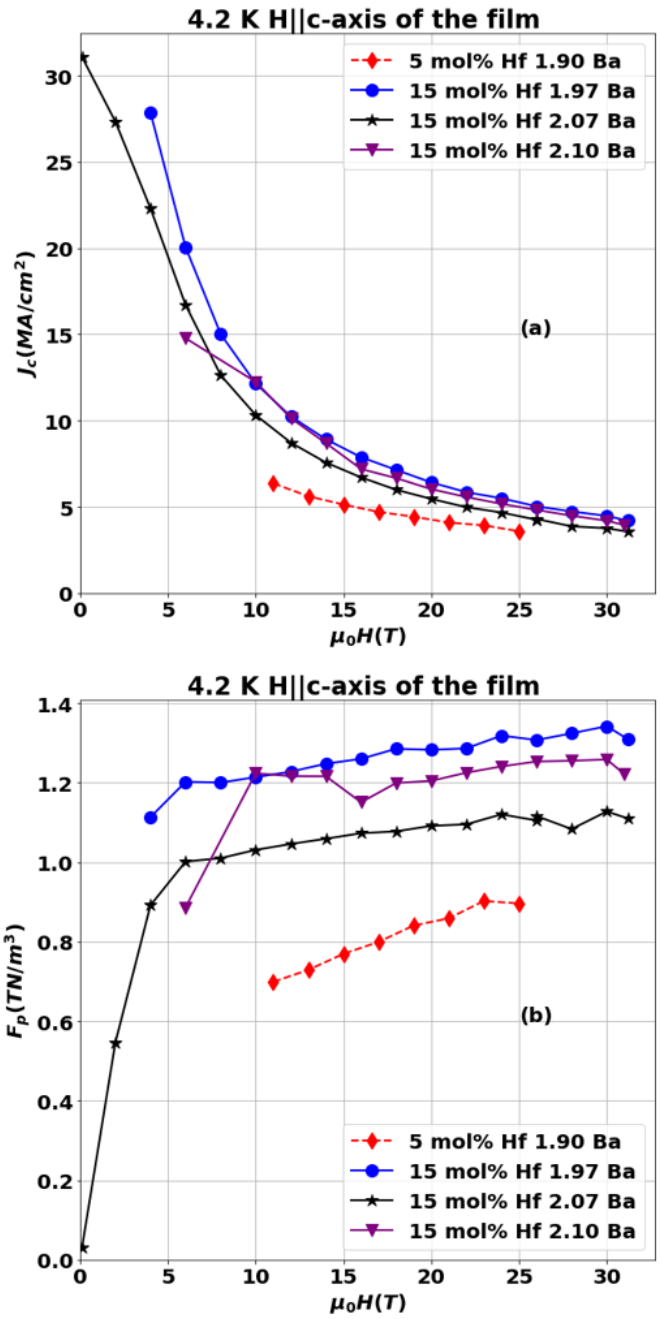

Figure 4-16. (a) Critical density at 4.2 K and magnetic fields up to 31.2 T of REBCO films with 5% Hf and 15% Hf doping with Ba in precursor variations. (b) The corresponding pinning force curves.

A log–log plot of the field dependence of J_c can be divided into two regimes. In the lower field regime, a plateau is observed in the critical current density. In the higher-field regime, the field-dependence of the critical current follows a power-law. The J_c in

the first regime can be enhanced by increasing the critical current self-field, which raises the whole field dependence curve. Increasing the extent of the plateau (delaying the start in decay of J_c) can be achieved by incorporating BMO into REBCO as observed at 30 K in Figure 4-7. However, the reduction of the alpha value means that a slower decay rate is achieved in the power-law regime. The temperature dependence of the alpha value of J_c of the BMO samples that have been discussed in this chapter is presented in Figure 4-17. The alpha value was fitted from the magnetic J_c curves at temperatures from 4.2 K to 65 K and magnetic fields up to 13 T. A decay in the alpha value with decreasing temperature is observed in all the doped samples. Among the 5 mol% Zr-, Nb-, and Hf-doped samples, the Zr-doped sample that had continuous small-diameter nanorods showed that the lowest alpha value at 65 K , while the highest alpha value was seen in the Nb-doped that sample that had large precipitates. A greater reduction in the alpha value at 65 K was achieved by increasing the density of BMOs, as observed for the 15 mol% Zr- and Hf-doped samples. Below 40 K, in the weak pinning regime, the 15 mol% Zr- and Hf-doped samples maintained an almost constant alpha value of around 1, while the lower dopant samples had a decreasing alpha value that reached 0.7 for the 5% Nb-doped sample at 4.2 K. However, while the low dopant concentration sample exhibited a slightly lower alpha value at 4.2 K, it had a lower accommodation field. This means that the decay in critical current density starts at a lower magnetic field, which makes the performance of the higher dopant concentration samples more interesting at 4.2 K.

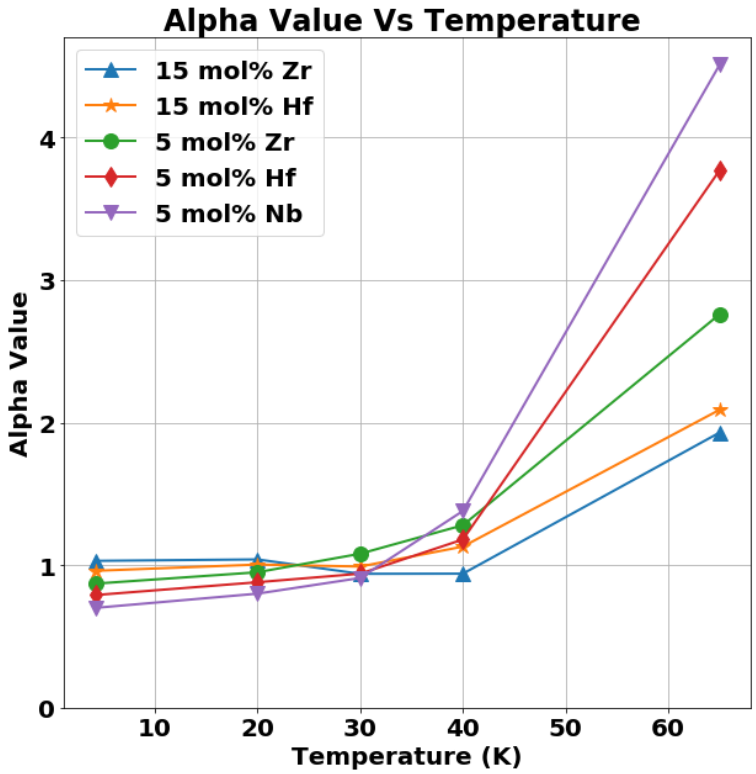

Figure 4-17. Evolution of the alpha value vs temperature for samples with different dopants and different dopant concentrations

4.3. Conclusions

A detailed J_c (H, T) study is presented on 4 – 5 µm thick film REBCO samples with different BMO doping (M: Zr, Hf, and Nb) and with different doping concentrations (3 to 15 mol%) to investigate the effect of the density, size, and continuity of the BMO on J_c. By fitting the contribution of uncorrelated pinning to the total J_c, it is demonstrated that the correlated pinning induced by the incorporation of BMO dominate the critical current in the strong pinning regime. While samples with small in diameter discontinuous BMO exhibit a higher J_c at 65 K and low magnetic fields, samples with continuous BMO of a small diameter show a higher field-independent J_c, resulting in higher critical currents in the higher magnetic field regime.

The 5% Hf-doped sample showed a more isotropic angular dependence of the critical current with a slightly higher critical density along the c-axis at 65 K and 1.5 T, while the 5% Zr-doped sample performed better at higher magnetic fields and at lower temperatures. Increasing the Zr and Hf doping to 15% led to a better performance in high magnetic fields and at low temperatures. From TEM observations and correlated pinning fittings, it appears that a higher density of continuous nanorods helps to achieve higher pinning forces and matching fields by building a stronger pinning matrix and making the REBCO more resistant to magnetic flux creep. This would explain the higher critical current values at higher magnetic fields that were observed in the higher dopant samples and in the samples where continuous nanorods where observed in TEM. This would also explain why 15 mol% Zr-doped samples showed a magnetic field-independent critical current up to 6 T at 65 K.

While the incorporation of BMOs into REBCO led to an improvement of the c-axis critical current, it also increased the anisotropy of these samples at 65 K. In the next chapter, several methods are presented to improve the pinning in the a–b-direction and the minimum critical current in Zr-doped REBCO.

Chapter 5. Toward isotropic pinning in BZO doped REBCO

5.1. Introduction

Due to its anisotropic crystal structure in addition to the anisotropic effectiveness of the different pinning centers, REBCO has an anisotropic critical current in a magnetic field. BZO addition to REBCO leads, as reported in the previous chapter, to an enhancement of the critical current when a magnetic field is applied parallel to the c-axis of the film and a greater anisotropy in in-field critical current, especially at high temperatures [38, 94]. The pinning landscape in Zr-doped REBCO can be engineered and made richer by the incorporation of additional pinning centers such as RE_2O_3 that are effective in magnetic field orientations aside from the c-axis of the REBCO film.

RE_2O_3 nanoprecipitates are formed by deviation from the REBCO 1:2:3 stoichiometry and are effective pinning centers, especially when the magnetic field is applied parallel to the ab-plane of the REBCO film[35, 40, 68, 95-97]. Using A-MOCVD, films with a high density of these precipitates were grown without intercepting the growth of the BZO nanorods, resulting in enhancing the J_c (B||ab-plane) at 65 K, 1.5 T.

A second approach to reducing the anisotropy of the Zr-doped REBCO is a multilayered architecture made of successive layers of undoped REBCO and Zr-doped REBCO. The angular dependence of critical current value at 65 K, 1.5 T of tapes of this multilayered architecture is compared with that of an undoped REBCO film and Zr-doped film of similar thickness.

A novel post-deposition method to improve the ab-plane pinning is then presented, where fully-processed Zr-doped REBCO films were subject to high-temperature tensile-creep deformation. The deformation process resulted in increased density of ab-plane stacking faults, which can enhance the critical current, especially when the magnetic field is applied parallel to the ab-plane of the REBCO film. In fact, their effect has been confirmed by the dramatic drop in the I_c (B || ab) at 77 K, 1 T when they were eliminated by high-temperature annealing [98] and by the increase in I_c in this field orientation through the optimization of their density in Sm-doped REBCO [99]. High-temperature compressive deformation has been demonstrated with bulk melt-textured YBCO, where an increase in dislocation density has been observed to yield enhanced in-field critical current over a wide range of field orientations [42]. However, high-temperature deformation has not been shown to be a viable method for REBCO tapes. Even though REBCO tapes are processed with a tensile force in reel-to-reel fabrication, the impact of tensile forces at a high temperature after processing has not been investigated until this work. Finally, the anisotropy of critical current of a round wire made by winding Zr- doped REBCO tapes on a round copper former is presented.

5.2. Results and discussion

5.2.1. Effect of the rare-earth oxide density on the electromagnetic properties of REBCO

While Zr-doping of GdYBCO led to an enhancement of pinning along the c-axis, the anisotropy of critical current density increased at 65 K, 1.5 T. Figure 5-1 shows the evolution of the retention of the 65 K self-field I_c up to 9 T when the magnetic field was applied at different orientations to a 5 mol% Zr-doped GdYBCO film. It is seen

that while the c-axis pinning (dominated by BZO) enabled retention of more than 50% of the self-field I_c up to 5 T, the I_c retention in the orientation of B||ab was below 50% of self-field I_c, starting from 0.6 T. The minimum I_c direction is the angle at which the sample had the lowest critical current value (direction at which the pinning mechanisms are the least efficient). When the magnetic field was applied parallel to this direction, the retention factor was below 40% at 0.4 T.

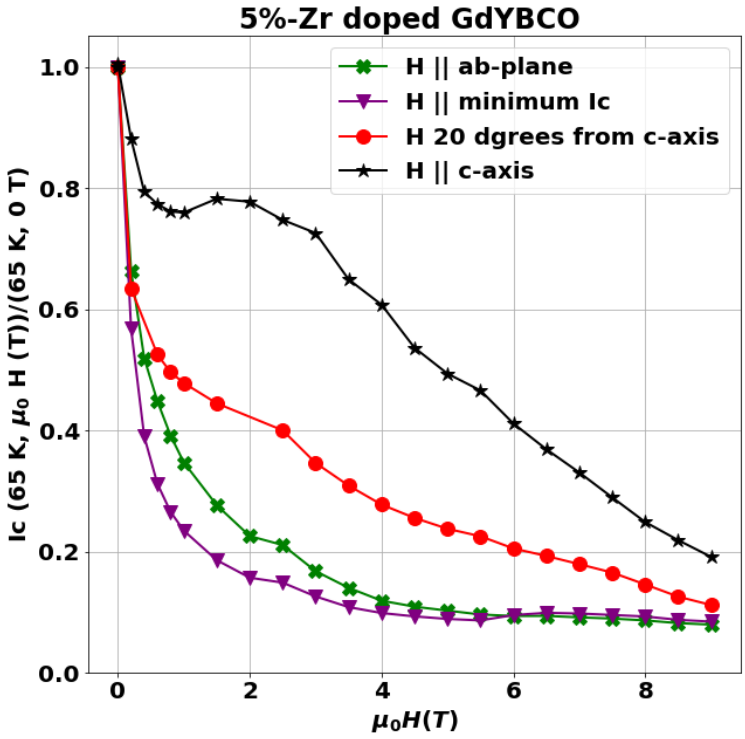

Figure 5-1. Angular dependence of the retention of self-field Ic of a 5% Zr-doped GdYBCO film at 65 K with increasing magnetic field up to 9 T at different orientations.

The pinning landscape of the GdYBCO films can be engineered, and thus made richer, by combining BZO and rare-earth oxides RE_2O_3. RE_2O_3 are precipitates that form in the GdYBCO matrix when the rare-earth content exceeds the normal stoichiometry of GdYBCO. Using the Advanced MOCVD system, it was possible to

form small-sized precipitates that did not interrupt the growth of the BZO nanorods, as observed in Figure 4-1.

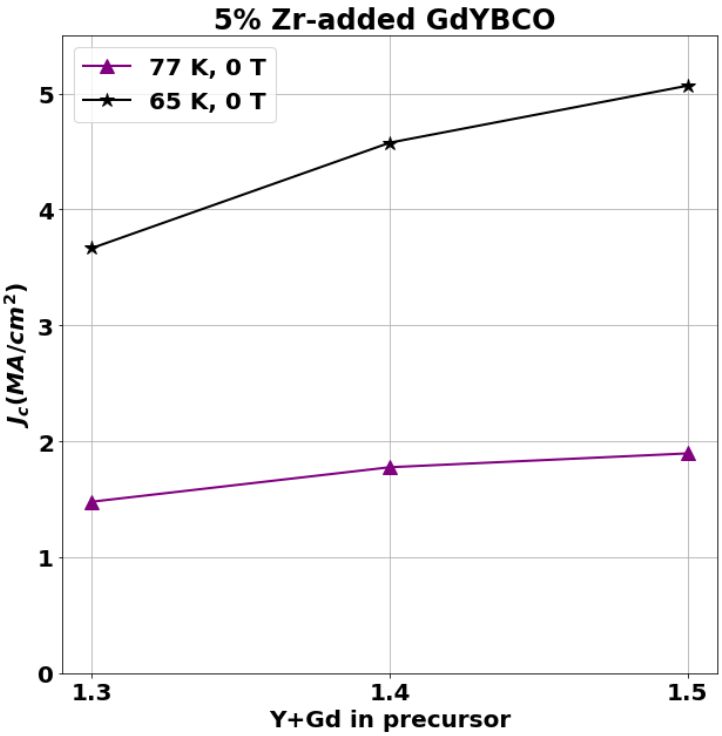

Figure 5-2. Evolution of the self-field Ic at 77 K and 65 K when the Y+Gd in the precursor content was increased from 1.3 to 1.5.

The rare-earth content in the film has a direct effect on the self-field I_c, as noted in Figure 5-2, where the self-field I_c increased by 28% at 77 K and by 38 % at 65 K when the Y+Gd in precursor content was increased from 1.3 to 1.5. The increase in the RE_2O_3 density when the Y+Gd content was raised from 1.3 to 1.5 led to a slight change of the c-axis lattice constant of $REBa_2Cu_3O_7$ from ~ 11.73 Å to ~ 11.75 Å. This slight change in the c-lattice constant can be explained by the small lattice mismatch between the $REBa_2Cu_3O_7$ and RE_2O_3. Further increase in the RE_2O_3 density may lead to a further increase in the c-lattice constant of $REBa_2Cu_3O_7$ and deteriorate the crystallinity of the

film. But, both the increasing self-field I_c and the slight change in the c-lattice constant up to a Y+Gd content of 1.5 indicate that the GdYBCO quality did not yet deteriorate.

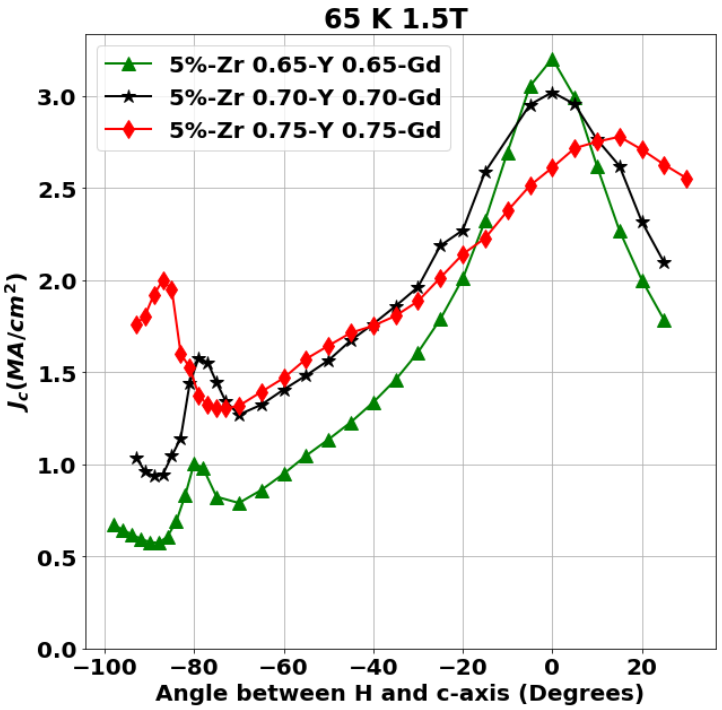

Figure 5-3. Evolution of the angular dependence of critical current density of 5% doped GdYBCO films at 65 K, 1.5 T with increasing Y+Gd content from 1.3 to 1.5.

Figure 5-3 reports the angular dependence of critical current when the Gd+Y content increases from 1.3 to 1.5. While the presence of a c-axis peak in critical current density of all three samples is consistent with the presence of BZO nanorods, an enhancement in the ab-plane critical current density was systematically observed with the increasing RE_2O_3 density. In fact, J_c (H || ab-plane) increased from 1.0 to 1.57 and further to 1.99 MA/cm^2 when the Y+Gd content was raised from 1.3 to 1.4 and 1.5 respectively. This can be explained by an increase of in-plane defect density.

In addition to their effect on the ab-plane pinning, the shape of the RE_2O_3 non-superconducting defects makes them effective also at orientation of magnetic field near B||ab, which explains the enhancement of the minimum critical current densities at 65

K, 1.5 T as observed in Figure 5-3. In fact, the anisotropy ratio, defined as the ratio between the maximum and the minimum critical current density, decreased from 5.6 to 3.22 and further down to 2.13 when the Y+Gd content was raised from 1.3 to 1.4 and 1.5. The effectiveness of pinning by RE_2O_3 over a wider angular range of magnetic field broadened the c-axis peak in J_c, which is important for high-temperature applications. Meanwhile, for the 1.5 Y-Gd sample, the critical current density at B||c decreased to 2.77 MA/cm^2, which indicates the possibility of shorter discontinuous BZO in this film.

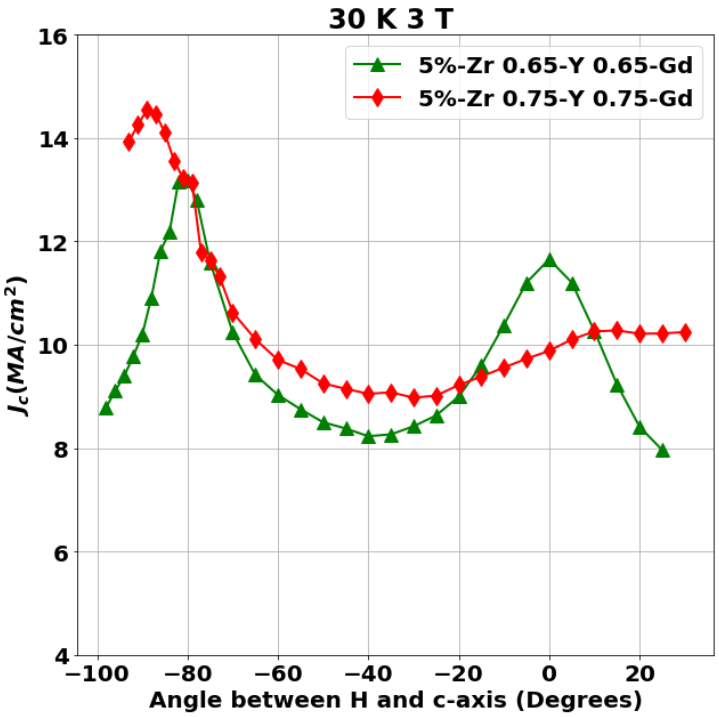

Figure 5-4. Angular dependence of critical current density at 30 K, 3 T of 5% Zr doped GdYBCO films with Y+Gd content of 1.3 and 1.5.

At 30 K, 3 T (Figure 5-4), the sample with higher rare-earth content exhibited minimum J_c and ab-plane J_c, that were higher by 1 MA/cm^2 and 1.4 MA/cm^2, respectively than the corresponding values of the samples with lower rare-earth content.

At B||c, the J_c of the higher rare-earth content sample was lower than that of the lower rare-earth content sample by 1.4 MA/cm^2. Additionally, the higher rare-earth content sample exhibited a wide, almost flat peak in critical current density when the magnetic field was applied parallel to the c-axis.

5.2.2. Multilayers of undoped GdYBCO and Zr-doped GdYBCO

A multi-layered structure of alternating layers of 5% Zr-doped and undoped GdYBCO was fabricated to change the anisotropy observed in the angular dependence of critical current of the Zr-doped GdYBCO films, especially at high temperatures and low magnetic fields. Figure 5-5 presents the cross-section of the multilayered sample constituted of 18 to 22 layers of Zr-doped GdYBCO alternating with undoped GdYBCO layers. The average spacing between the Zr-doped GdYBCO layers was 36 to 44 nm. In Figure 5-6, a microstructure of the multi-layered structure is presented. It is seen that the BZO is in form of round precipitates with an average diameter of 4 to 6 nm with an average spacing of around 5 nm. In some regions, few randomly-oriented short nanorods were observed.

Figure 5-5. Cross-sectional micrograph of the whole thickness of a 0.8-μm GdYBCO film made of multlyaers of undoped GdYBCO and 5% Zr-doped GdYBCO.

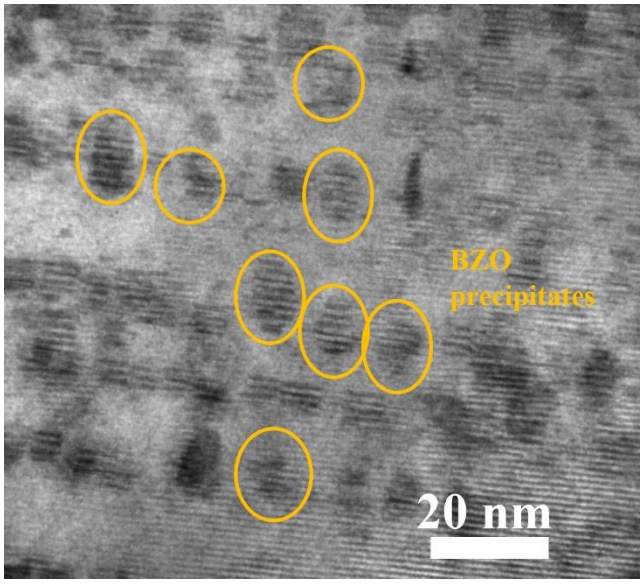

Figure 5-6. A higher magnification microstructure of the multilayered sample described in Figure 5-5.

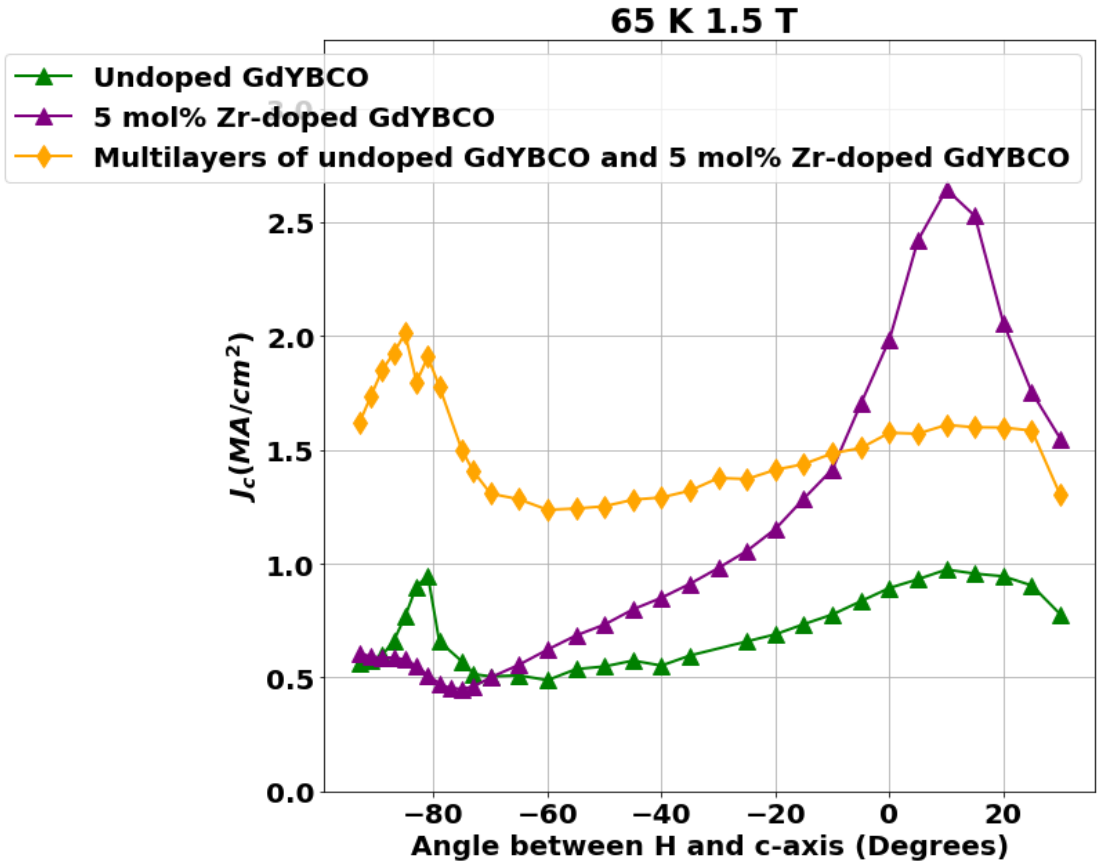

Figure 5-7. Angular dependence of critical current density of ~0.9 μm-thick undoped GdYBCO, a ~1.1 μm-thick 5% Zr-doped GdYBCO, and a ~0.8 μm-thick multilayered sample at 65 K, 1.5 T.

The angular dependence of critical current of an undoped GdYBCO, a 5 mol% Zr-doped GdYBCO, and the multilayered sample at 65 K, 1.5 T with thicknesses in the range of 0.8 to 1.1 μm, are presented in Figure 5-7. Comparing the undoped GdYBCO sample and the 5% Zr-doped sample, we noted the reversed anisotropy in the two samples. While the undoped GdYBCO sample showed a higher ab-plane critical current, the Zr-doped sample exhibited a suppressed ab-plane critical current and a c-axis J_c peak associated with BZO nanorods. The multilayered sample, on the other hand, showed an improvement of the critical current at all magnetic field orientations when compared to the undoped film. The ab-pinning enhancement can be explained by the

presence of non-superconducting BZO phase along the ab-plane that can be effective pinning centers when the magnetic field is applied in this direction. Also, the high density of periodically dispersed BZO round precipitates can truncate and pin a succession of parts of each flux vortex, regardless of the orientation at which the magnetic field is applied, which could explain the enhancement of critical current at all field orientations.

Contrary to the 5% Zr-doped sample where the c-axis critical current was higher than the ab-direction critical current, the multilayered sample had a higher ab-direction critical current. It appears that the BZO round precipitates are not as effective as the BZO nanorods when the magnetic field is applied parallel to the c-axis of the film. The multilayer approach is promising for applications that require an isotopic J_c at 65 K and low magnetic fields but scaling it to a thick film might be challenging.

5.3. ab-plane pinning enhancement by post-process tensile creep-deformation

Commercial Zr-doped REBCO tapes, 12-mm in width with 1.4 μm thick REBCO film made by conventional MOCVD, were used in this work. The superconductor film was grown on a buffer stack comprising of Al_2O_3, Y_2O_3, MgO, and $LaMnO_3$ layers. The buffered stack was based on ion beam assisted deposition (IBAD) of MgO over an electropolished Hastelloy C276 substrate. The tape was coated with silver, 1.8 μm on the REBCO side, and 0.5 μm on the Hastelloy side.

High-temperature tensile creep deformation of the Zr-doped REBCO tapes was conducted with a model 4507 Instron machine. A K-type thermocouple was spot-welded on the substrate side of the tape for monitoring the sample's temperature during the experiment. A direct ohmic heating method was used for heating the tape. The ends

of the tape were clamped in two copper current feedthroughs, as shown in Figure 5-8. A 100 A power source supplied current to the tape and was controlled in a closed-loop with the temperature reading from the thermocouple bonded to the tape. The total length of the tape was 20 cm, with approximately 4 cm on each side of the tape clamped by the copper feedthroughs. The load was monitored by a load cell attached to the sample and the strain was determined by measuring the displacement of the tape. The experiments were done in a closed chamber in 100% ambient oxygen.

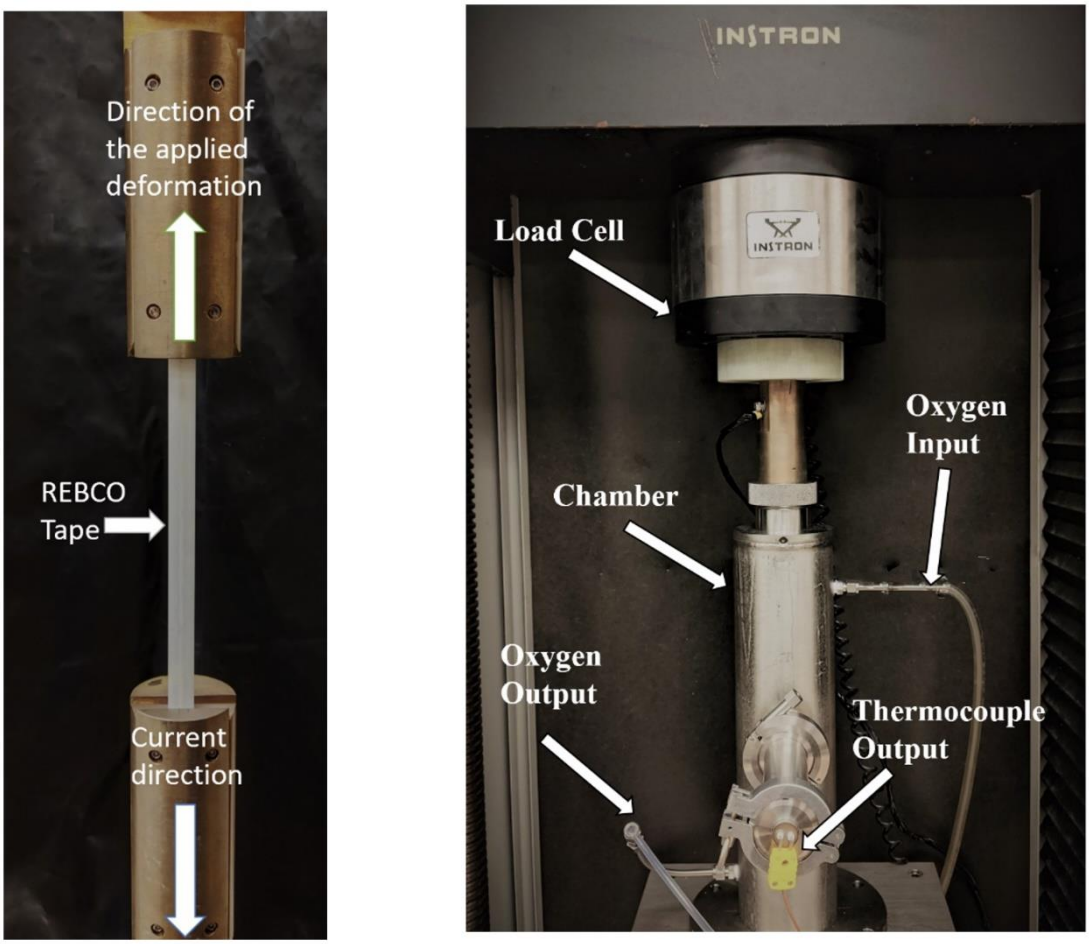

Figure 5-8. Setup used for high temperature tensile deformation of REBCO tape. The tape was clamped between two copper current feedthroughs for direct ohmic heating. The sample was under load in oxygen flow.

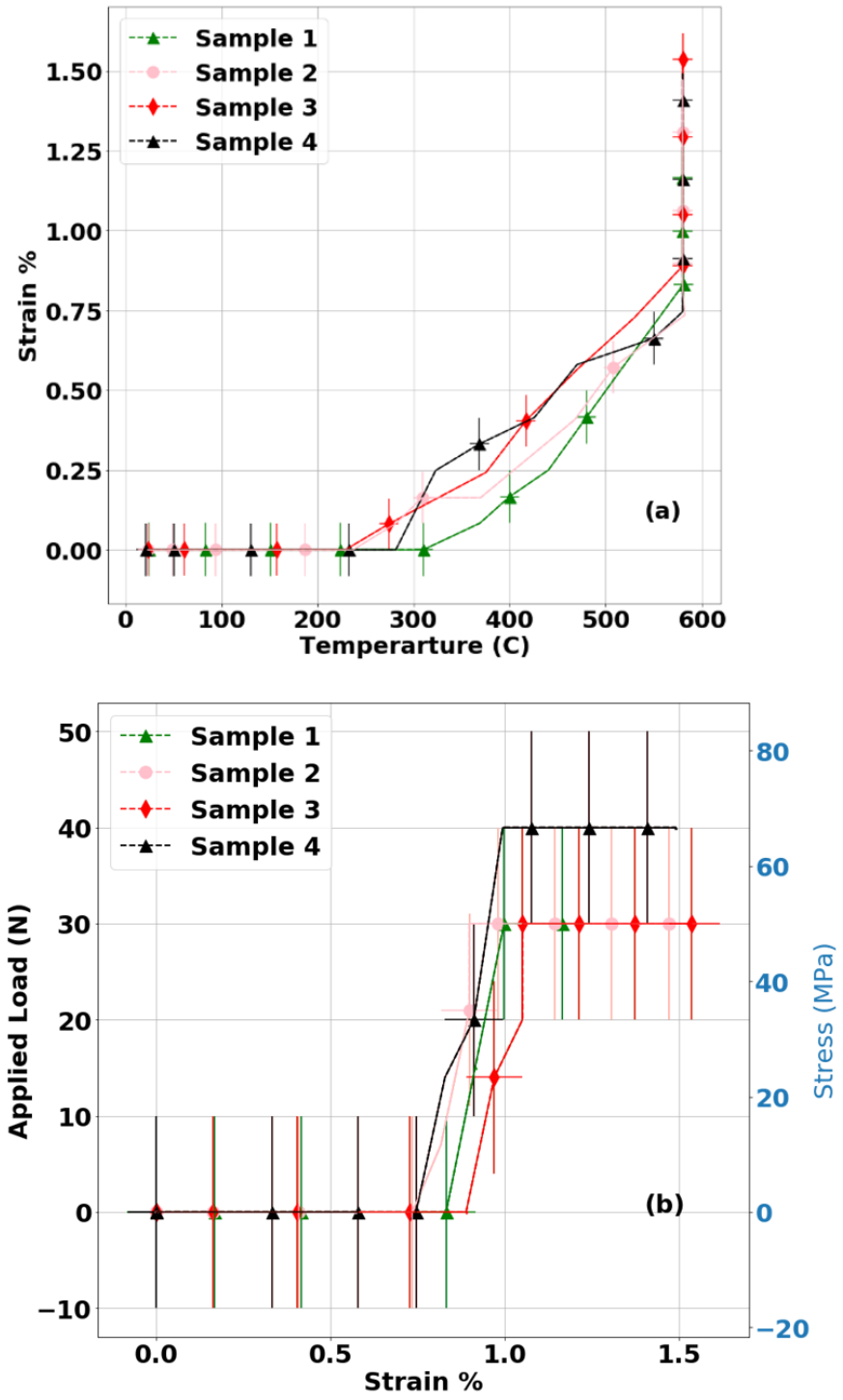

Figure 5-9. (a) Evolution of strain with temperature during the heating of 4 REBCO tapes.(b) Stress-strain curves of 4 REBCO tapes during tensile-creep deformation at 580°C.

The samples were then heated before applying the load at a ramp of ~20°C/min up to ~ 580°C; this resulted in thermal expansion of ~0.7 to 0.8%, as shown in Figure 5-9(a). After reaching ~580°C, a tensile load was applied to the tape. Once the final stress value ~50–70 MPa was reached, the load was maintained, for around 14-20 h, until the desired strain value was obtained, as displayed in Figure 5-9(b). After reaching the desired final strain, the load was released gradually, and the sample was cooled slowly to room temperature. The experiment resulted in permanent plastic deformation.

Table 5-1. Summary of the tensile-creep deformation experiment at 580°C.

Sample #	Applied load	Final strain value	Duration of the experiment	I_c (B || ab) 77 K, 1 T (A/12 mm width)
1	30 N	1.25 %	~ 14 hours	117.1
2	30 N	1.47 %	~ 20 hours	203.9
3	40 N	1.53 %	~ 20 hours	190.5
4	40 N	1.49 %	~ 20 hours	186.5

The results of the tensile-creep deformation of four REBCO tapes are summarized in Table 5-1. It can be noted that the change of the applied load from 30 to 40 N for 20 h had no significant effect on the final strain value. Therefore, the final strain value has been controlled by varying the duration for which the sample was under stress.

Figure 5-10 shows the angular dependence of I_c at 77 K, 1 T for the same tape before and after it was subject to a strain of 1.25% at 580ºC for 14 hours. An increase

in I_c was seen in the deformed tape over a wide range of magnetic field directions. The largest increase in I_c was observed when the magnetic field was applied parallel to the ab-direction of the tape. It is seen that the I_c increased by 43 A (58% of the original I_c) in this direction; the minimum I_c also was enhanced by 15 A (78% of the original I_c).

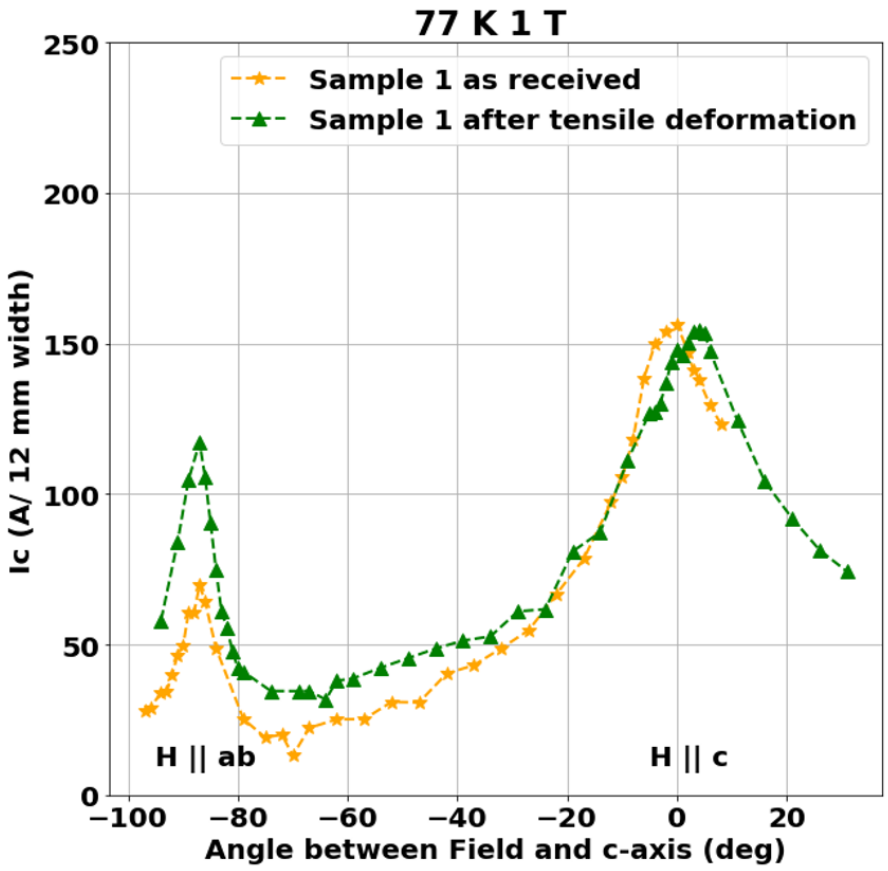

Figure 5-10. Angular dependence of I_c at 77 K, 1T for the same REBCO tape before and after deformation under a tensile load of 30 N at 580ºC for 14 h to reach 1.25 % total strain. The sample exhibited the largest increase in I_c when the magnetic field was applied parallel to the ab-plane.

Further optimization of the final strain values at the same temperature led to a greater enhancement in the pinning at 77 K, especially when the magnetic field was applied parallel to the ab-plane. Figure 5-11 shows the angular dependence of I_c at 77 K, 1 T of an undeformed sample, a sample that was subject to 580°C for 20 hours in oxygen flow without applying load and three deformed samples. All deformed samples

were subjected to tensile deformation for around 20 hours at 580°C. It can be observed that both deformed and undeformed samples exhibited a peak in I_c when the magnetic field was applied parallel to the c-axis of the REBCO film, which is due to the presence of BZO nanorods from Zr doping of the film. The deformed sample showed an increase in I_c when the magnetic field was applied parallel to the ab-direction of the REBCO films. In fact, the deformed samples showed up to 2.8-times higher I_c in this direction. The improvement in ab-direction's I_c reversed the anisotropy of the Zr-doped REBCO films at 77 K, 1 T resulting in a higher I_c in the ab-direction than in the c-direction. Compared to the reference undeformed sample, the sample that experienced only thermal expansion at 580ºC for 20 hours showed no change in critical current at B||c-axis, and a slight improvement in critical current at other field orientations. However, when compared to the sample that was heat treated without load at 580ºC for 20 hours, the samples deformed at 580ºC exhibited up to 2.1 times higher I_c in the direction of magnetic field parallel to the a-b plane. This result clearly shows that the creep deformation, not just the long heat treatment, was responsible for the significant improvement in critical current at B||a-b. No significant difference was seen between the critical current characteristics of sample 2 deformed at 30 N for 20 h and samples 3 and 4 deformed at 40 N for 20 h. This might be due to the fact the final strain levels in all three samples were comparable, as shown in Table 5-1. Comparing with the lower critical current of sample 1 at magnetic field parallel to the a-b plane, shown in Figure 5-10, it is clear that the final strain (which was determined by the deformation time) was more impactful than the deformation load, which indicates the importance of the creep mechanism.

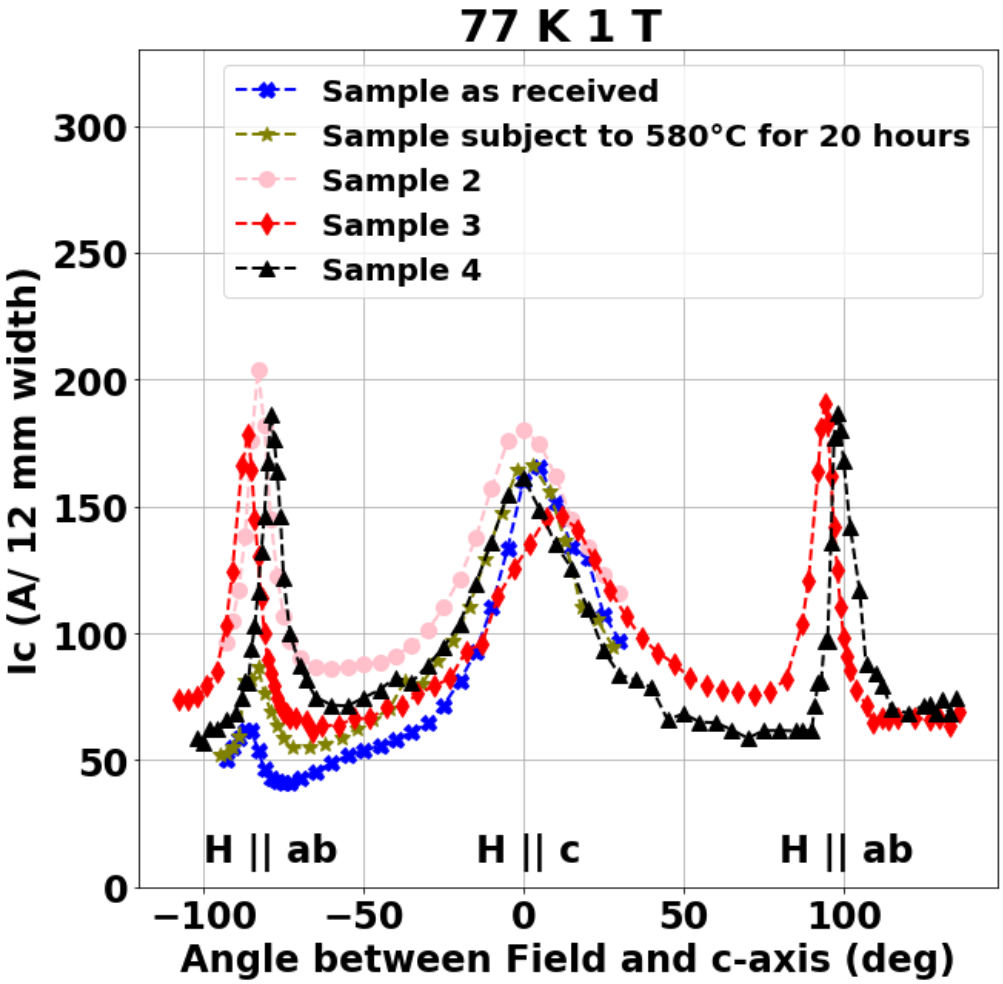

Figure 5-11. Comparison of the angular dependence at 77 K, 1 T of one reference sample, one sample after heat treatment at 580 ºC in oxygen flow for 20 hours without applying load and 3 samples after tensile deformation at 580ºC for 20 hours in oxygen flow.

The magnetic dependence of I_c at 77 K with the magnetic field applied parallel to the ab-direction was studied for Sample 2, the sample that experienced only thermal expansion and no deformation at 580ºC and the reference sample. The results are shown in Figure 5-12. The critical current of the deformed sample was observed to be more than a factor of 2 higher than that of the as received sample and the sample that was subject only to thermal expansion at the same temperature and for the same duration over a wide range of magnetic fields up to the maximum field of 6.5 T.

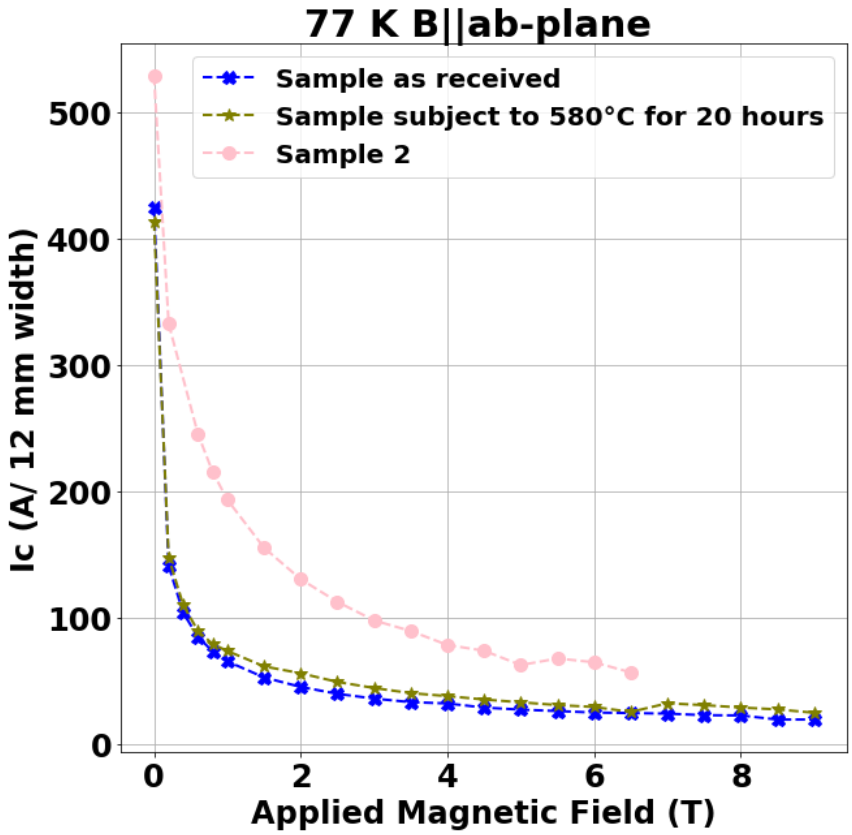

Figure 5-12. The magnetic field dependence of I_c at 77 K of reference, a sample that was in oxygen flow at 580°C for 20 hours without applying load and deformed sample 2 when the magnetic field is applied parallel of the ab-plane.

A cross-sectional microstructure image of Sample 1 after mechanical deformation is shown in Figure 5-13. As expected in this Zr-added sample, continuous BZO nanocolumns aligned along the c-axis were seen throughout the entire film thickness of around 1.4 µm. The observed average diameter size of BZO was 5 nm, while the average spacing between nanocolumns was 23 nm. The matching field corresponding to the BZO distribution was 3.9 T, calculated using $B_\Phi = \Phi_0/a_0^2$, where $\Phi_0 = 2.07\times10^{-15}$ Wb is the magnetic flux quantum, and a_0 is the spacing between BZO nanocolumns. The presence of the BZO nanocolumns explains the strong c-peak

observed at 77 K, 1 T in all the samples presented in this section (Figures 5-10 and 5-11).

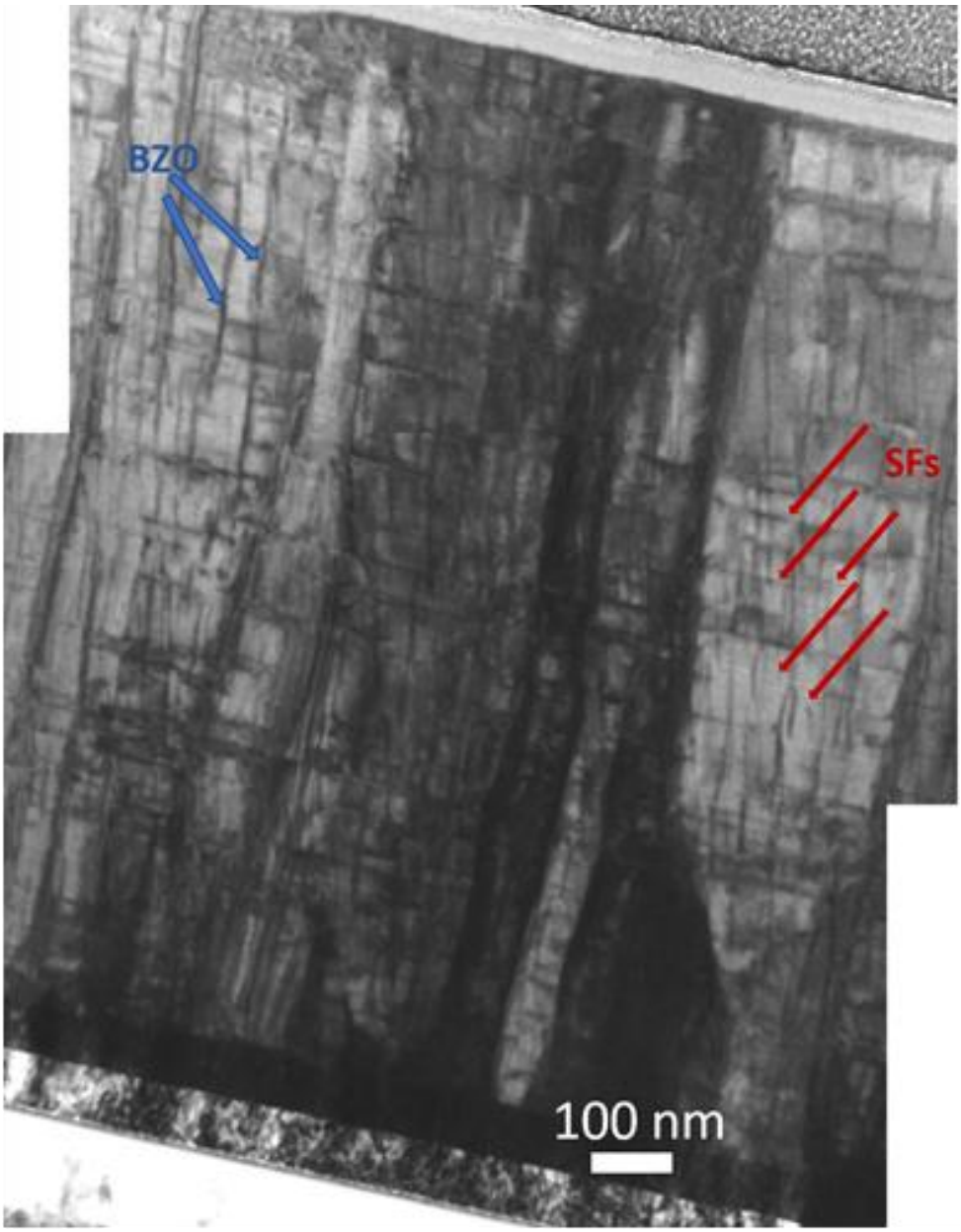

Figure 5-13. Cross-sectional microstructure of Sample 1 after mechanical deformation, showing a high density of stacking faults (SF) present along the ab-planes.

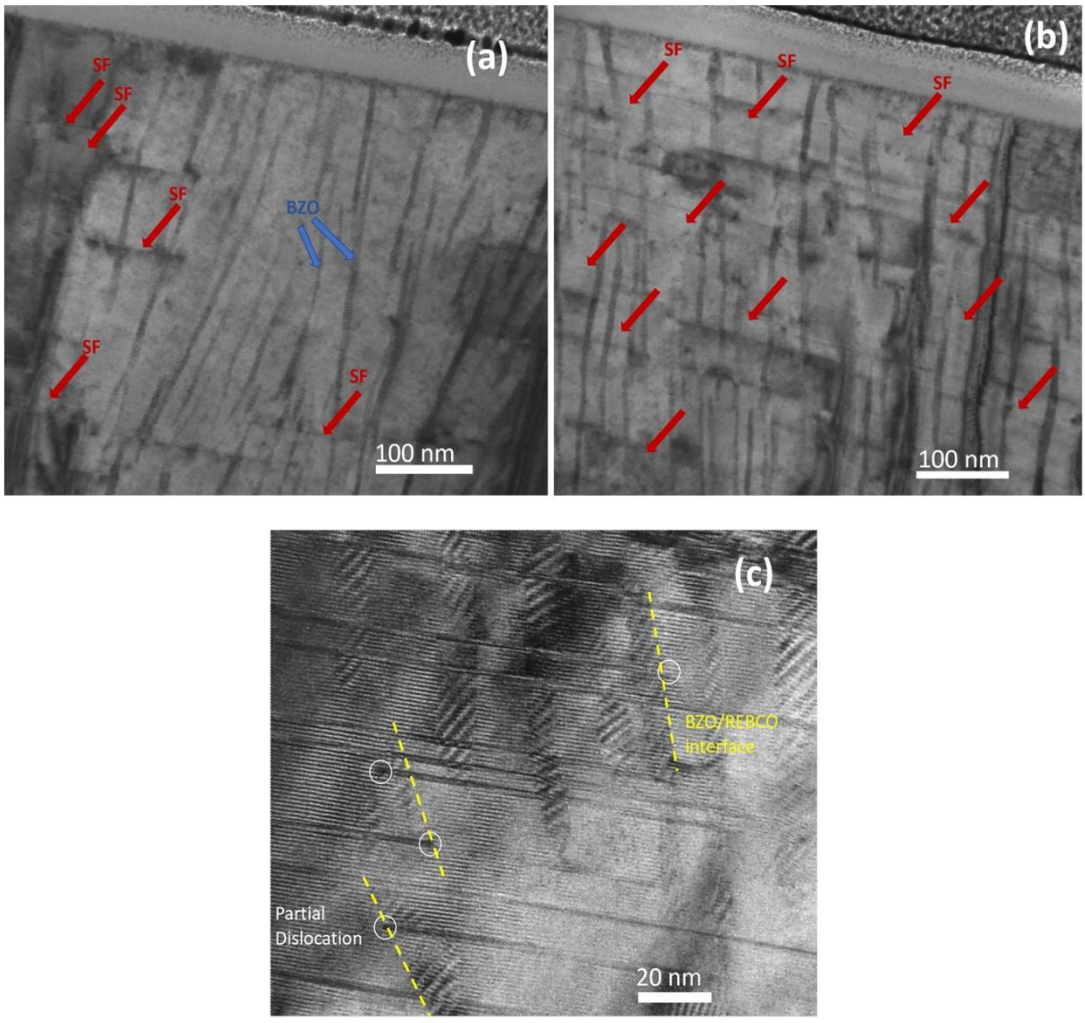

Figure 5-14. (a) TEM micrograph of a cross section of the reference sample. (b) Cross-sectional TEM micrograph at the same magnification of Sample 1 after (c) a high magnification cross-sectional image of the deformed sample.

In Figure 5-13, in addition to the vertically-aligned BZO nanocolumns, domain boundaries along the c-axis and a high density of in-plane stacking faults were observed. The defect structure of the material was dominated by the extraordinarily high density of stacking faults. The observed length of stacking faults ranged between 23 and 30 nm, which corresponded to the spacing between BZO nanocolumns and the REBCO domain boundaries.

The TEM micrographs, is Figure 5-14 (a) and (b) show the microstructures of a reference sample and Sample 1 after mechanical deformation, respectively. The sample that was subjected to the high-temperature tensile-creep deformation showed uniformly-distributed elongated stacking faults along the ab-plane with an average spacing of 10 nm, while the reference sample showed short stacking faults with an average spacing of 36 nm. The ab plane of the REBCO film, where the increased density of stacking faults is found in the deformed sample, is parallel to the direction of the applied tensile deformation. In a higher magnification image (Figure 5-14 (c)), ribbon-like stacking faults passing across the BZO nanocolumns can be observed. In the same image, partial dislocations leading the stacking faults can also be seen. These partial dislocations must have nucleated from the BZO/REBCO interface to alleviate the strain due to the lattice mismatch between the BZO and the REBCO. The formation of these Shockley partials is energetically favorable, since their energy is much lower than that of a perfect dislocation.

5.4. Round wire: an engineering solution to the electromagnetic anisotropy

By reducing the thickness of the substrate to ~20 μm, and using a symmetric tape architecture wherein the REBCO film positioned near the neutral plane, it was possible to increase the bending tolerance of REBCO tapes [100-102]. These tapes were helically wound around copper formers to make round wires of 1.6 to 1.9 mm in diameter (Figure 5-15) [100]. When bent to a radius of 15 mm, a 6-layer round wire had an engineering current density J_e of 586.4 A/mm^2 at 4.2 K and 20 T which is the highest J_e reported on a REBCO round wire at these conditions [100-102].

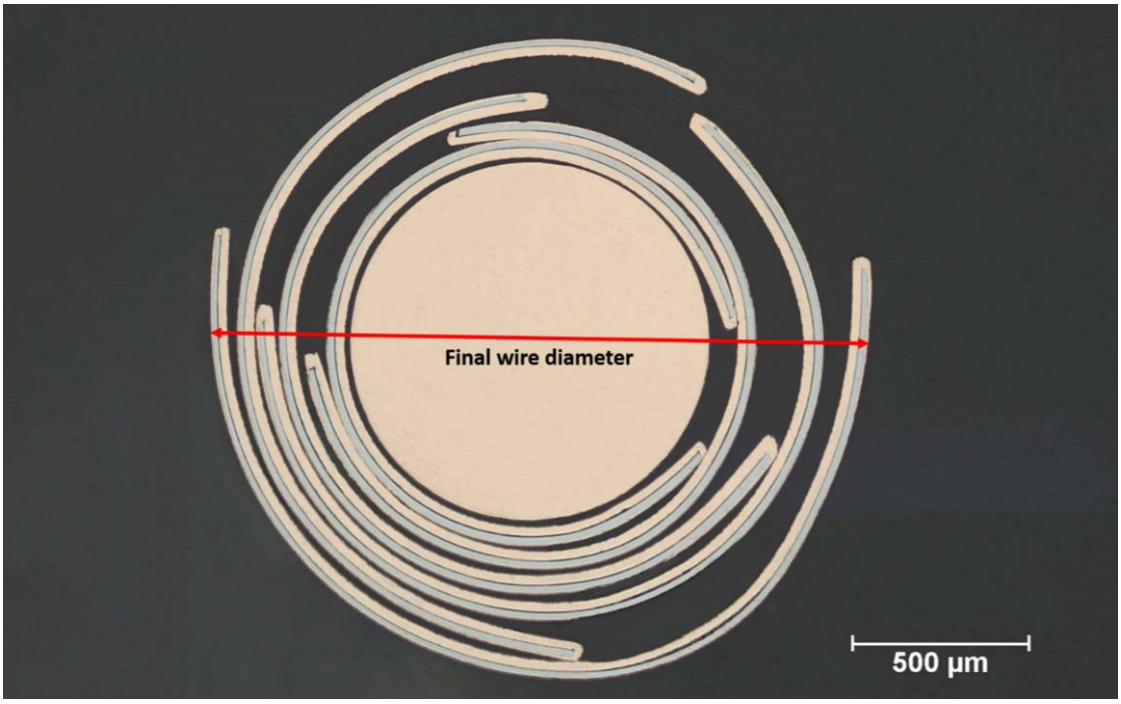

Figure 5-15. Cross-section of a round wire, the total wire diameter is 1.81 mm.

While the 6-layer and 8-layer round wires have an outstanding performance at 4.2 K with the magnetic field applied at a fixed angle, they also have an isotropic structure that might lead to an isotropic angular dependence of critical current. To check the angular dependence of these wires, a 3-layer round wire (Figure 5-16) was made to be tested at 30 K, 65 K, and 77 K in the 9 T system (fewer tape layers were used due to power supply and heat extraction limitations in the 9 T system). The sample was 3.8 cm long, with a total diameter of 1.46 mm. On each side of the sample, 0.5 cm were soldered inside copper blocks that are to be pressed on the current leads in the 9 T probe (Figure 5-16). The end parts of the wire were also sanded into a cone shape to expose each layer and extra solder was included at the end part to ensure contact between the layers. The voltage tabs were soldered at a distance of 1 cm and 1 µV/cm was used as a criterion to define the critical current value.

Figure 5-16. Three-layer round wire made to be measured for angular dependence of critical current in the 9 T system.

The 3-layer round wire had a 77 K self-field critical current of 170.1 A. The angular dependence of critical current of the wire at different temperatures and the magnetic field are reported in Figure 5-17. At 77 K, 1 T, the wire had a maximum I_c of 49.2 A and a minimum I_c of 41.7 A. The anisotropy ratio at 77 K, 1 T was equal to 1.17. At 65 K, 1.5 T it had a maximum I_c of 140 A and a minimum I_c of 116.9 A. The anisotropy ratio at 65 K, 1.5 T was equal to 1.19. At 30 K, 5 T the wire had a maximum I_c of 316 A and a minimum I_c of 272.2 A. The anisotropy ratio at 30 K, 5 T was equal to 1.16. Such values of anisotropy in both the strong and weak pinning regimes are

much lower than what was reported in the original tape, where the anisotropy ratios were equal to 4.02 at 77 K, 1 T and 2.60 at 30 K, 3 T, Figure 5-18.

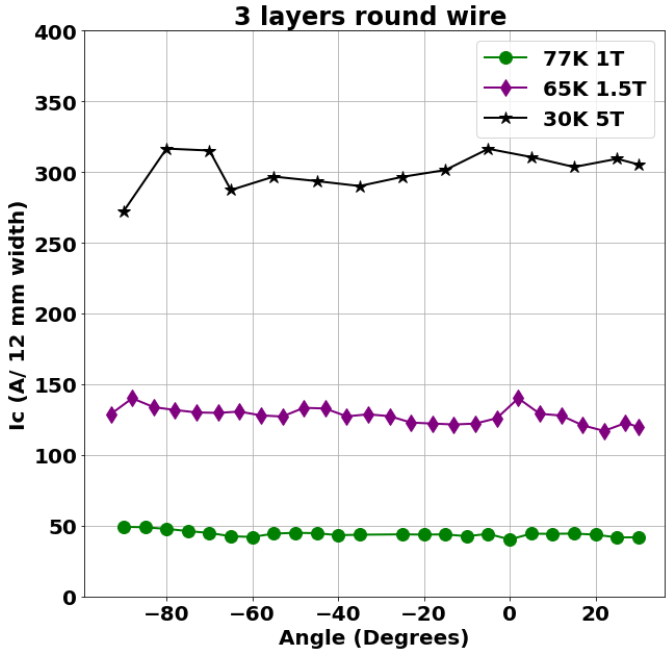

Figure 5-17. Angular dependence of critical current of a three-layer round wire at 30 K, 65 K and 77 K showing an isotropic critical current.

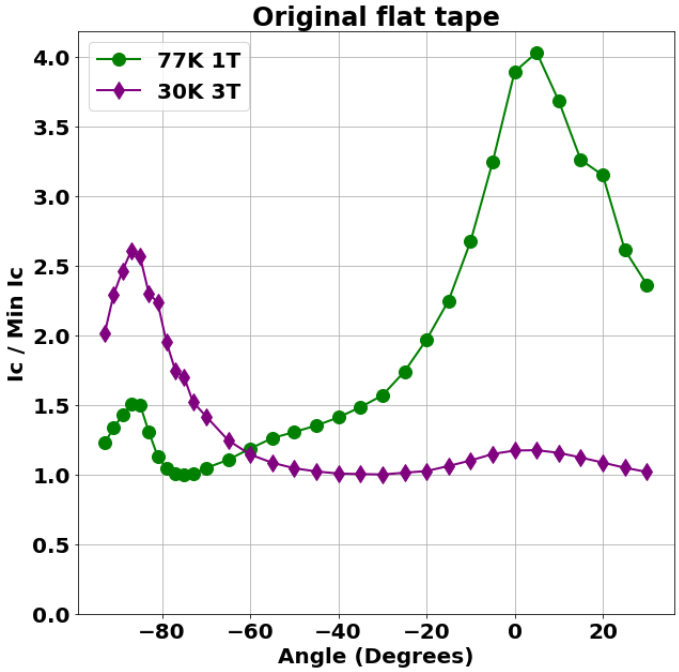

Figure 5-18. Angular dependence at 30 K and 77 K for the original flat tape. The critical current was normalized to its minimal value for clarity.

5.5. Conclusions

While winding the flat REBCO tapes into round wires made their critical current almost independent of the direction of the applied magnetic field in both the weak and strong pinning regimes, combining other pinning mechanisms with the BMO doping is still a valuable addition since they lift the critical currents in magnetic fields directions other than along the c-axis of the film and might result in enhancing the isotropic critical current of the round wires.

Using the Advanced MOCVD system, it was possible to form small RE_2O_3 precipitates that did not interrupt the growth of BZO and, by varying the composition of the GdYBCO films, it was possible to control their density. This resulted in doubling the J_c (H || ab-plane) at 65 K, 1.5 T when the Y+Gd in precursor composition increased from 1.3 to 1.5.

A multilayer architecture of alternate layers of undoped GdYBCO and Zr-doped GdYBCO is a second method to change the pinning architecture of the Zr-doped GdYBCO films and thus modify their magnetic field angular dependence of critical current. Films with such architecture showed an enhanced critical current over the whole range of magnetic field orientations when compared to an undoped GdYBCO film of similar thickness. Such a method, while promising for applications that require isotropic pinning, might be challenging when scaled up to roll-to-roll manufacturing of thicker films.

Tensile-creep deformation at 580°C of commercial Zr-doped REBCO tapes, on the other hand, resulted in a drastic improvement in critical current at 77 K. A strain-

dependent improvement in critical current was observed, especially when the magnetic field was applied parallel to the ab-direction of the REBCO film. TEM investigation of a sample that was subject to ~1.25% of total strain showed approximately 3.6-times more ab-plane stacking faults compared to a reference sample. While stacking faults are an established pinning mechanism at 77 K, in this work, a new method to increase their density and thus enhance the performance of REBCO films has been demonstrated in this work.

Chapter 6. Prediction of low-temperature critical currents using Artificial Neural Networks

6.1. Introduction

There is a lack of critical current data and systematic studies, especially at 4.2 K and high magnetic fields. Continuous non-destructive critical current measurements over 100% of length of long superconducting tapes at low temperatures and high magnetic fields remain extremely challenging. Therefore, predicting low-temperature, high magnetic field critical currents using data from measurements at higher temperatures and lower magnetic fields would be beneficial.

Critical currents at 77 K and 3 T were previously shown to correlate well with 30 K and 3 T measurements [103], and this study was performed using a set of 28 samples, all of which were 15% Zr-doped and approximately 1 μm thick. Based on this result, a reel-to-reel nondestructive critical current measurement tool was built to predict the 30 K and 3 T critical current of long tapes by measuring their critical currents at 77 K and 3 T [104].

In this chapter, machine learning methods were applied to predict critical currents at 4.2 to 40 K using the critical current values at 65 K. Critical current measurements at 65 K are relatively easy because they can be obtained using liquid nitrogen, and because the critical current values are lower at this temperature, the risk of burning the samples is lower.

6.2. The data

The dataset used in this experiment consisted of 349 samples. These samples were deposited using the Advanced MOCVD system. Because the growth conditions were varied during the deposition of the REBCO films (e.g., growth temperature and flow rate), to optimize the deposition process, the dataset contained both good- and poor-performing samples.

In addition to the different deposition conditions, compositions of the samples also varied. The Ba content ranged from 1.85 to 2.35 while the rare-earth content varied from 1.30 to 1.60. The Zr additions in these samples ranged from 0 to 20 mol.%, with some of the samples containing layers of different Zr amounts. In cases where the deposition time and molarity were varied, the samples covered a wide range of thicknesses, from 0.5 to approximately 8 μm (Figure 6-1).

The dataset included in-field magnetic critical currents of the 349 samples from 0 to 13 T at the following six different temperatures: 4.2, 20, 30, 40, 65, and 77 K. In-field critical current was measured while the magnetic field was applied perpendicular to the tape using the PPMS VSM system that was presented in Chapter 2.

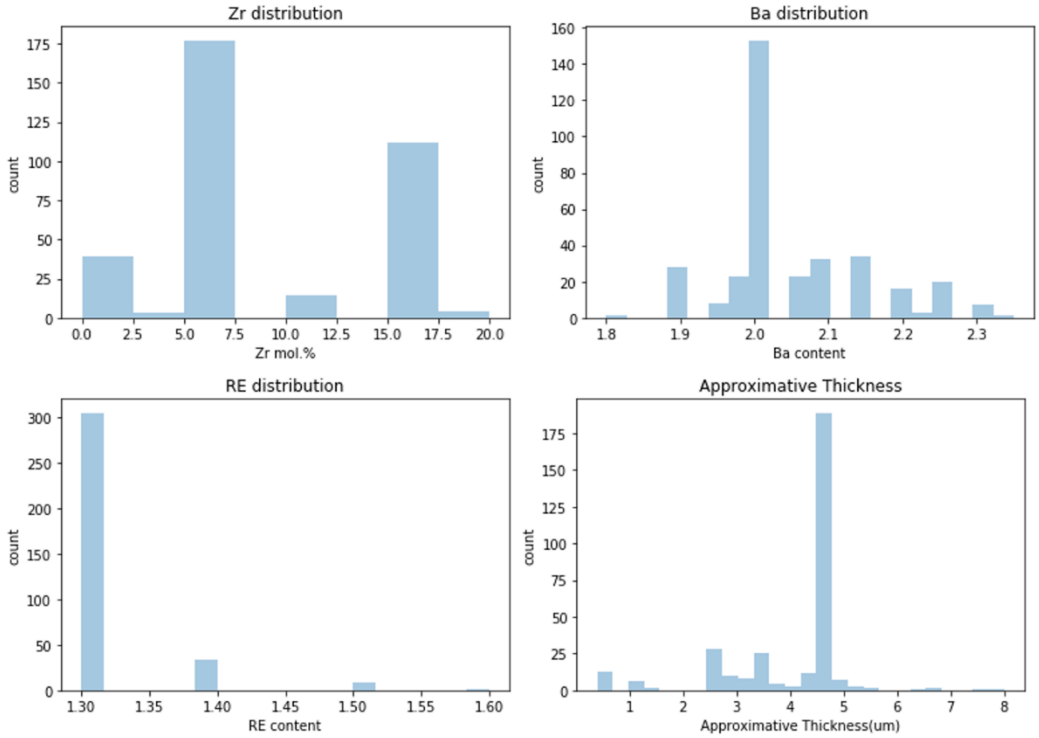

Figure 6-1. Distribution of compositions and thicknesses of REBCO films within the dataset that was used to predict the in-field critical currents.

6.3. Artificial Neural Networks

Machine learning is an application of artificial intelligence that uses data to solve complex problems such as classification, clustering, and regression. Artificial neural networks are one of the most frequently-used machine learning methods. An artificial neural network is a matrix of interconnected nodes or neurons, which models the neurons in a human brain. Each neuron has several inputs, including their respective weights, a bias, an activation function, and an output (Figure 6-2).

A neural network, as shown in Figure 6-3, contains one to multiple layers of neurons to perform a function approximation. The inputs of the first layer are the model inputs from the dataset, such as the critical currents at 65 K and different magnetic

fields. The output of the final layer of the network is the result that is to be predicted using the model, such as the critical current at 4.2 K and 11 T.

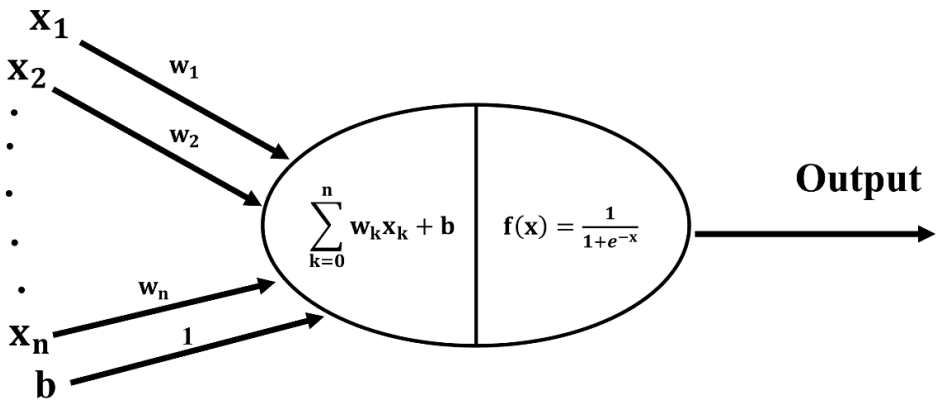

Figure 6-2. An artificial neuron, where w_k is the weight of every input x_k, b is the bias, and f(x) is the activation function.

MLPRegressor is a regression neural network that is offered by the library Scikitlearn [105], and was used in Python 3.6 in this work. The dataset was randomly sampled into a training and an evaluation dataset. Approximately 75% of the data was used to train the model, while the rest of the data was utilized to evaluate the accuracy of the predictions. The dataset was randomly split to limit the risk of information leakage between the training and the evaluation modes. The data was also scaled to be in the same range of values. Scaling the numeric values is important to avoid features with high numeric values (e.g., critical current at 65 K and 1 T) dominate the features with lower numeric values (e.g., critical current at 65 K and 13 T). Z-score normalization was used for this purpose; it scales each feature so that its mean value is 0 and its variance is 1.

The logistic sigmoid function,

$$f(x) = \frac{1}{1 + e^{-x}} \ , \qquad \text{Equation (6-1)}$$

was used as an activation function, and a stochastic gradient-based optimizer gave the best results for weight optimization [106].

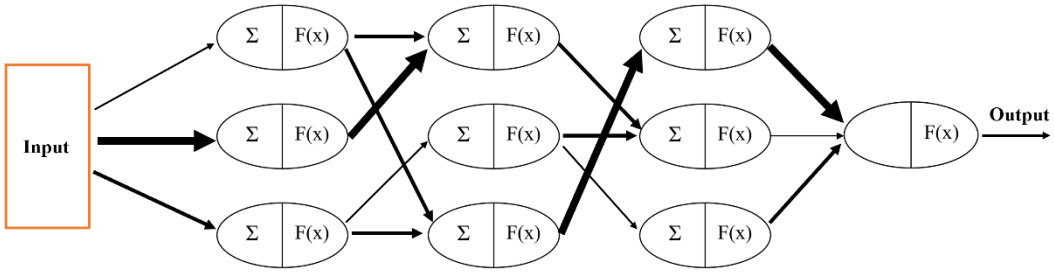

Figure 6-3. A feed-forward neural network where the weights are optimized based on the output of the previous layer of neurons, with three hidden layers

6.3.1. Evaluation Metrics

To evaluate the accuracy of the predictions, the predicted critical current values from the evaluation dataset were compared to the measured critical currents. The following statistical metrics were used to satisfy this purpose:

- **R^2:** The R-squared also known as the coefficient of determination is a statistical measure that represents the proportion of the variance in a dependent variable that is predictable from an independent variable or variables [107]. R-squared explains to what extent the variance of one or multiple variables explains the variance of another variable. This means that if the R^2 of a regression model is equal to 1, then all the observed variation in the output is directly related to the model's inputs. This is shown in Equation 6.2 below.

$$R^2 = 1 - \frac{\sum_i^n \left(y_i - f(x_i)\right)^2}{\sum_i^n (y_i - \bar{y})^2} \ , \qquad \text{Equation (6-2)}$$

where y_i is the ith value to be predicted and x_i is the ith value of the input variable.

- **The adjusted R^2:** Similar to the R^2, the adjusted R^2 indicates how well the data fit a curve, but it adjusts to the number of inputs in the model. The adjusted R^2 decreases when useless variables are added to the model.

$$R^2_{adj} = 1 - (1 - R^2)\frac{n-1}{n-p-1} \ , \qquad \text{Equation (6-3)}$$

where p is the total number of inputs in the model and n is the sample size.

6.4. Results

Among the whole dataset, 100 samples were randomly selected to verify the accuracy of the predictions. After training the model using the rest of the dataset (249 samples), the model was applied to the 100 samples that were used to verify the accuracy (the evaluation dataset). Figure 6-4 shows the plots of the predicted values of critical currents at 4.2, 20, 30, and 40 K and different magnetic fields up to 13 T for the 100 samples compared with their actual critical currents measured at the same temperatures and magnetic fields. The model input was the normalized critical current values at 65 K and the following magnetic fields: 0, 1, 3, 5, 7, 9, 11, and 13 T.

Table 6-1. Evaluation of the prediction accuracy by comparing the predicted and the actual critical currents in the evaluation dataset (100 samples).

Temperature (K)	40			30			20			4.2		
Magnetic Field (T)	0	5	13	0	5	13	0	5	13	0	5	13
R^2	0.98	0.98	0.94	0.98	0.97	0.92	0.96	0.94	0.91	0.94	0.90	0.87
Adjusted R^2	0.97	0.97	0.92	0.97	0.95	0.89	0.95	0.91	0.88	0.92	0.87	0.82
Mean absolute error (A)	97	52	32	169	93	61	366	197	96	657	426	231
Average Error %	0.2	1.4	2.0	0.5	1.8	1.8	0.6	2.7	1.8	1.2	4.5	2.8

Figure 6-4 and Table 6-1 show that the model was able to predict the actual critical current in all the tested fields and temperatures with great accuracy. The lowest R^2 values registered for critical currents at 13 T and 40 K, 30 K, 20 K, and 4.2 K were 0.94, 0.92, 0.91, and 0.87 respectively.

In addition to the high R^2 values (close to 1) that indicate the existence of a good fit between the predicted and the actual critical current values at all temperatures and magnetic fields, the corresponding adjusted R^2, Equation 6-3, was close to the actual R^2 value, and the difference was less than 0.05 for all the compared values. Having an adjusted R^2 close to the actual R^2 value indicates that the critical currents from the entire

range of magnetic fields from 0–13 T at 65 K contributed to the prediction of the critical currents at each field at temperatures lower than 65 K. This means that no unnecessary inputs were used to train the model.

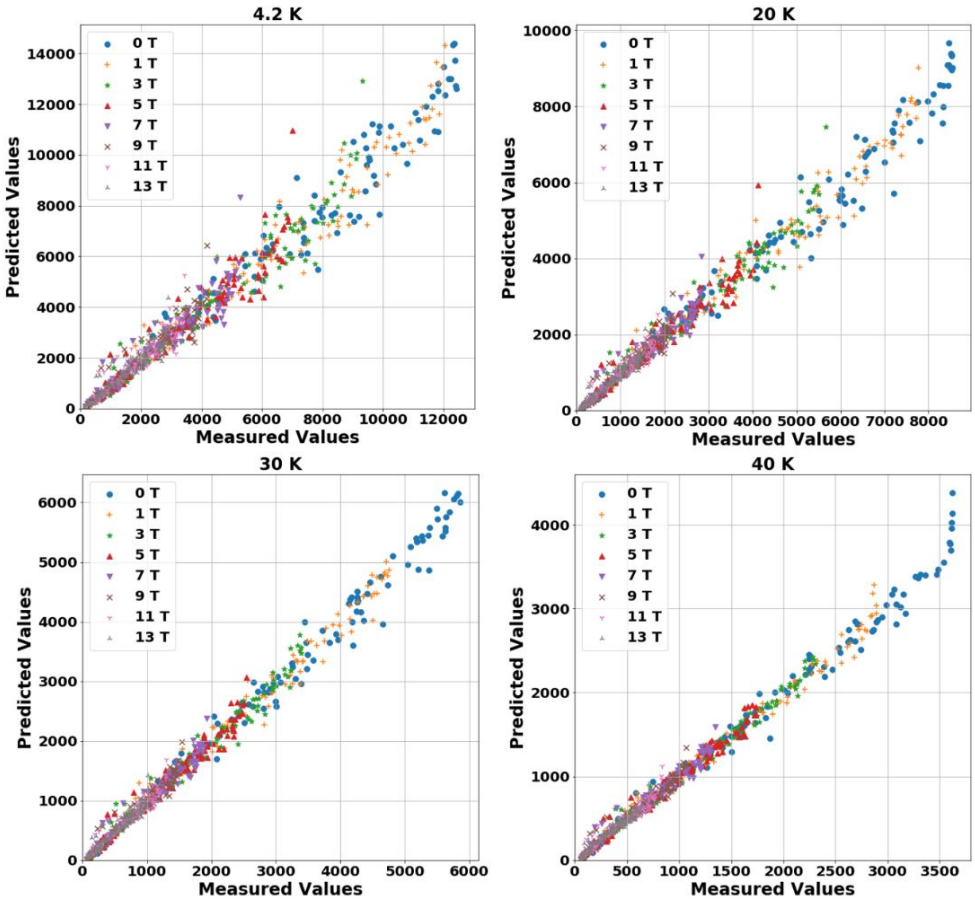

Figure 6-4. Comparison between the measured critical currents and the predicted critical currents in the evaluation dataset (100 samples) at different temperatures and applied magnetic fields.

In Table 6-1, the average error % between the predicted and the actual critical current at different temperatures and magnetic fields is presented. This value was below 4.5% for all conditions, which, in addition to the high R^2 value, confirmed the capability of the model to predict the critical current values at low temperatures with good accuracy.

6.4.1. Cross-validation

To further evaluate the precision of the predictions, k-fold cross-validation was applied to the dataset. In k-fold cross-validation, the dataset is divided to k folds. Each fold contains 1/k cases and is created by random sampling of the dataset. In each iteration of the cross-validation, k−1 folds were used to train the model and one-fold was used for testing the accuracy of the prediction, as illustrated in Figure 6-5. This process was repeated for k iterations.

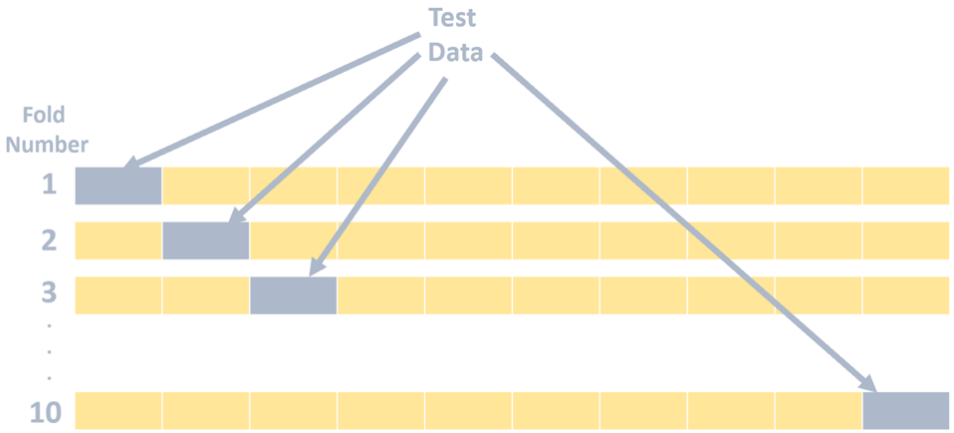

Figure 6-5. Ten-fold cross-validation. The data was randomly separated into ten folds. The model was trained and tested ten times, whereas the data was trained using nine folds and tested using the remaining fold.

Cross-validation helps avoid overfitting the data and reduces the risk of an over-promising model that may not work when applied to a different dataset. Ten-fold cross-validation was used to evaluate the model that was built previously, and it yielded the results shown in Table 6-2. It was applied to the training dataset that was used to build the model, which contained 249 samples.

The results of this process are summarized in Table 6-2. At every iteration, the model was able to predict the critical current at every temperature and magnetic field with an acceptable accuracy, $R^2 \sim 0.9$, and with an average error% <5% in all cases.

Table 6-2. Mean values and standard deviations of the R^2 and the mean absolute errors obtained at every iteration of the ten-fold cross-validation applied to the training set that was used to build the initial model.

Temperature (K)	40			30			20			4.2		
Magnetic Field (T)	0	5	13	0	5	13	0	5	13	0	5	13
Mean R^2	0.98	0.98	0.94	0.96	0.96	0.92	0.94	0.92	0.89	0.91	0.86	0.85
Standard deviation of R^2	0.007	0.006	0.02	0.01	0.01	0.03	0.02	0.03	0.03	0.02	0.04	0.05
Mean of Mean Absolute error (A)	92	52	31	224	100	58	439	196	96	794	432	227
Standard deviation of Mean of Mean Absolute error (A)	16.7	7.4	6.1	28.4	11.8	11.8	61.1	37	14.9	97.4	58.8	29.3

6.5. Discussion

The effectiveness of different pinning mechanisms varies with the temperature and applied magnetic field [29, 41, 108-111]. For example, while weak pinning is more dominant at low temperatures, below 30 K [83, 84], strong pinning that was introduced by the BZO nanocolumns is dominant at high temperatures[26, 83, 84]. From the

existence of this boundary between the weak and strong pinning regimes, one can conclude that it might not be possible to accurately predict the critical currents at low temperatures using critical currents from the high temperatures. However, the opposite was found using machine learning, where it was possible to predict the critical currents at 4.2 K using their values at 65 K despite using a database that contained samples that were engineered with different pinning mechanisms (i.e., different rare-earth and zirconium contents).

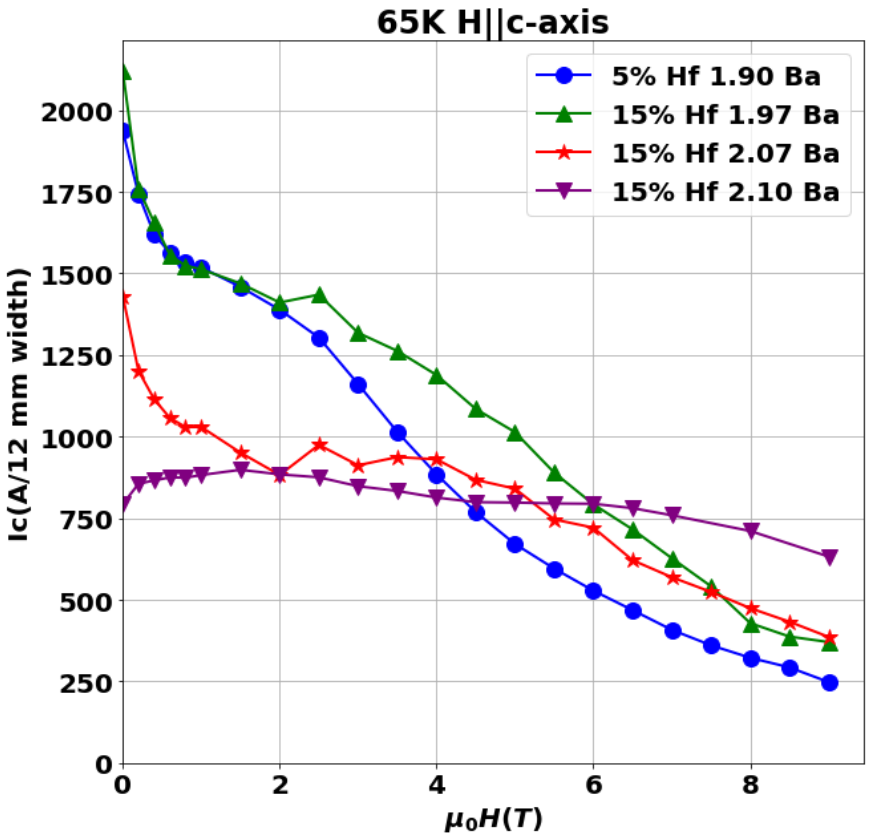

Figure 6-6. Transport critical current at 65 K that was used as an input to the model to predict the transport critical current at 4.2 K.

To check if the model is applicable to transport critical currents, it was applied to the transport critical current data from the 9 T system (magnetic fields up to 9 T) and transport critical currents measured at the National High Magnetic field at 4.2 K up to

31.2 T. The 65 K, B||c-axis I_c data from 0 to 9 T were used as an input to predict the transport critical currents at 4.2 K from 0 to 13 T. The model's output was then compared to the critical currents that were obtained from the National High Magnetic field lab at 4.2 K and fields up to 31.2 T. The predicted data from the statistical model was combined with the power law function, $I_c \sim H^{-\alpha}$ to predict I_c values up 32 T.

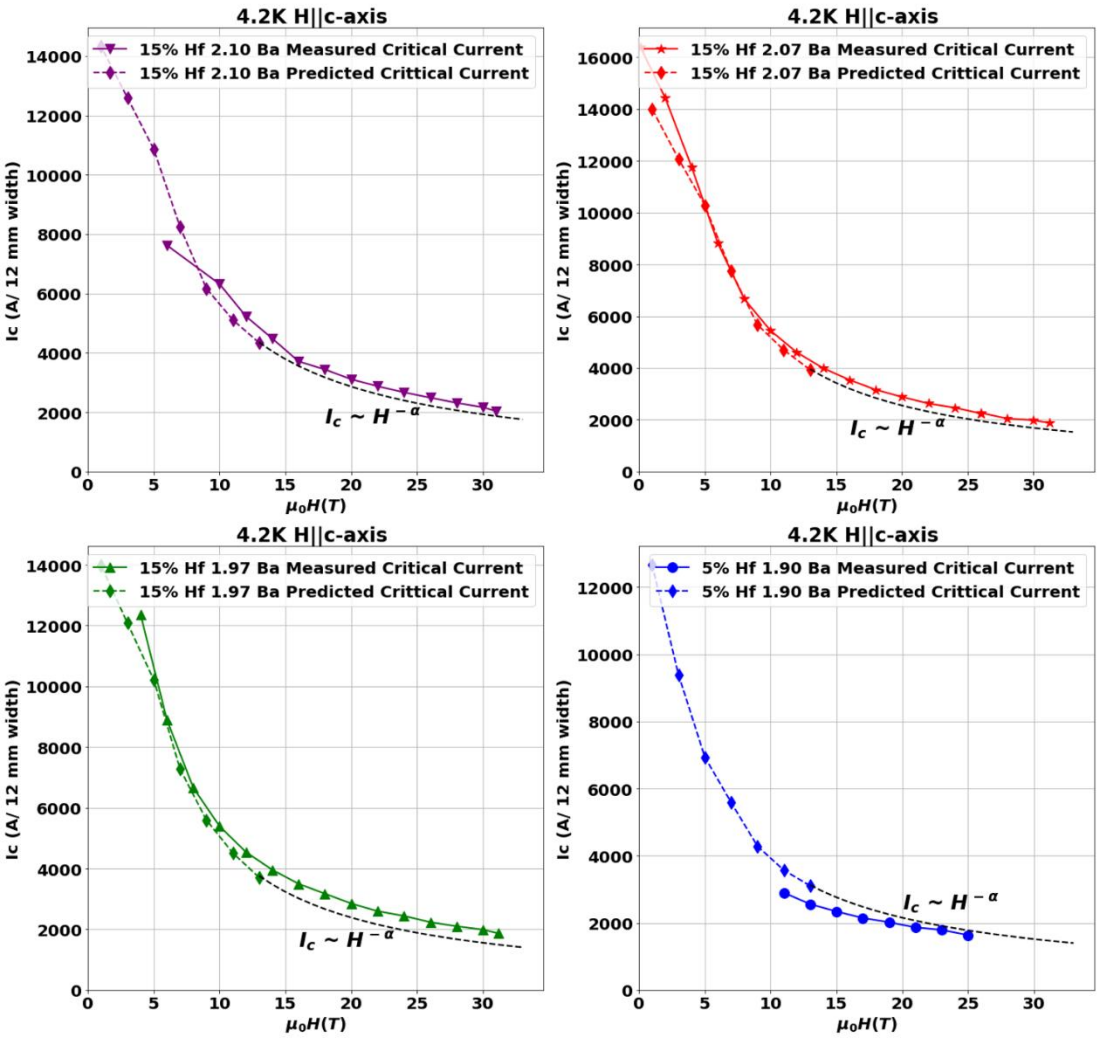

Figure 6-7. Prediction of transport critical currents at 4.2 K up to 31 T by combining statistical and physics-based models using 65 K data. The predicted critical current was then compared to the actual critical current.

Table 6-3. Properties of the samples that were used in transport critical current measurements to verify the accuracy of the model.

Sample #	Composition of MOCVD precursor	Thickness (μm)	Alpha value at 4.2 K from the Measured I_c	Alpha value at 4.2 K from the Predicted I_c
1	5% Hf, Ba= 1.90, Cu=2.60, Y=0.65, Gd=0.65	3.8	0.863	0.766
2	15% Hf, Ba= 1.97, Cu=2.60, Y=0.65, Gd=0.65	3.7	1.055	1.055
3	15% Hf, Ba= 2.07, Cu=2.60, Y=0.65, Gd=0.65	4.4	0.933	0.992
4	15% Hf, Ba= 2.10, Cu=2.60, Y=0.65, Gd=0.65	4.3	0.974	0.957

The transport critical current samples that were used to verify the model compatibility with transport measurements (Figure 6-6 and Table 6-3) were Hf-doped. Although none of the 349 samples that were used to develop the model were Hf-doped, the model was able to predict the critical currents with an acceptable accuracy (Figure 6-7).

Table 6-3 shows the alpha values from the predicted and the actual critical current values. The alpha value was used to predict the critical currents at 4.2 K and magnetic fields up to 32 T.

6.6. Conclusions

Artificial neural networks were successfully utilized to predict in-magnetic field critical currents at temperatures below 40 K based on data from 65 K measurements.

The model was able to predict the magnetic critical currents in magnetic fields up to 13 T. The artificial neural network was trained and validated, and then applied on transport measurements combined with the power law fitting, $J_c \sim H^{-\alpha}$, to predict critical current values in magnetic fields up to 31.2 T at 4.2 K. The model showed an average error of 2.8% at 4.2 K and 13 T when applied on a validation dataset containing 100 samples. The ability of the model to predict the critical current in the weak pinning regime (4.2 to 30 K) based on the critical currents at 65 K (strong pinning regime) shows that, while the efficiency of strong pinning centers may vary with temperature, they play a role in pinning at all the operating temperatures and magnetic fields.

The presented model developed in this work can be used to optimize REBCO tapes, especially for low temperatures and high magnetic field applications where the actual measurements are complicated to perform. It also enables evaluation of the critical current of long tapes at low temperatures and high magnetic fields. Based on continuous non-destructive in-magnetic field critical current measurements at high temperatures [104], the statistical model developed in this work can be used to predict critical currents of long superconducting tapes at 4.2 K.

Chapter 7. Summary and Future studies

Flux pinning in thick film REBCO coated conductors was studied in this dissertation to support research on enhancing their critical currents over a wide range of temperature and magnetic fields as well as on reducing the anisotropy and field and thickness dependencies of critical current. In chapter 3, assessment of 5% Zr-doped REBCO films up to 4.8 μm-thick grown using an advanced MOCVD reactor, that allows a higher control of the deposition process, was presented. XRD and TEM analyses revealed no degradation of crystallinity or formation of misoriented a-grains with increasing film thickness. At 65 K and 1.5 T (B||c-axis), a 4.8 μm-thick film had an I_c of 1722 A/12 mm which corresponds to a J_c of 3 MA/cm^2. A maximum of pinning force at 65 K (B||c-axis) of 87 GN/m^3 was achieved in the 4.8 μm-thick film at a matching field of 4 T.

In chapter 4, a detailed J_c (H, T) study was presented on 4 – 5 μm thick film REBCO samples with different BMO doping (B: Ba, M: Zr, Hf, and Nb) and with different doping concentrations (3 to 15 mol%) to investigate the effect of the density, size, and continuity of the BMO on J_c. Higher critical current values at higher magnetic fields were observed in the higher dopant samples and in the samples where continuous nanorods were observed in TEM. From TEM observations and correlated pinning analysis, it appears that a higher density of continuous nanorods helps to achieve higher pinning forces and matching fields by building a stronger pinning matrix..

In chapter 5, the effect of RE_2O_3 precipitates combined with $BaZrO_3$ nanorods on reduction in the anisotropy of critical current of Zr-doped REBCO was investigated. Increasing the density of the RE_2O_3 precipitates in 5% Zr-doped REBCO resulted in

doubling the J_c (B||ab-plane) and in enhancing the minimum J_c at 65 K, 1.5 T. To further enhance the minimum critical current at 65 K, 1.5 T, a multilayer of undoped REBCO and Zr-doped REBCO was engineered. The multilayered film showed an enhancement of J_c over a wide range of magnetic field orientations when compared to a 5% Zr-doped film. Post-deposition tensile creep-deformation was then introduced as a post-process method to enhance the critical current of Zr-doped REBCO films. Samples that were subjected to deformation at 580°C for 20 hours showed up to 3-times higher critical current (B||ab-plane) which correlated with a higher density of ab-plane stacking faults observed by TEM analysis.

In chapter 6, Artificial Neural Networks were trained to predict the critical currents at low temperatures (4.2 — 40 K) from the 65 K critical currents. The model was validated with a dataset of 100 samples showing an error of 2.8% at 4.2 K and 13 T. The statistical model was then combined with a physics-based fitting, $J_c \sim H^{-\alpha}$, to predict J_c at 4.2 K and high magnetic fields up 31 T.

7.1. Future Studies

- Molecular Dynamics simulations can be a valuable method to further understand the interactions between the flux vortices and the self-assembled nanorods.
- Molecular Dynamics simulations may also be valuable to understand the reason behind the formation of the bottle shaped nanorods and if this particular shape of nanorods has an effect on flux pinning in Zr-doped REBCO.

- For the present study, tensile-creep deformation was applied on samples with a maximum length of 20 cm. Scaling up the process to long tapes may be challenging but will be valuable for commercial applications.
- By increasing the dataset size, it may be possible using machine learning methods to predict in-magnetic field critical currents using self-field critical current at 77 K and film composition. Using the current dataset size (450 sample) the artificial neural network predictions were not able to achieve this prediction with an acceptable accuracy.

References

[1] H. K. Onnes, "Further experiments with liquid helium." pp. 1910-1911.

[2] J. Bardeen, “LN cooper, and JR Schrieffer,” *Phys. Rev,* vol. 108, no. 1175, pp. 5, 1957.

[3] J. Nagamatsu, N. Nakagawa, T. Muranaka, Y. Zenitani, and J. Akimitsu, “Superconductivity at 39 K in magnesium diboride,” *Nature materials,* vol. 410, no. 6824, pp. 63, 2001.

[4] M. Wu, J. Ashburn, C. Torng, P. Hor, R. Meng, L. Gao, Z. Huang, Y. Wang, and C. Chu, “Superconductivity at 93 K in a New Mixed-Phase Y-Ba-Cu-O Compound System at Ambient Pressure,” *Physical Review Letters,* pp. O80, 1987.

[5] H. Maeda, Y. Tanaka, M. Fukutomi, and T. Asano, “A new high-Tc oxide superconductor without a rare earth element,” *Japanese Journal of Applied Physics,* vol. 27, no. 2A, pp. L209, 1988.

[6] L. Gao, Y. Xue, F. Chen, Q. Xiong, R. Meng, D. Ramirez, C. Chu, J. Eggert, and H. Mao, “Superconductivity up to 164 K in $HgBa_2Ca_{m-1}Cu_mO_{2m+2+\delta}$ (m= 1, 2, and 3) under quasihydrostatic pressures,” *Physical Review B,* vol. 50, no. 6, pp. 4260, 1994.

[7] Z. Melhem, *High temperature superconductors (HTS) for energy applications*: Elsevier, 2011.

[8] E. Siegrist, S. Sunshine, D. Murphy, R. J. Cava, and S. Zahurak, “Crystal structure of the high-T_c superconductor $Ba_2YCu_3O_{9-\delta}$,” *Physical Review B,* vol. 35, no. 13, pp. 7137, 1987.

[9] J. Jorgensen, B. Veal, A. P. Paulikas, L. Nowicki, G. Crabtree, H. Claus, and W. Kwok, "Structural properties of oxygen-deficient $YBa_2Cu_3O_{7-\delta}$," *Physical Review B,* vol. 41, no. 4, pp. 1863, 1990.

[10] P. Benzi, E. Bottizzo, and N. Rizzi, "Oxygen determination from cell dimensions in YBCO superconductors," *Journal of Crystal Growth,* vol. 269, no. 2-4, pp. 625-629, 2004.

[11] A. Xu, "Flux Pinning Study of $REBa_2Cu_3O_{7-\delta}$ Coated Conductors for High Field Magnet Applications," Thesis, 2012.

[12] V. Breit, P. Schweiss, R. Hauff, H. Wühl, H. Claus, H. Rietschel, A. Erb, and G. Müller-Vogt, "Evidence for chain superconductivity in near-stoichiometric $YBa_2Cu_3O_x$ single crystals," *Physical Review B,* vol. 52, no. 22, pp. R15727, 1995.

[13] P. Bordet, C. Chaillout, J. Chenavas, J. Hodeau, M. Marezio, J. Karpinski, and E. Kaldis, "Structure determination of the new high-temperature superconductor $Y_2Ba_4Cu_7O_{14+x}$," *Nature materials,* vol. 334, no. 6183, pp. 596, 1988.

[14] P. Marsh, R. Fleming, M. Mandich, A. DeSantolo, J. Kwo, M. Hong, and L. Martinez-Miranda, "Crystal structure of the 80 K superconductor $YBa_2Cu_4O_8$," *Nature materials,* vol. 334, no. 6178, pp. 141, 1988.

[15] K. Oka, Z. Zou, and J. Ye, "Crystal growth of superconductive $PrBa_2Cu_3O_{7-y}$," *Physica C: Superconductivity,* vol. 300, no. 3-4, pp. 200-206, 1998.

[16] D. Quinn III, and W. Ittner III, "Resistance in a Superconductor," *Journal of Applied Physics,* vol. 33, no. 2, pp. 748-749, 1962.

[17] W. Meissner, and R. Ochsenfeld, “Ein neuer effekt bei eintritt der supraleitfähigkeit,” *Naturwissenschaften,* vol. 21, no. 44, pp. 787-788, 1933.

[18] T. Matsushita, *Flux pinning in superconductors*: Springer, 2007.

[19] D. A. Cardwell, and D. S. Ginley, *Handbook of superconducting materials*: CRC Press, 2003.

[20] M. Daeumling, J. Seuntjens, and D. Larbalestier, “Oxygen-defect flux pinning, anomalous magnetization and intra-grain granularity in $YBa_2Cu_3O_{7-\delta}$,” *Nature,* vol. 346, no. 6282, pp. 332, 1990.

[21] F. Klaassen, G. Doornbos, J. Huijbregtse, R. Van der Geest, B. Dam, and R. Griessen, “Vortex pinning by natural linear defects in thin films of $YBa_2Cu_3O_{7-\delta}$,” *Physical Review B,* vol. 64, no. 18, pp. 184523, 2001.

[22] J. MacManus-Driscoll, S. Foltyn, B. Maiorov, Q. Jia, H. Wang, A. Serquis, L. Civale, Y. Lin, M. Hawley, and M. Maley, “Rare earth ion size effects and enhanced critical current densities in $Y_{2/3}Sm_{1/3}Ba_2Cu_3O_{7-x}$ coated conductors,” *Applied Physics Letters,* vol. 86, no. 3, pp. 032505, 2005.

[23] J. Wang, J. Kwon, J. Yoon, H. Wang, T. Haugan, F. Baca, N. Pierce, and P. Barnes, “Flux pinning in $YBa_2Cu_3O_{7-\delta}$thin film samples linked to stacking fault density,” *Applied Physics Letters,* vol. 92, no. 8, pp. 082507, 2008.

[24] J. Huijbregtse, F. Klaassen, A. Szepielow, J. Rector, B. Dam, R. Griessen, B. Kooi, and J. T. M. De Hosson, “Vortex pinning by natural defects in thin films of $YBa_2Cu_3O_{7-\delta}$,” *Superconductor Science Technology,* vol. 15, no. 3, pp. 395, 2002.

[25] H. Tobita, K. Notoh, K. Higashikawa, M. Inoue, T. Kiss, T. Kato, T. Hirayama, M. Yoshizumi, T. Izumi, and Y. Shiohara, "Fabrication of $BaHfO_3$ doped $Gd_1Ba_2Cu_3O_{7-\delta}$ coated conductors with the high Ic of 85 A/cm-w under 3 T at liquid nitrogen temperature (77 K)," *Superconductor Science Technology,* vol. 25, no. 6, pp. 062002, 2012.

[26] P. Mele, K. Matsumoto, T. Horide, A. Ichinose, M. Mukaida, Y. Yoshida, S. Horii, and R. Kita, "Ultra-high flux pinning properties of $BaMO_3$-doped $YBa_2Cu_3O_{7-x}$ thin films (M= Zr, Sn)," *Superconductor Science Technology,* vol. 21, no. 3, pp. 032002, 2008.

[27] C. Varanasi, J. Burke, H. Wang, J. Lee, and P. Barnes, "Thick $YBa_2Cu_3O_{7-x}$+ $BaSnO_3$ films with enhanced critical current density at high magnetic fields," *Applied Physics Letters,* vol. 93, no. 9, pp. 092501, 2008.

[28] L. Civale, "Vortex pinning and creep in high-temperature superconductors with columnar defects," *Superconductor Science Technology,* vol. 10, no. 7A, pp. A11, 1997.

[29] K. Matsumoto, and P. Mele, "Artificial pinning center technology to enhance vortex pinning in YBCO coated conductors," *Superconductor Science Technology,* vol. 23, no. 1, pp. 014001, 2009.

[30] V. Maroni, Y. Li, D. Feldmann, and Q. Jia, "Correlation between cation disorder and flux pinning in the Y Ba 2 Cu 3 O 7 coated conductor," *Journal of Applied Physics,* vol. 102, no. 11, pp. 113909, 2007.

[31] T. Haugan, T. Campbell, N. Pierce, M. Locke, I. Maartense, and P. Barnes, "Microstructural and superconducting properties of (Y1− xEux) Ba2Cu3O7− δ

thin films: x= 0–1," *Superconductor Science Technology,* vol. 21, no. 2, pp. 025014, 2008.

[32] T. Haugan, P. Barnes, R. Wheeler, F. Meisenkothen, and M. Sumption, "Addition of nanoparticle dispersions to enhance flux pinning of the $YBa_2Cu_3O_{7-x}$ superconductor," *Nature,* vol. 430, no. 7002, pp. 867, 2004.

[33] R. Emergo, J. Wu, T. Aytug, and D. Christen, "Thickness dependence of superconducting critical current densityin vicinal $YBa_2Cu_3O_{7-\delta}$ thick films," *Applied physics letters*, vol. 85, no. 4, pp. 618-620, 2004.

[34] S. Foltyn, L. Civale, J. MacManus-Driscoll, Q. Jia, B. Maiorov, H. Wang, and M. Maley, "Materials science challenges for high-temperature superconducting wire," *Nature materials,* vol. 6, no. 9, pp. 631, 2007.

[35] T. G. Holesinger, L. Civale, B. Maiorov, D. M. Feldmann, J. Y. Coulter, D. J. Miller, V. A. Maroni, Z. Chen, D. C. Larbalestier, and R. Feenstra, "Progress in Nanoengineered Microstructures for Tunable High-Current, High-Temperature Superconducting Wires," *Advanced Materials,* vol. 20, no. 3, pp. 391-407, 2008.

[36] X. Song, Z. Chen, S.-I. Kim, D. M. Feldmann, D. Larbalestier, J. Reeves, Y. Xie, and V. Selvamanickam, "Evidence for strong flux pinning by small, dense nanoprecipitates in a Sm-doped $YBa_2Cu_3O_{7-\delta}$ coated conductor," *Applied physics letters,* vol. 88, no. 21, pp. 212508, 2006.

[37] J. Gutierrez, A. Llordes, J. Gazquez, M. Gibert, N. Roma, S. Ricart, A. Pomar, F. Sandiumenge, N. Mestres, and T. Puig, "Strong isotropic flux pinning in solution-derived $YBa_2Cu_3O_{7-x}$ nanocomposite superconductor films," *Nature materials,* vol. 6, no. 5, pp. 367, 2007.

[38] B. Maiorov, S. Baily, H. Zhou, O. Ugurlu, J. Kennison, P. Dowden, T. Holesinger, S. Foltyn, and L. Civale, "Synergetic combination of different types of defect to optimize pinning landscape using $BaZrO_3$-doped $YBa_2Cu_3O_7$," *Nature materials,* vol. 8, no. 5, pp. 398, 2009.

[39] L. Civale, A. Marwick, T. Worthington, M. Kirk, J. Thompson, L. Krusin-Elbaum, Y. Sun, J. Clem, and F. Holtzberg, "Vortex confinement by columnar defects in $YBa_2Cu_3O_7$ crystals: Enhanced pinning at high fields and temperatures," *Physical Review Letters,* vol. 67, no. 5, pp. 648, 1991.

[40] Y. Chen, V. Selvamanickam, Y. Zhang, Y. Zuev, C. Cantoni, E. Specht, M. P. Paranthaman, T. Aytug, A. Goyal, and D. Lee, "Enhanced flux pinning by $BaZrO_3$ and $(Gd, Y)_2O_3$ nanostructures in metal organic chemical vapor deposited GdYBCO high temperature superconductor tapes," *Applied Physics Letters,* vol. 94, no. 6, pp. 062513, 2009.

[41] J. MacManus-Driscoll, S. Foltyn, Q. Jia, H. Wang, A. Serquis, L. Civale, B. Maiorov, M. Hawley, M. Maley, and D. Peterson, "Strongly enhanced current densities in superconducting coated conductors of $YBa_2Cu_3O_{7-x}$+ $BaZrO_3$," *Nature materials,* vol. 3, no. 7, pp. 439, 2004.

[42] V. Selvamanickam, M. Mironova, S. Son, and K. Salama, "Flux pinning by dislocations in deformed melt-textured $YBa_2Cu_3O_x$ superconductors," *Physica C: Superconductivity,* vol. 208, no. 3-4, pp. 238-244, 1993.

[43] B. Dam, J. Huijbregtse, F. Klaassen, R. Van der Geest, G. Doornbos, J. Rector, A. Testa, S. Freisem, J. Martinez, and B. Stäuble-Pümpin, "Origin of high

critical currents in $YBa_2Cu_3O_{7-\delta}$ superconducting thin films," *Nature,* vol. 399, no. 6735, pp. 439, 1999.

[44] D. Larbalestier, A. Gurevich, D. M. Feldmann, and A. Polyanskii, "High-Tc superconducting materials for electric power applications," *Materials For Sustainable Energy: A Collection of Peer-Reviewed Research and Review Articles from Nature Publishing Group,* pp. 311-320: World Scientific, 2011.

[45] D. Dimos, P. Chaudhari, and J. Mannhart, "Superconducting transport properties of grain boundaries in $YBa_2Cu_3O_7$ bicrystals," *Physical Review B,* vol. 41, no. 7, pp. 4038, 1990.

[46] X. Song, G. Daniels, D. M. Feldmann, A. Gurevich, and D. Larbalestier, "Electromagnetic, atomic structure and chemistry changes induced by Ca-doping of low-angle $YBa_2Cu_3O_{7-\delta}$ grain boundaries," *Nature Materials,* vol. 4, no. 6, pp. 470, 2005.

[47] D. W. Hazelton, "2G HTS wire development at superPower," 2016.

[48] T. Nagaishi, Y. Shingai, M. Konishi, T. Taneda, H. Ota, G. Honda, T. Kato, and K. Ohmatsu, "Development of REBCO coated conductors on textured metallic substrates," *Physica C: Superconductivity,* vol. 469, no. 15-20, pp. 1311-1315, 2009.

[49] R. Pratap, "Growth and Optimization of High-Performance Thick Rebco Films for Application over a Wide Range of Temperature (77-4.2) K and Magnetic Fields (0–15) T," 2019.

[50] C. Barth, G. Mondonico, and C. Senatore, "Electro-mechanical properties of REBCO coated conductors from various industrial manufacturers at 77 K, self-

field and 4.2 K, 19 T," *Superconductor Science Technology,* vol. 28, no. 4, pp. 045011, 2015.

[51] L. Civale, B. Maiorov, A. Serquis, J. Willis, J. Coulter, H. Wang, Q. Jia, P. Arendt, J. a. MacManus-Driscoll, and M. Maley, "Angular-dependent vortex pinning mechanisms in $YBa_2Cu_3O_7$ coated conductors and thin films," *Applied Physics Letters,* vol. 84, no. 12, pp. 2121-2123, 2004.

[52] A. Xu, V. Braccini, J. Jaroszynski, Y. Xin, and D. Larbalestier, "Role of weak uncorrelated pinning introduced by $BaZrO_3$ nanorods at low-temperature in (Y, Gd) $Ba_2Cu_3O_x$ thin films," *Physical Review B,* vol. 86, no. 11, pp. 115416, 2012.

[53] T. Puig, J. Gutiérrez, A. Pomar, A. Llordés, J. Gazquez, S. Ricart, F. Sandiumenge, and X. Obradors, "Vortex pinning in chemical solution nanostructured YBCO films," *Superconductor Science Technology,* vol. 21, no. 3, pp. 034008, 2008.

[54] Y. Tsuchiya, S. Miura, S. Awaji, Y. Ichino, K. Matsumoto, T. Izumi, K. Watanabe, and Y. Yoshida, "Flux pinning landscape up to 25 T in $SmBa_2Cu_3O_y$ films with $BaHfO_3$ nanorods fabricated by low-temperature growth technique," *Superconductor Science Technology,* vol. 30, no. 10, pp. 104004, 2017.

[55] J. Plain, T. Puig, F. Sandiumenge, X. Obradors, and J. Rabier, "Microstructural influence on critical currents and irreversibility line in melt-textured YBa 2 Cu 3 O 7− x reannealed at high oxygen pressure," *Physical Review B,* vol. 65, no. 10, pp. 104526, 2002.

[56] J. Gutierrez, T. Puig, and X. Obradors, “Anisotropy and strength of vortex pinning centers in Y Ba 2 Cu 3 O 7− x coated conductors,” *Applied physics letters,* vol. 90, no. 16, pp. 162514, 2007.

[57] D. R. Nelson, and V. Vinokur, “Boson localization and correlated pinning of superconducting vortex arrays,” *Physical Review B,* vol. 48, no. 17, pp. 13060, 1993.

[58] V. Moshchalkov, V. Metlushko, G. Güntherodt, I. Goncharov, A. Y. Didyk, and Y. Bruynseraede, “Irradiation-induced crossover from point defects to correlated disorder pinning in $Bi_2Sr_2CaCu_2O_x$ single crystals,” *Physical Review B,* vol. 50, no. 1, pp. 639, 1994.

[59] Y. Iye, T. Tamegai, H. Takeya, and H. Takei, “Critical field anisotropy of a single crystal $GdBa_2Cu_3O_x$ and $HoBa_2Cu_3O_x$,” *Japanese journal of applied physics,* vol. 26, no. 11A, pp. L1850, 1987.

[60] K. Nakao, N. Miura, K. Tatsuhara, S.-i. Uchida, H. Takagi, T. Wada, and S. Tanaka, “Superconductivity in $YBa_2Cu_3O_{7-x}$ in a 100 tesla magnetic field,” *Nature,* vol. 332, no. 6167, pp. 816, 1988.

[61] A. Dzurak, B. Kane, R. Clark, N. Lumpkin, J. O’Brien, G. Facer, R. Starrett, A. Skougarevsky, H. Nakagawa, and N. Miura, “Transport measurements of in-plane critical fields in $YBa_2Cu_3O_{7-\delta}$ to 300 T,” *Physical Review B,* vol. 57, no. 22, pp. R14084, 1998.

[62] C. P. Bean, “Magnetization of high-field superconductors,” *Reviews of modern physics,* vol. 36, no. 1, pp. 31, 1964.

[63] C. P. Bean, “Magnetization of hard superconductors,” *Physical review letters*, vol. 8, no. 6, pp. 250, 1962.

[64] P. W. Anderson, and Y. Kim, “Hard superconductivity: theory of the motion of Abrikosov flux lines,” *Reviews of modern physics*, vol. 36, no. 1, pp. 39, 1964.

[65] P. W. Anderson, “Theory of flux creep in hard superconductors,” *Physical Review Letters*, vol. 9, no. 7, pp. 309, 1962.

[66] E. J. Kramer, “Scaling laws for flux pinning in hard superconductors,” *Journal of Applied Physics*, vol. 44, no. 3, pp. 1360-1370, 1973.

[67] G. Blatter, M. V. Feigel'man, V. B. Geshkenbein, A. I. Larkin, and V. M. Vinokur, “Vortices in high-temperature superconductors,” *Reviews of Modern Physics*, vol. 66, no. 4, pp. 1125, 1994.

[68] H. Zhou, B. Maiorov, S. Baily, P. Dowden, J. Kennison, L. Stan, T. Holesinger, Q. Jia, S. Foltyn, and L. Civale, “Thickness dependence of critical current density in $YBa_2Cu_3O_{7-\delta}$ films with $BaZrO_3$ and Y_2O_3 addition,” *Superconductor Science Technology*, vol. 22, no. 8, pp. 085013, 2009.

[69] G. Majkic, "Progress in Thick Film 2G-HTS Development," *Superconductivity*, pp. 73-131: Springer, 2020.

[70] G. Majkic, R. Pratap, A. Xu, E. Galstyan, H. C. Higley, S. O. Prestemon, X. Wang, D. Abraimov, J. Jaroszynski, and V. Selvamanickam, “Engineering current density over 5 kA mm^{-2} at 4.2 K, 14 T in thick film REBCO tapes,” *Superconductor Science Technology*, vol. 31, no. 10, pp. 10LT01, 2018.

[71] G. Majkic, E. Galstyan, and V. Selvamanickam, “High performance 2G-HTS wire using a novel MOCVD system,” *IEEE Transactions on Applied Superconductivity,* vol. 25, no. 3, pp. 1-4, 2014.

[72] A. Umezawa, G. Crabtree, J. Liu, H. Weber, W. Kwok, L. Nunez, T. Moran, C. Sowers, and H. Claus, “Enhanced critical magnetization currents due to fast neutron irradiation in single-crystal $YBa_2Cu_3O_{7-\delta}$,” *Physical Review B,* vol. 36, no. 13, pp. 7151, 1987.

[73] Ö. Polat, J. Sinclair, Y. L. Zuev, J. R. Thompson, D. K. Christen, S. W. Cook, D. Kumar, Y. Chen, and V. Selvamanickam, “Thickness dependence of magnetic relaxation and E-J characteristics in superconducting (Gd-Y)-Ba-Cu-O films with strong vortex pinning,” *Physical review B,* vol. 84, no. 2, pp. 024519, 2011.

[74] G. Majkic, R. Pratap, A. Xu, E. Galstyan, and V. Selvamanickam, “Over 15 MA/cm^2 of critical current density in 4.8 μm thick, Zr-doped (Gd, Y)$Ba_2Cu_3O_x$ superconductor at 30 K, 3T,” *Scientific reports,* vol. 8, no. 1, pp. 6982, 2018.

[75] A. Gurevich, “Pinning size effects in critical currents of superconducting films,” *Superconductor Science Technology,* vol. 20, no. 9, pp. S128, 2007.

[76] S. Senoussi, M. Osséna, G. Collin, and I. Campbell, “Exponential H and T decay of the critical current density in Y Ba 2 Cu 3 O 7− δ single crystals,” *Physical Review B,* vol. 37, no. 16, pp. 9792, 1988.

[77] X. Wang, F. J. Baca, R. L. Emergo, J. Z. Wu, T. J. Haugan, and P. N. Barnes, “Eliminating thickness dependence of critical current density in $YBa_2Cu_3O_{7-x}$

films with aligned $BaZrO_3$ nanorods," *Journal of Applied Physics,* vol. 108, no. 11, pp. 113911, 2010.

[78] M. H. Gharahcheshmeh, E. Galstyan, A. Xu, J. Kukunuru, R. Katta, Y. Zhang, G. Majkic, X. Li, and V. Selvamanickam, "Superconducting transition width (ΔT_c) characteristics of 25 mol% Zr-added (Gd, Y) $Ba_2Cu_3O_{7-\delta}$ superconductor tapes with high in-field critical current density at 30 K," *Superconductor Science Technology,* vol. 30, no. 1, pp. 015016, 2016.

[79] H. Huhtinen, K. Schlesier, and P. Paturi, "Growth and c-axis flux pinning of nanostructured YBCO/BZO multilayers," *Superconductor Science Technology,* vol. 22, no. 7, pp. 075019, 2009.

[80] C. Cai, J. Hänisch, R. Hühne, V. Stehr, C. Mickel, T. Gemming, and B. Holzapfel, "Structural and magnetotransport properties of $YBa_2Cu_3O_{7-\delta}/Y_2O_3$ quasimultilayers," *Journal of applied physics,* vol. 98, no. 12, pp. 123906, 2005.

[81] T. Matsushita, H. Nagamizu, K. Tanabe, M. Kiuchi, E. Otabe, H. Tobita, M. Yoshizumi, T. Izumi, Y. Shiohara, and D. Yokoe, "Improvement of flux pinning performance at high magnetic fields in $GdBa_2Cu_3O_y$ coated conductors with BHO nano-rods through enhancement of Bc_2," *Superconductor Science Technology,* vol. 25, no. 12, pp. 125003, 2012.

[82] T. Matsushita, M. Kiuchi, T. Haraguchi, T. Imada, K. Okamura, S. Okayasu, S. Uchida, J.-i. Shimoyama, and K. Kishio, "Condensation energy density in Bi-2212 superconductors," *Superconductor Science Technology,* vol. 19, no. 2, pp. 200, 2006.

[83] M. Kochat, R. Pratap, E. Galstyan, G. Majkic, and V. Selvamanickam, "Electromagnetic Properties of Thick Film REBCO Tapes," *IEEE Transactions on Applied Superconductivity,* vol. 29, no. 5, pp. 1-4, 2019.

[84] E. Galstyan, R. Pratap, G. Majkic, M. Kochat, V. Mohan, and V. Selvamanickam, "Correlation Between Microstructure and In-Field Performance of Zr-Added REBCO Coated Conductors Made by Advanced MOCVD," *IEEE Transactions on Applied Superconductivity,* vol. 29, no. 5, pp. 1-6, 2019.

[85] A. Xu, N. Khatri, Y. Liu, G. Majkic, E. Galstyan, V. Selvamanickam, Y. Chen, C. Lei, D. Abraimov, and X. Hu, "Broad temperature pinning study of 15 mol.% Zr-Added (Gd, Y)–Ba–Cu–O MOCVD coated conductors," *IEEE Transactions on Applied Superconductivity,* vol. 25, no. 3, pp. 1-5, 2014.

[86] V. Braccini, A. Xu, J. Jaroszynski, Y. Xin, D. Larbalestier, Y. Chen, G. Carota, J. Dackow, I. Kesgin, and Y. Yao, "Properties of recent IBAD–MOCVD coated conductors relevant to their high field, low temperature magnet use," *Superconductor Science Technology,* vol. 24, no. 3, pp. 035001, 2010.

[87] A. Xu, L. Delgado, N. Khatri, Y. Liu, V. Selvamanickam, D. Abraimov, J. Jaroszynski, F. Kametani, and D. Larbalestier, "Strongly enhanced vortex pinning from 4 to 77 K in magnetic fields up to 31 T in 15 mol.% Zr-added (Gd,Y)-Ba-Cu-O superconducting tapes," *Apl Materials,* vol. 2, no. 4, pp. 046111, 2014.

[88] Y. Tsuchiya, S. Awaji, K. Watanabe, S. Miura, Y. Ichino, Y. Yoshida, and K. Matsumoto, "Delocalization of vortex in $SmBa_2Cu_3O_{7-\delta}$ superconducting films

with $BaHfO_3$ nano-rods," *Journal of Applied Physics,* vol. 120, no. 10, pp. 103902, 2016.

[89] T. Sekitani, N. Miura, S. Ikeda, Y. Matsuda, and Y. Shiohara, "Upper critical field for optimally-doped $YBa_2Cu_3O_{7-\delta}$," *Physica B: Condensed Matter,* vol. 346, pp. 319-324, 2004.

[90] S. Rosenzweig, J. Hänisch, K. Iida, A. Kauffmann, C. Mickel, T. Thersleff, J. Freudenberger, R. Hühne, B. Holzapfel, L. J. S. S. Schultz, and Technology, "Irreversibility field up to 42 T of $GdBa_2Cu3O_{7-\delta}$ thin films grown by PLD and its dependence on deposition parameters," *Superconductor Science Technology,* vol. 23, no. 10, pp. 105017, 2010.

[91] Z. Chen, F. Kametani, Y. Chen, Y. Xie, V. Selvamanickam, and D. Larbalestier, "A high critical current density MOCVD coated conductor with strong vortex pinning centers suitable for very high field use," *Superconductor Science Technology,* vol. 22, no. 5, pp. 055013, 2009.

[92] S. Fujita, S. Muto, W. Hirata, Y. Adachi, T. Yoshida, M. Igarashi, K. Kakimoto, Y. Iijima, K. Naoe, and T. Kiss, "Development of long-length BMO-doped REBCO coated conductors by hot-wall PLD process," *IEEE Transactions on Applied Superconductivity,* vol. 28, no. 4, pp. 1-4, 2018.

[93] M. Inoue, Y. Yamaguchi, T. Sakakibara, K. Imamura, K. Higashikawa, T. Kiss, S. Awaji, K. Watanabe, H. Tobita, and M. Yoshizumi, "Enhancement of In-Field Current Transport Properties in GdBCO Coated Conductors by $BaHfO_3$ Doping," *IEEE Transactions on Applied Superconductivity,* vol. 23, no. 3, pp. 8002304-8002304, 2013.

[94] F. Baca, P. Barnes, R. Emergo, T. Haugan, J. Reichart, and J. Wu, "Control of $BaZrO_3$ nanorod alignment in $YBa_2Cu_3O_{7-x}$ thin films by microstructural modulation," *Applied Physics Letters,* vol. 94, no. 10, pp. 102512, 2009.

[95] P. Mele, R. Guzman, J. Gazquez, T. Puig, X. Obradors, S. Saini, Y. Yoshida, M. Mukaida, A. Ichinose, and K. Matsumoto, "High pinning performance of $YBa_2Cu_3O_{7-x}$ films added with Y_2O_3 nanoparticulate defects," *Superconductor Science Technology,* vol. 28, no. 2, pp. 024002, 2014.

[96] H. Wang, A. Serquis, B. Maiorov, L. Civale, Q. Jia, P. Arendt, S. Foltyn, J. MacManus-Driscoll, and X. Zhang, "Microstructure and transport properties of Y-rich $YBa_2Cu_3O_{7-\delta}$ thin films," *Journal of applied physics,* vol. 100, no. 5, pp. 053904, 2006.

[97] Y. Li, J. Zhao, C. Chern, P. Lu, T. Chien, B. Gallois, P. Norris, B. Kear, and F. Cosandey, "Effects of Y_2O_3 precipitates on critical current anisotropy in $YBa_2Cu_3O_{7-x}$ thin films prepared by plasma-enhanced metalorganic vapor deposition," *Applied physics letters,* vol. 60, no. 19, pp. 2430-2432, 1992.

[98] E. D. Specht, A. Goyal, J. Li, P. M. Martin, X. Li, and M. Rupich, "Stacking faults in $YBa_2Cu_3O_{7-x}$: Measurement using x-ray diffraction and effects on critical current," *Applied physics letters,* vol. 89, no. 16, pp. 162510, 2006.

[99] S. H. Wee, E. D. Specht, C. Cantoni, Y. L. Zuev, V. Maroni, W. Wong-Ng, G. Liu, T. J. Haugan, and A. Goyal, "Formation of stacking faults and their correlation with flux pinning and critical current density in Sm-doped $YBa_2Cu_3O_{7-\delta}$ films," *Physical Review B,* vol. 83, no. 22, pp. 224520, 2011.

[100] S. Kar, W. Luo, A. B. Yahia, X. Li, G. Majkic, and V. Selvamanickam, "Symmetric tape round REBCO wire with J e (4.2 K, 15 T) beyond 450 A mm^{-2} at 15 mm bend radius: a viable candidate for future compact accelerator magnet applications," *Superconductor Science Technology*, vol. 31, no. 4, pp. 04LT01, 2018.

[101] S. Kar, J. S. Sandra, W. Luo, M. Kochat, J. Jaroszynski, D. Abraimov, G. Majkic, and V. Selvamanickam, "Next-generation highly flexible round REBCO STAR wires with over 580 A mm^{-2} at 4.2 K, 20 T for future compact magnets," *Superconductor Science Technology,* vol. 32, no. 10, pp. 10LT01, 2019.

[102] W. Luo, S. Kar, A. Xu, X. Li, A. B. Yahia, and V. Selvamanickam, "Fabrication and electromagnetic characterization of ultrasmall diameter REBCO wires," *IEEE Transactions on Applied Superconductivity,* vol. 27, no. 4, pp. 1-5, 2016.

[103] V. Selvamanickam, A. Xu, Y. Liu, N. Khatri, C. Lei, Y. Chen, E. Galstyan, and G. Majkic, "Correlation between in-field critical currents in Zr-added (Gd, Y) $Ba_2Cu_3O_x$ superconducting tapes at 30 and 77 K," *Superconductor Science Technology*, vol. 27, no. 5, pp. 055010, 2014.

[104] X.-F. Li, A. B. Yahia, G. Majkic, M. Kochat, S. Kar, and V. Selvamanickam, "Reel-to-reel critical current measurement of REBCO coated conductors," *IEEE Transactions on Applied Superconductivity*, vol. 27, no. 4, pp. 1-5, 2016.

[105] F. Pedregosa, G. Varoquaux, A. Gramfort, V. Michel, B. Thirion, O. Grisel, M. Blondel, P. Prettenhofer, R. Weiss, and V. Dubourg, "Scikit-learn: Machine

learning in Python," *Journal of machine learning research,* vol. 12, no. Oct, pp. 2825-2830, 2011.

[106] D. P. Kingma, and J. Ba, "Adam: A method for stochastic optimization," 2014.

[107] Investopedia. "R-Squared Definition," 10/22/2019, 2019; https://www.investopedia.com/terms/r/r-squared.asp.

[108] S. Kang, A. Goyal, J. Li, A. A. Gapud, P. M. Martin, L. Heatherly, J. R. Thompson, D. K. Christen, F. List, and M. Paranthaman, "High-performance high-Tc superconducting wires," *Science,* vol. 311, no. 5769, pp. 1911-1914, 2006.

[109] Y. Yamada, K. Takahashi, H. Kobayashi, M. Konishi, T. Watanabe, A. Ibi, T. Muroga, S. Miyata, T. Kato, and T. Hirayama, "Epitaxial nanostructure and defects effective for pinning in Y(RE)$Ba_2Cu_3O_{7-x}$ coated conductors," *Applied Physics Letters,* vol. 87, no. 13, pp. 132502, 2005.

[110] A. Llordes, A. Palau, J. Gázquez, M. Coll, R. Vlad, A. Pomar, J. Arbiol, R. Guzman, S. Ye, and V. Rouco, "Nanoscale strain-induced pair suppression as a vortex-pinning mechanism in high-temperature superconductors," *Nature materials,* vol. 11, no. 4, pp. 329, 2012.

[111] V. Selvamanickam, Y. Chen, J. Xie, Y. Zhang, A. Guevara, I. Kesgin, G. Majkic, and M. Martchevsky, "Influence of Zr and Ce doping on electromagnetic properties of (Gd, Y)–Ba–Cu–O superconducting tapes fabricated by metal organic chemical vapor deposition," *Physica C: Superconductivity,* vol. 469, no. 23-24, pp. 2037-2043, 2009.